AN OPTIMIZATION APPROACH TO THE DETERMINATION OF MANIPULATOR WORKSPACES

by

Lukas Johannes du Plessis

A thesis submitted in partial fulfillment of the requirements for the degree of

Master of Engineering

in the

Faculty of Engineering, University of Pretoria

January 1999

To my parents

ABSTRACT

AN OPTIMIZATION APPROACH TO THE DETERMINATION OF MANIPULATOR WORKSPACES

by **Lukas Johannes du Plessis**

Supervisor: **Professor J.A. Snyman**

Department of Mechanical Engineering

Degree: Master of Engineering

Keywords: accessible workspace, dextrous workspace, serial manipulator, parallel manipulator, Stewart platform, optimization, bifurcation, workspace characterization

The main objective of this study is to propose and develop a *general* numerical technique by means of which the workspaces of mechanical manipulators may be determined with relative *ease*. The emphasis is on parallel or so-called Stewart platforms.

Stewart platforms have many advantages over the traditional serial manipulators. These advantages include high accuracy, high stiffness, high load-to-weight ratio and most importantly, low cost. According to the literature, it is strongly felt that the use of parallel manipulators in many robotic tasks is so necessary that they will become indispensable in the near future.

In spite of the advantages of these mechanisms, the use of Stewart platforms is still mainly in an experimental stage. This is because there seems to be a lack of rational synthesis tools for the design of practically useful platform manipulators. In particular, the problems of the forward kinematics and workspace determination remain to be satisfactorily solved. This study addresses the latter problem. It is believed that if the workspace is understood, and its characterization properly done, then many design problems will easily be solved.

In this study a novel optimization approach to solving the workspace problem is introduced. An attempt is made to demonstrate that this approach is *general* in the sense that it is applicable to different kinds of manipulators, and may also easily be implemented to determine *various types* of accessible workspaces.

In particular, the generality of the method is illustrated by the fact that the optimization approach was successfully implemented for a redundantly controlled planar serial manipulator, a planar Stewart

platform as well as a spatial 6–3 Stewart platform. The optimization method is also successful in assisting in the characterization of the workspace by, for example, identifying interior curves connecting bifurcation points. This is of great potential importance with regard to the control of a manipulator within its workspace.

The description of the behavior of the planar manipulators, led to a new notation for labeling the workspaces. This notation arises in a natural way from the optimization approach, is generally applicable and easy to understand. Using this notation, the complete workspace may be described in terms of the behavior of the manipulator.

Of great practical importance is the treatment of dexterity requirements imposed on a Stewart platform. The optimization approach successfully determines different specified dextrous workspaces of the planar Stewart platform. An example of a dextrous workspace of the 6–3 Stewart platform was also successfully mapped. This is very significant, because as far as the author is aware, such a mapping has not previously been performed for the spatial case.

It is hoped that this study will lie the foundation for the development of a general and rational synthesis design tool for parallel manipulators. Further research that will be addressed in the near future, and stems from the work done here, is the determination of the feasible workspace for parallel manipulators subject to various additional prescribed mechanical constraints.

This study has important potential impact for the manufacturing industry of South Africa and other developing countries. The implementation of this technology lies in retrofitting existing non-CNC milling equipment to increase their capability at a lower cost than that of the alternative of purchasing traditional 5-axis machining centers.

SAMEVATTING

'n OPTIMERINGS-BENADERING TOT DIE BEPALING VAN MANIPULEERDER-WERKRUIMTES

deur: **Lukas Johannes du Plessis**

Studie-leier: **Professor J.A. Snyman**

Departement van Meganiese Ingenieurswese

Graad: Magister in Ingenieurwese

Sleutelwoorde: bereikbare werkruimte, bruikbare werkruimte, serie-manipuleerder, parallel-manipuleerder, Stewart platform, optimering, bifurkasie, werkruimte-karakterisering

Die doelwit van hierdie studie is om 'n *algemene* numeriese metode te ontwikkel, waarmee die werkruimtes van meganiese manipuleerders redelik *maklik* bepaal kan word. Die klem val op parallel- of sogenaamde Stewart platforms.

In vergelyking met die tradisionele serie-manipuleerders, beskik Stewart platforms oor bepaalde voordele. Hierdie voordele sluit onder andere in: hoë akkuraatheid, hoë styfheid, hoë las-tot-gewig verhouding en, die belangrikste voordeel, lae koste. Vanuit die literatuur is dit duidelik dat die potesiële gebruik van Stewart platforms so' belangrik is, dat hulle binne die afsienbare toekoms onvervangbaar sal wees.

Ten spyte van die voordele, is die gebruik van Stewart platforms hoofsaaklik nog in die eksperimentele fase. Dit wil voorkom asof daar 'n gebrek is aan rasionale sintese-metodes waarmee prakties-bruikbare parallel-manipuleerders ontwerp kan word. Onder andere is die afleiding van die voorwaarste kinematiese vergelykings, asook die bepaling van die werkruimtes van hierdie meganismes, huidiglik nog probleem-areas. Laasgenoemde probleem word in hierdie studie aangespreek. As die werkruimte deeglik omskryf, en dienooreenkomstig gekarakteriseer word, sal baie ontwerp-probleme betreklik maklik opgelos kan word.

'n Nuwe optimeringsmetode word voorgestel waarmee die werkruimtes van verskillende manipuleerders bepaal word. Hierdeur word aangetoon dat die metode *algemeen* toepasbaar is, en ook maklik implementeer kan word om *verskillende tipes* bereikbare werkruimtes mee te bepaal.

In besonder word die algemene toepasbaarheid van die metode aangetoon deur die suksesvolle bepaling van die werkruimtes van 'n oortollig-beheerde serie-manipuleerder, 'n vlak Stewart platform en 'n ruimtelike 6–3 Stewart platform. Met behulp van die optimerings-metode, kon die werkruimtes gekarakteriseer word deur, byvoorbeeld, die identifisering van interne krommes wat bifurkasie-punte verbind. Dit is van groot potensiële belang met betrekking tot die beheer van 'n manipuleerder binne die spesifieke werkruimte.

Die beskrywing van die gedrag van die vlak manipuleerders het gelei tot 'n nuwe metode om die werkruimtes te anoteer. Hierdie nuwe notasie, wat voortspruit uit die toepassing van die optimerings-metode, is algemeen bruikbaar en maklik verstaanbaar. Deur gebruik te maak van hierdie notasie, kan die algehele werkruimte beskryf word in terme van die fisiese gedrag van die manipuleerder.

Die afdwing van sekere bruikbaarheids-voorskrifte vir die Stewart platform is noodsaaklik vanuit 'n praktiese oogpunt. Verskillende bruikbare werkruimtes van die vlak Stewart platform is bepaal deur die optimeringsmetode te gebruik. Verder is daar 'n spesifieke voorbeeld van 'n bruikbare werkruimte van die 6–3 Stewart platform bereken. So ver die skrywer kon vasstel, is dit die eerste keer dat 'n bruikbare werkruimte vir hierdie ruimtelike manipuleerder bepaal is.

Daar word gehoop dat hierdie studie die grondslag sal lê vir die ontwikkeling van 'n algemene ontwerp-metodiek vir parallel-manipuleerders. As voortsetting van die werk wat hier gedoen is, word dit beoog om bereikbare werkruimtes van parallel-platforms, onderhewig aan verskeie ander voorgeskrewe meganiese begrensings, te bepaal.

Die vervaardigingssektor van die Suid-Afrikaanse nywerheid en van ander ontwikkelende lande, kan moontlik voordeel trek uit hierdie navorsing. Bestaande freesmasjiene, wat nie gerekenariseer is nie, kan opgradeer word deur die aanhegting van 'n Stewart platform. Sodoende kan die vermoëns van hierdie freesmasjiene uitgebrei word, en word die hoë kapitale uitgawe om 'n 5-as gerekenariseerde freesmasjien aan te koop, uitgeskakel.

ACKNOWLEDGEMENTS

I would like to express my deepest thanks to Prof. J.A. Snyman for his enthusiasm and guidance during this research. I feel privileged to have worked under such an excellent researcher and mentor.

I am very grateful for the six-month research period I spent in the USA. Without the effort of Prof. Snyman this excellent opportunity would not have been possible. Thank you also to Dr. J. Duffy and the rest of the CIMAR people who made the visit to the University of Florida the highlight of my education.

My sincere gratitude goes to the FRD and the University of Pretoria for their financial support. Finally, a special thank you goes to Mr. P.J. Saayman for the editing of the report, and everyone else who encouraged and assisted me during the completion of this study.

Praise the Lord!

TABLE OF CONTENTS

LIST OF FIGURES

Chapter 1

1 REVIEW OF STEWART PLATFORMS

1.1 INTRODUCTION

The main objective of this study is to propose and develop a *general* numerical technique by means of which the workspaces of mechanical manipulators may be determined with relative *ease*. The emphasis is on parallel or so-called Stewart platforms.

To give an understanding of the significance and importance of the development of analytical design tools for such mechanical manipulators, this introductory chapter presents a *brief survey* of the field of Stewart platforms. This review will also allow for the later assessment and evaluation of the merits of the method proposed here.

The review, in the form of a literature survey, starts with reference to the *history* and *uses* of Stewart platforms. This is followed by a discussion of the *different designs* and *commercial products* presently available. Because of their significance with respect to the current study, special attention is paid to the discussion of *existing methods* for the determination of manipulator workspaces. With reference to these existing methods the chapter is concluded with a *detailed motivation* for the current study.

1.2 HISTORY OF THE STEWART PLATFORM

In his 1965 article, Stewart [1] "describes a mechanism, which has six degrees of freedom (DOF) controlled in any combination by six motors each having a ground abutment". He proposed that the mechanism be used for a flight simulator for the training of helicopter pilots.

Although in-parallel devices or parallel-link manipulators are often called Stewart platforms, Stewart was not the original inventor of this type of mechanism. Stewart's proposed mechanism is only a different configuration of the six linear jack system developed by Gough [2] in 1947. Gough was one of the reviewers of Stewart's article and in his review he states that he designed a similar tire test machine (see Figure 1.1) in 1949, which was already built and operational in 1954-1955 [3].

Stewart's paper was published together with the communications of the reviewers, as well as the author's reply. Stewart acknowledged the fact that he was not aware of Gough's tire test machine and also states that, although it is similar to his flight simulation mechanism, it was designed using a different approach.

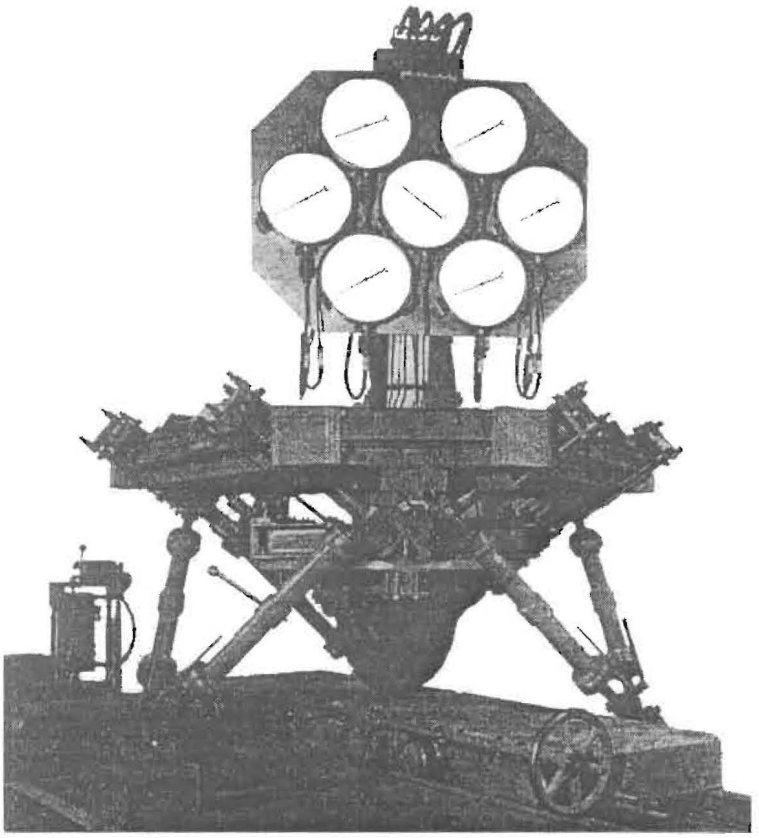

Figure 1.1 Gough's six DOF tire test machine (after [1]).

Ironically, Gough is also not acknowledged as the original inventor of this type of mechanism. According to Merlet [4] parallel manipulators have been known for a long time and the actual invention is attributed to the mathematician Cauchy, who wrote an article on the possible motion and rigidity of an "articulated octahedron" in 1813.

Merlet is of the opinion that although "Stewart platforms" is the name currently associated with these mechanisms, "Gough platforms" would be more appropriate.

Nevertheless, the re-discovery of the parallel manipulator by Stewart in 1965, sparked a flame that is still burning today. A schematic representation of the modern and general so-called 6–6 Stewart platform with prismatic actuators, is shown in Figure 1.2.

Merlet reports that real interest in this type of robot started around 1987, and from that date the number of papers on this subject increased drastically. Because of their inherent advantages of load carrying

capacity and spatial rigidity, Stewart platforms are suitable for a wide range of applications. It is believed that the research and development of parallel devices is currently the most popular topic in the area of robot manipulators [5].

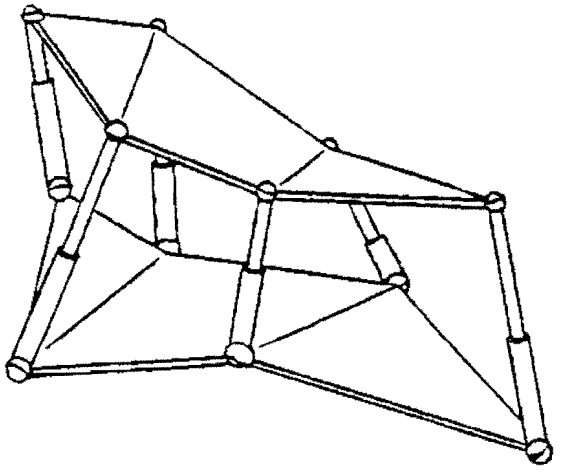

Figure 1.2 Schematic view of the general 6–6 Stewart platform (after [6]).

It is interesting to note that Stewart's proposal also raised some criticism. In his review on Stewart's article D. J. Thomas, referring to the possible use of the platform for flight simulation, asks: "Are six degrees of freedom really worthwhile?" In his reply Stewart points out that true flight can only achieved with six degrees of freedom [1].

1.3 USES OF STEWART PLATFORMS

Although Stewart proposed his mechanism for use as a flight simulator, he also suggested other possible uses for the mechanism, including:

- "a platform held stationary in space mounted on a vessel such as a ship subjected to the random movements of the sea."
- "a new form of machine tool."
- "an automatic assembly or transfer machine."

Some of the reviewers of Stewart's article also suggested possible uses of platform devices. G. H. Meier [1] stated that the machine tool and medical fields were suitable areas where these platforms may be used. Meier noticed that the inherent stability of the platform, as well as its light working platform,

made it attractive to the machine tool industry as a working table mounted to the platform. With a rotating table mounted to the platform, 360° rotation would be possible.

The second application suggested by Meier, is a stabilizing platform, where a Stewart platform could be used to eliminate rotational motions, and damp linear motions. Looking at a hospital ship for instance, this would mean that a doctor would be able to perform delicate operations as he would be working on a stabilized platform. Meier also mentioned a gun platform aboard a warship as another application.

Another reviewer, J. Tindale, stated that any improvements may be satisfactory from a machine point of view, but to prove their economical viability would require a period of expensive study and development. Tindale included in his review an artistic impression of a possible design of a universal mill, which could machine complicated shapes with simple cutters, as well as an artistic impression of an oil drilling rig, where the platform is supported on a tripod comprising six telescopic legs.

By the time Gough reviewed Stewart's article, his tire test machine was fitted with digitally controlled motor drives attached to the screw jacks, and electronic instrumentation to study tire-to-ground forces and movement.

The development of platforms for flight simulation and amusement park rides, has been ongoing since Stewart's article was published three decades ago. In his comprehensive review [4], Merlet explains that the reason for the main interest in these platforms, is their high nominal load-to-weight ratio. He developed a prototype platform which has a weight of 35kg, and can carry a load of 600kg. The weight of the load is approximately equally distributed on all the links. Another advantage is that the stress in each link is mostly of a traction-compression nature, which is very suitable for linear actuators and therefore contributes to the rigidity of the platforms.

There are other advantages that make Stewart platforms suitable for a wider range of applications. For example, Merlet states that because the position of the moving platform is less sensitive to the errors on the articulated sensors in comparison to serial link robots, Stewart platforms are ideally suited for assembly lineups. As early as 1979 a parallel manipulator was first used in a robotics assembly cell. Merlet also points out that parallel manipulators can be used as six component force sensors. Measuring the traction-compression stress in the links enables one to calculate the resulting force and torque acting on the mobile platform. This capability of parallel manipulators makes it possible for manipulators to be used as assembly units, where the platform comes in contact with its surroundings. Another application where this feature is important, is surface following.

Parallel manipulators can be very small where, for example, the linear actuators range a few micrometers enabling the upper platform to perform motions of a few nanometers. In contrast to this, Merlet also reports on a huge manipulator developed for mining operations.
One of the prototype platforms developed by Merlet is used for opthalmic surgery and the European Synchrotron Radiation Facility (ESRF) uses a more classical Gough type platform for the manipulation of heavy experimental setups.

Parallel manipulators can also be used in trusses. The mechanism modules are joined to form an articulated truss, which is light and highly redundant. Merlet states that these manipulators may be useful in space applications, once the kinematics and control problems have been solved.

In their article on five DOF parallel mechanisms, Wang and Gosselin [7] explain that the development of these manipulators is of interest, as they can be used for various tasks where mostly serial five DOF mechanisms are presently used. They mention tasks for which axi-symmetric tools are being used (e.g., drilling, welding, riveting, etc.), as well as the positioning and orientation of lasers, mirrors, antennas and spotlights.

1.4 DIFFERENT DESIGNS

Merlet [4] defines a parallel manipulator as a "closed-loop mechanism in which the end-effector is connected to the base by at least two independent kinematic chains." He also defines a fully-parallel manipulator as "a closed loop-manipulator with an n degrees-of-freedom (DOF) end-effector connected to the base by n independent chains, which have at most two links and are actuated by a unique prismatic or rotary actuator"

According to Merlet, many different designs of parallel manipulators are possible and the scientific literature is very rich on this topic. All have in common their low cost, since most of the components are standard, although the assembly of the manipulator must be done with care.

According to Merlet's definition, parallel manipulators include all in-parallel devices where the links have rotary or prismatic actuators. Stewart platforms traditionally are parallel manipulators equipped with prismatic actuators.

There are two main categories of parallel manipulators, namely planar and spatial manipulators.

Looking at the first category, a planar parallel manipulator is a special type of closed loop manipulator. Haug et al. [8] investigated the dextrous workspace of an elementary closed loop manipulator with one DOF. Gosselin and Wang [9] considered the singularity loci of a two DOF planar closed loop manipulator consisting of a five bar chain. Bajpai and Roth [10] determined the workspace of the same five bar chain, with a third additional DOF, as the basis of a manipulator mounted on a rotary joint.

The closed loop manipulators mentioned thus far have revolute actuators, and according to Merlet's definition, these mechanisms are not parallel manipulators as they are connected to the ground via two linearly *dependent* kinematic chains.

Gosselin and Wang [9] also consider a planar three DOF parallel manipulator with three revolute actuators. Seeing that this closed loop manipulator has two independent kinematic chains connecting the moving platform with the base, it can be classified as a parallel manipulator (see Figure 1.3).

The line segment moving platform in Figure 1.3 can be replaced by a triangular shaped moving platform. Kumar [11] characterizes the workspace of such a planar three DOF parallel manipulator (see Figure 1.4)

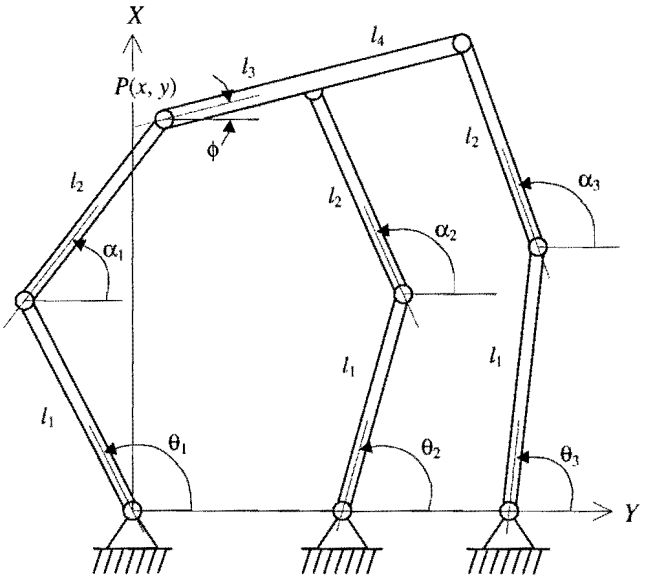

Figure 1.3 Planar three DOF parallel manipulator with revolute actuators (after [9]).

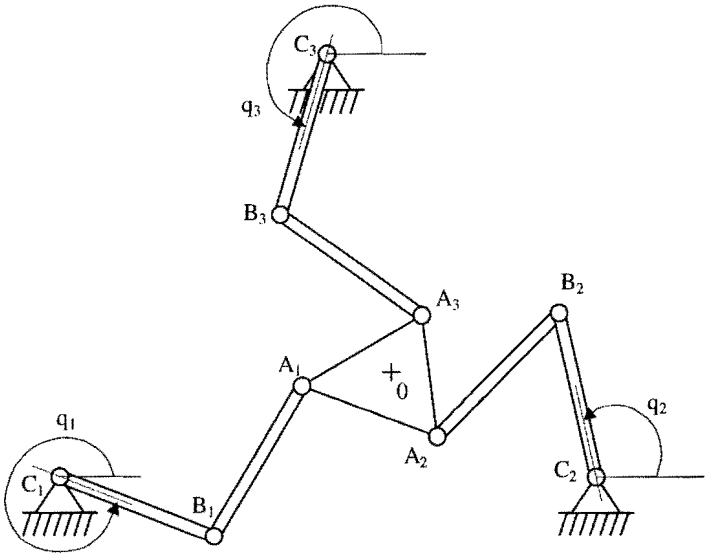

Figure 1.4 Three DOF parallel manipulator with a triangular moving platform and revolute actuators (after [11]).

The literature is also very rich as far as different designs of planar Stewart platforms (planar parallel manipulators with linear actuators) are concerned. Haug et al. [12] determine the workspace of a planar three DOF Stewart platform. This Stewart platform is a line segment platform with two coincident joints (see Figure 1.5).

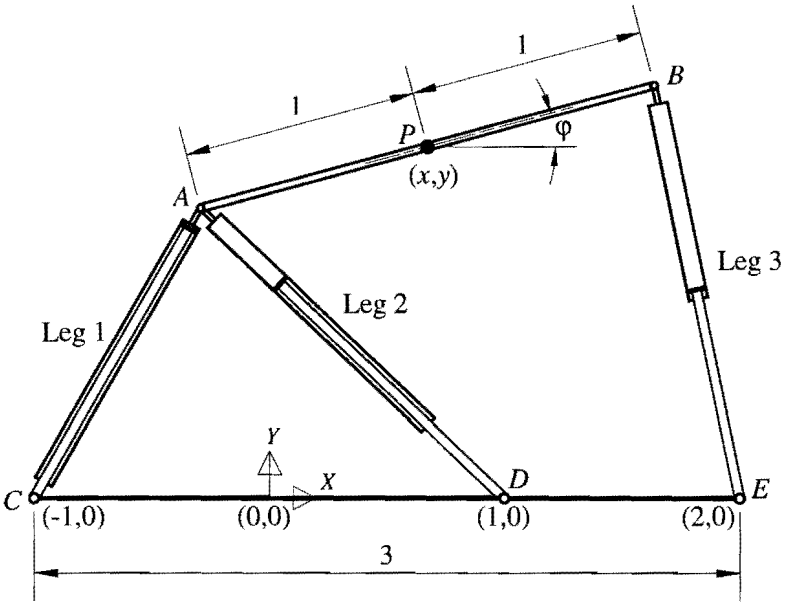

Figure 1.5 Three DOF planar Stewart platform (after [12]).

Some researchers also consider planar three DOF Stewart platforms with triangular moving platforms. Lee et al. [13] found that the optimum design, as far as stability is concerned, of a planar Stewart platform, is an equilateral moving platform (see Figure 1.6).

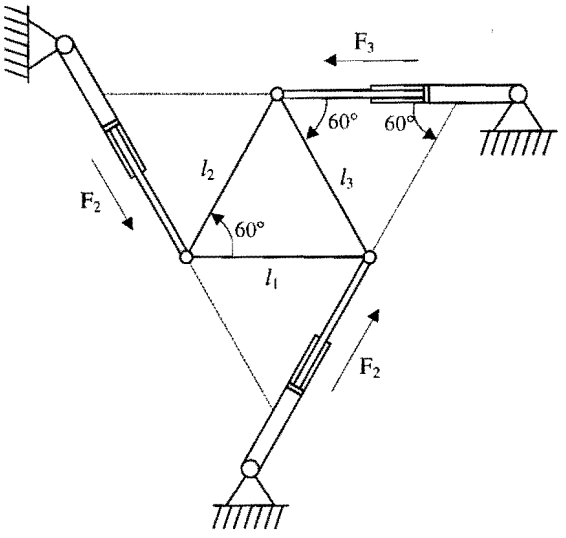

Figure 1.6 Planar three DOF Stewart platform with equilateral moving platform (after [13]).

In a later study Merlet et al. [14] determine the different workspaces of a planar Stewart platform with a triangular moving platform. They describe the mechanism in terms of the number and type of kinematic chains, with which the moving platform is connected to the ground. Both planar Stewart platforms shown in Figure 1.6 and Figure 1.7 are 3-RPR (Revolute-Prismatic-Revolute) parallel manipulators. In each manipulator, the mobile platform is connected to the base via three identical chains consisting of a revolute joint attached to the ground followed by an actuated prismatic joint which is connected to the platform by a revolute joint

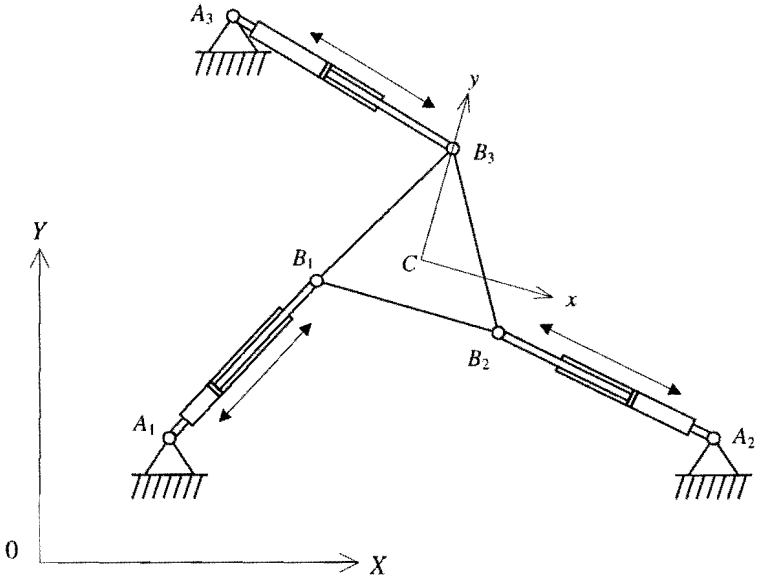

Figure 1.7 The three RPR parallel manipulator (after [14]).

The second category of parallel manipulators is spatial mechanisms. Depending on the design, these mechanisms can have three to six DOF. For instance, Wang and Gosselin [7] explain that three DOF and four DOF devices are sometimes used in flight simulation. Five DOF mechanisms are also available and used for tasks where axi-symmetrical tools are being used.

As pointed out by Stewart in his original paper, there are many possible designs for providing six DOF. One of the obvious designs is a three axis gimbal superimposed on a three axis linear slide system. Stewart [1] rejected this option, because he wanted to achieve the most simple and cohesive design with the highest capabilities in a wide range of applications.

The original mechanism proposed by Stewart [1] comprises out of a triangular plane, called the platform, of which each of the three corners is connected through a three-axis joint (spherical joint or ball-and-socket joint) to one off the three legs. Each leg is connected to the ground by a two-axis joint (universal joint). Three additional actuators are connected to the three legs. Each additional actuator has one end connected via a rotary joint to the outer-cylinder end of each leg. The other end of each additional actuator is connected to the foundation or base via a universal joint. (see Figure 1.8).

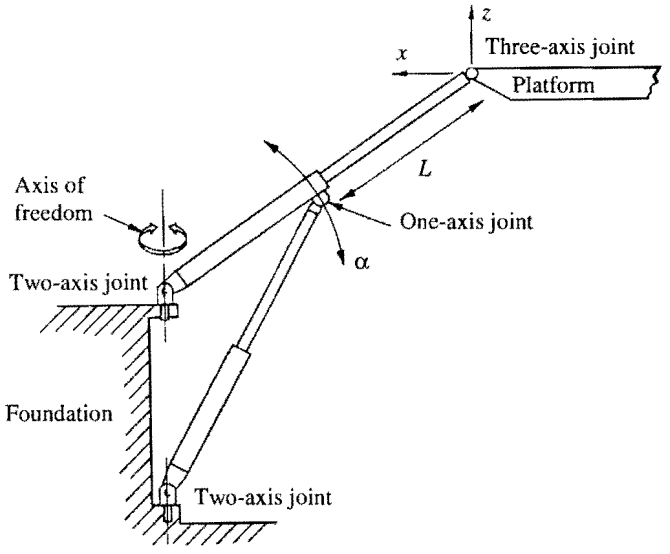

Figure 1.8 Stewart's original platform: General arrangement of single leg system (after [1]).

The two jack foundation connections have one common axis and the remaining axes are parallel to each other. The common axis is not controlled within the single leg system but the plane containing the leg can rotate about it, thereby permitting a three-axis motion on the platform support joint.

The tire test machine of Gough [3], also uses six actuators, but they are arranged differently. Each actuator is attached separately to the upper platform (see Figure 1.1). Gough uses the same universal

joint system to attach the actuators to the platform and the base, as described in his communications on Stewart's original paper [1].

Also included in the communications on Stewart's article, are comments by Murdoch and Meier who mention the preferred arrangement that would result from the use of the "linear coordinate leg system". This is a similar arrangement to the one Gough used for his tire test machine, where the actuator-foundation, and actuator-platform connecting points are co-planar.

A general parallel manipulator has the actuator connection points in any position on the fixed and moving bodies, i.e. the actuator connection points are not restricted to be co-planar [4] (see Figure 1.2).

Spatial parallel manipulators are usually labeled according to the number of connecting points on the base and moving platforms, keeping in mind that the name "Stewart platform" refers to a parallel manipulator equipped with linear prismatic actuators. Stewart's original platform can accordingly be labeled as a *special* 6-3 "Stewart platform", as there are six foundation connecting points and three moving platform connecting points. The word *special* is necessary when referring to this platform, as the three additional actuators are connected to the three actuator legs, instead of the moving platform.

Meier and Murdoch's [1] proposed configuration is a 6–3 Stewart platform, i.e. it has six actuator legs, the bottom ends of which are connected to the six base vertices, and the top ends of the actuators are connected in pairs to the three moving platform vertices.

Gough's tire test machine is accordingly labeled as a 3–6 Stewart platform, where the moving platform with six vertices is connected to the three base vertices. Furthermore, it follows that a 6–6 Stewart platform (see Figure 1.2) is where each of the six linear prismatic actuators connects a moving platform vertex with a base vertex.

The configuration of a spatial Stewart platform is not the only important design aspect. Equally important is the type of connections with which the actuators are connected to the moving platforms and base. Spatial parallel manipulators can also be described according to the kinematic chains that connect the fixed and moving bodies. For example: a 6–6 Stewart platform with the six linear actuator legs connected to the base and moving platforms via ball-and-socket (spherical) joints can also be labeled as a 6–6 Stewart platform with six identical SPS (Spherical-Prismatic-Spherical) chains.

According to Griffis and Duffy [15], it should be noted that in an SPS serial chain, the prismatic joint (P) has an extra DOF, a rotation about the line joining the centers of its S pairs. This extra DOF in each leg

does not affect the gross motion of the top platform. Either one of the S pairs could be replaced by a Hooke joint. However, this may not be desirable from a design standpoint.

As described earlier, Stewart uses 1-axis rotary, 2-axes universal and three axes spherical joints in his original platform. With a 6–3 or 3–6 configuration, the actuators are connected to the base with either a spherical or a universal joint, allowing rotation about respectively three or two axes. "Special" ball-and-socket joints are to be used to connect the top ends of the actuators in pairs to the moving platform.

Due to the design problems that arise from using pairs of concentric spherical joints, Lin et al. [16] emphasize that it is very important to eliminate, as far as possible, the use of concentric spherical joints.

Fichter [17] proposes that the ends of the legs be mounted on gimbals (Hooke joints), because if it is designed properly, a gimbal gives a much greater range of motion than a ball-and-socket joint. The platform gimbal is doubled to make the two adjacent legs coincident. The platform gimbal also has a third axis perpendicular to the platform plane, which makes it equivalent to a double ball joint. The base gimbal Fichter uses, has its first revolute axis inclined to the base plate to increase the useful range of motion of the joint (see Figure 1.9).

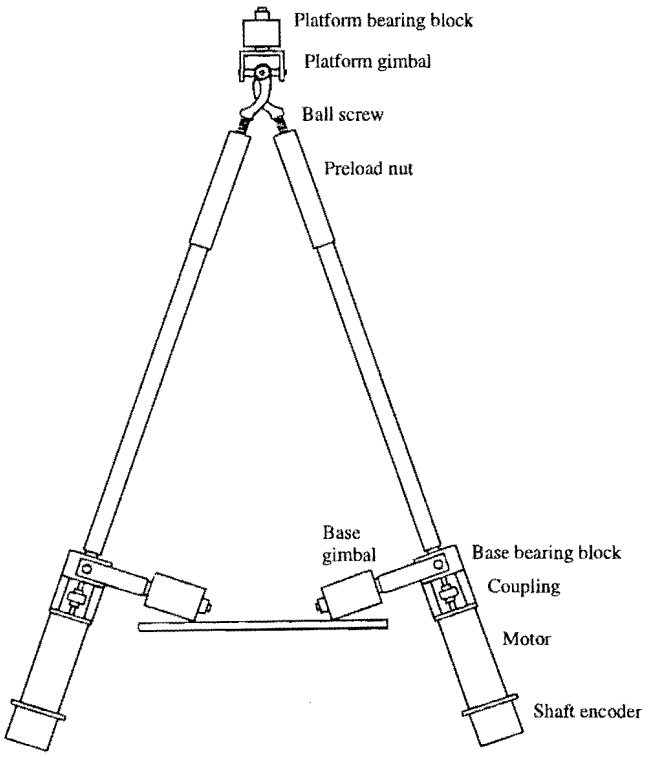

Figure 1.9 The leg triangle of the Stewart Platform built at Oregon State University (after [17]).

Liu et al. [18] have done the kinematic analyses of a 6–3 Stewart platform of the form shown in Figure 1.10. This Stewart platform has been built (see Figure 1.11) and is operational in the Arlington *Automation & Robotics Research Institute (ARRI)* of the University of Texas. As can be seen it uses the gimbal arrangement proposed by Fichter [17] as actuator connections (see Figure 1.12).

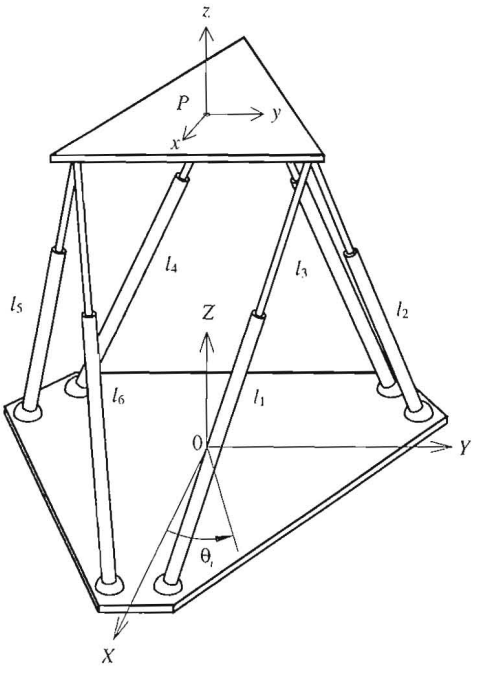

Figure 1.10 The 6-3 Stewart platform (after [18]).

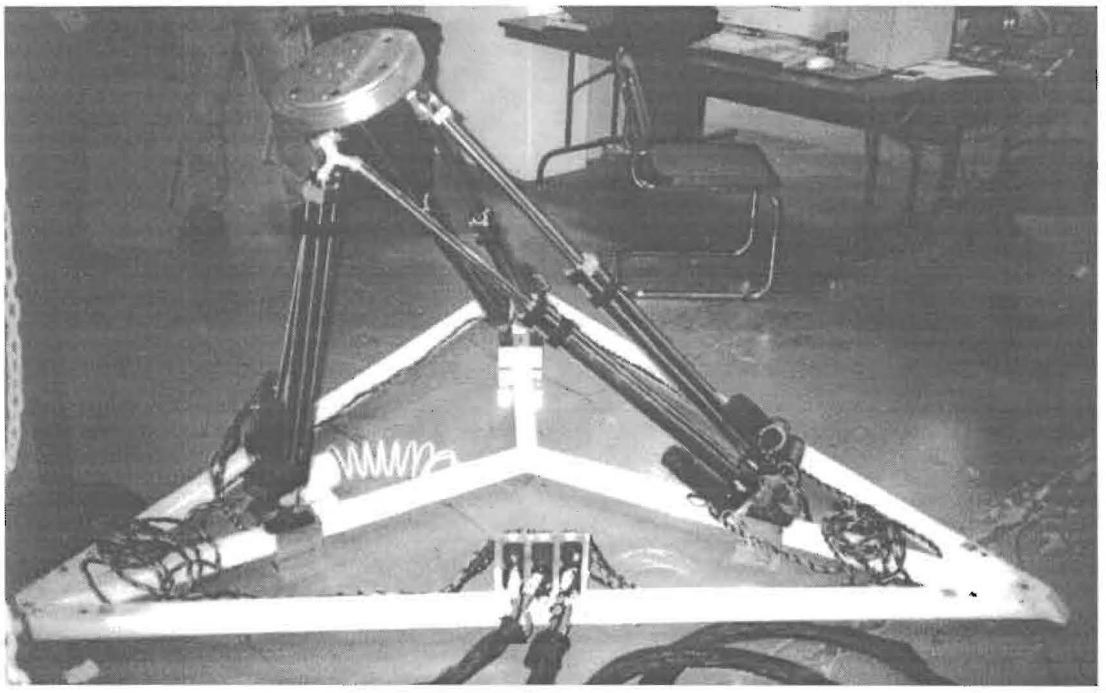

Figure 1.11 Photograph of the *ARRI*-Stewart platform.

Figure 1.12 Photograph of the *ARRI*-upper platform gimbals.

In his review Merlet [4] describes the configuration of a 6–6 Stewart platform which has universal joints connecting the prismatic actuators to the base, and ball-and-socket joints connecting them to the moving platform.

Fichter [17] does the kinematic and dynamic analysis of a general Stewart platform, which he considers as two solid bodies connected to each other via six linear actuators (see Figure 1.13). The connections at both ends of each actuator are ball-and-socket joints.

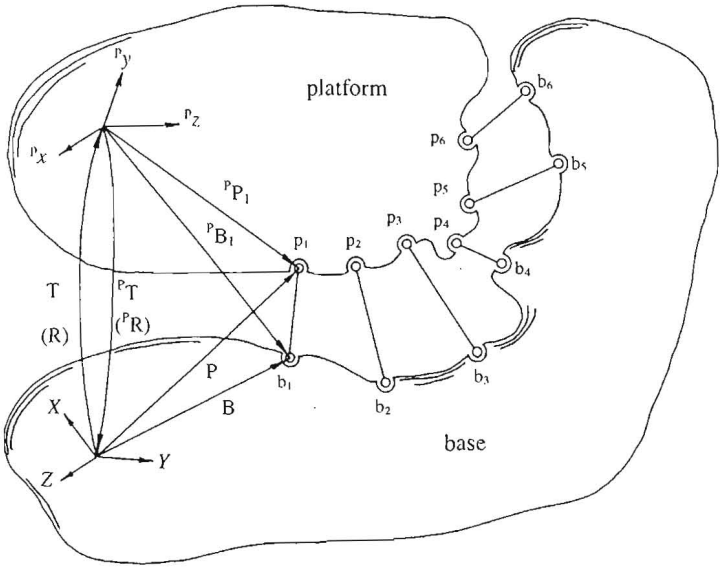

Figure 1.13 A schematical of the generalized Stewart platform (after [17]).

Similar to planar parallel mechanisms, spatial parallel mechanisms can also be designed using rotary actuators. Arai et al. [19] describe a 6–6 parallel manipulator with rotary actuators, as a parallel manipulator having six linkage chains, each consisting of three joints and two links. The first joint (joint 1) is an actuated rotary joint connecting link 1 with the foundation. Joint 2 is a Hooke / universal joint connecting links 1 and 2. Joint 3 is a spherical joint connecting link 2 with the moving platform (see Figure 1.14).

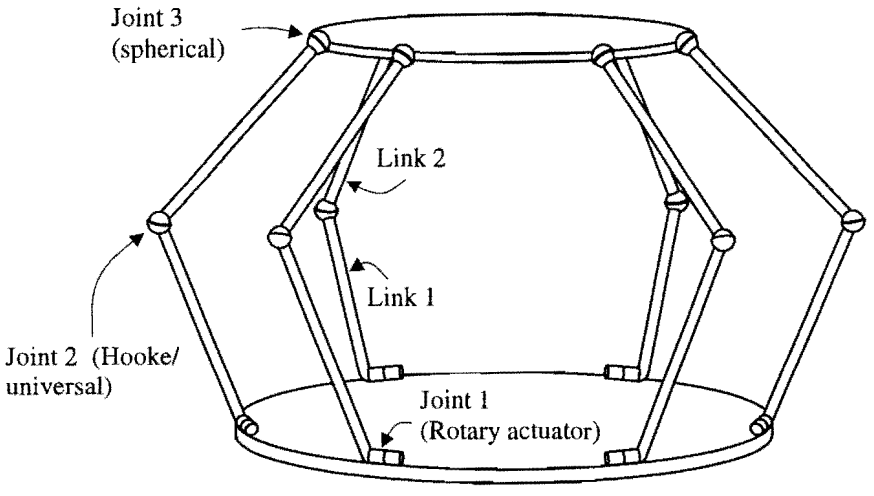

Figure 1.14 Rotary actuated 6-6 parallel manipulator (after [19]).

Arai et al. also point out that these rotary actuated parallel mechanisms have the advantage of good dynamic characteristics, which stems from the fact that the actuators are fixed in the basement, resulting in extremely lightweight movable elements.

Wang and Gosselin [7] studied the kinematics and singularity representation of spatial five DOF parallel mechanisms, with both prismatic and revolute actuators. Both mechanisms consist of six kinematic chains, five of which have the same topology.

Wang and Gosselin first considered the mechanism with the revolute actuators. Each of the five actuated legs consists of an actuated revolute joint connecting the first moving link to the base, a Hooke / universal joint connecting a second moving link to the first link and a spherical joint attaching the moving platform to the second moving link (see Figure 1.15). The five DOF spatial Stewart platform has a Hooke / universal joint connecting each of the five prismatic actuators to the base, and a spherical joint connecting the moving platform to each actuator.

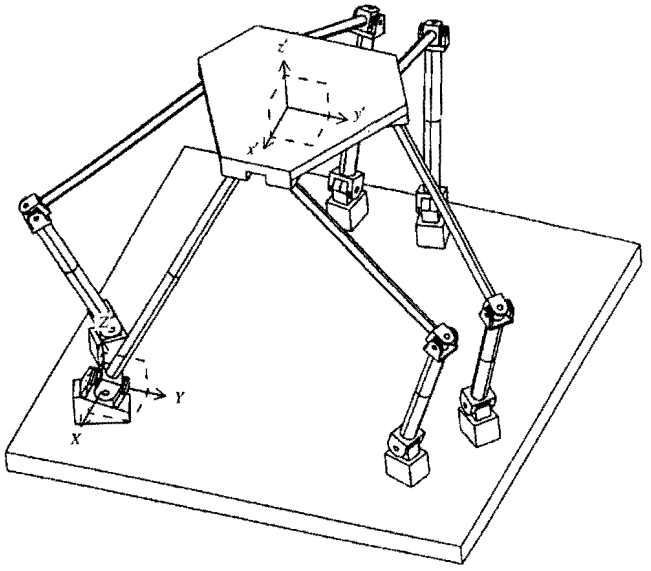

Figure 1.15 The spatial five DOF parallel mechanism with revolute actuators (after [7]).

The sixth kinematic chain of both mechanisms connects the moving platform with the base, and is not actuated. It consists of a Hooke \ universal joint attached to the base, a moving link, and a spherical joint attached to the platform (see Figure 1.15). It follows that the sixth kinematic chain constrains the motion of the platform to five DOF. According to Wang and Gosselin , the five DOF mechanism could also be built using only five legs, i.e. by removing one of the five identical legs, and actuating the first joint of the special leg. Apparently, these two arrangements lead to similar kinematic equations.

Having considered spatial parallel manipulators with revolute links, it is interesting to consider the new parallel manipulator proposed by Arai et al. [19]. The proposed new manipulator is a combination of a standard 6–6 Stewart platform with prismatic actuators, and a 6–6 parallel manipulator with revolute actuators (see Figure 1.16). It has a base plate and an "intermediate platform" connected to each other via six firmly fixed linear actuators, i.e. the position and orientation of the "intermediate platform" cannot change. A movable link is connected via a ball joint to the actuated part of each of the six linear actuators. The other ends of the six movable links are connected via spherical joints to the moving upper platform. As soon as the linear actuators move, the movable links move and the moving upper platform changes its position and orientation. The proposed mechanism is designed to achieve high speed and good accuracy capabilities.

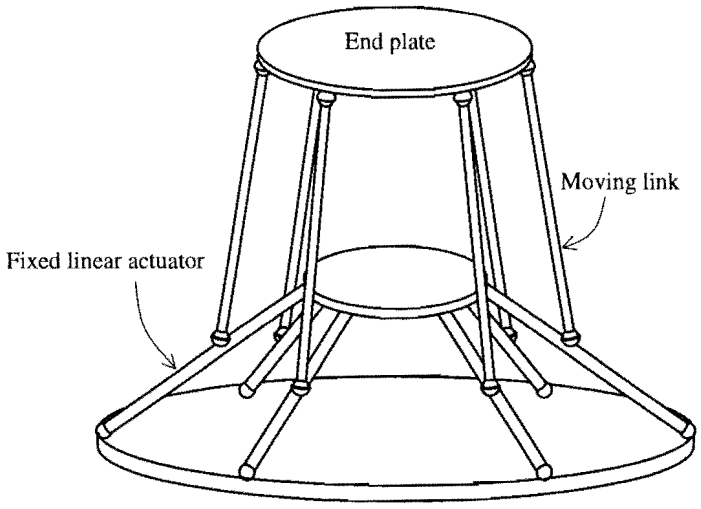

Figure 1.16 New parallel manipulator with fixed linear actuators (after [19]).

Similar to the parallel manipulator with the fixed linear actuators, is the Hexaglide developed at the *Institute of Machine Tools of the Swiss Federal Institute of Technology* in Zurich. According to Honneger et al. [20], who studied the control of this parallel manipulator, the Hexaglide is intended to be used as a high speed milling machine.

The Hexaglide also has six movable links with one end of each link connected to a linear motor. The motors are distributed on three linear rails mounted parallel to each other. The other ends of the moving links are connected in pairs to the triangular moving platform. One could describe the Hexaglide as a special 6–3 parallel manipulator (see Figure 1.17).

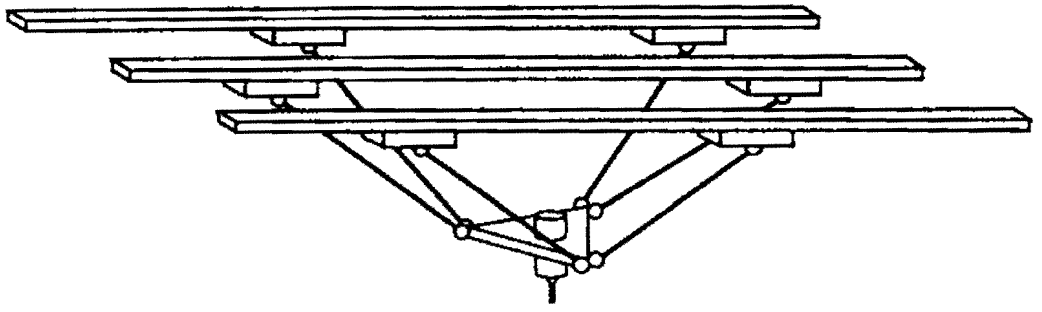

Figure 1.17 The six DOF Hexaglide (after [20])

Another design which is similar to the Hexaglide and the parallel manipulator with the fixed linear actuators, is the three translation DOF parallel manipulator designed by Hervè [21]. Three pairs of parallel links connect the fixed orientation platform with the three linear motors. The three motors run

along three radiating rails. Changing the position of the three motors, causes the moving platform only to translate, as the parallel links ensure the fixed orientation of the moving platform.

An interesting design found in the literature is the reconfigurable platform manipulator designed by Ji and Song [22]. According to them, the mechanical structure of a parallel manipulator is very suitable for reconfiguration, since parallel manipulators are actuated in parallel. The limited workspace of platform manipulators further points to the need for a modular, reconfigurable platform with adjustable configurations, so that the platform will have a wide range of applications.

As part of the investigation into a reconfigurable platform manipulator, an experimental platform was built consisting of a base and mobile plate and six prismatic actuated legs. The base connections are normal two axes Hooke / universal joints, and the moving platform connections are Hooke joints with an additional revolute joint, providing three axes rotation. The base and platform plates of the experimental platform have reconfiguration hole patterns used to connect the actuator leg units to the plates.

The objective of Ji and Song is to develop an inventory of standardized leg modules and customized mobile platforms and base plates, so that the parallel manipulator can be custom-configured, portable and easy to repair.

1.5 AVAILABLE COMMERCIAL PRODUCTS

The research and development of in-parallel devices have enjoyed much attention over the last three decades [5]. However, in spite of this Ji [23] reports as recently as 1996, that the use of platform manipulators is still mainly in an experimental stage. He attributes this to the lack of rational synthesis tools for the design of practical platform manipulators.

Many proposed prototypes, developed by researchers from around the globe, are to be found in the literature on parallel manipulators.

The authors of the *Hexapod* [24] brochure published by Geodetic Technology in the USA, state that the "cost of computing strut lengths has until recently been too high for most (practical) applications. Where the cost of processing could be justified, some interesting hexapod-based machines, such as the flight simulator, were made."

An example of a company that has been involved in the flight simulator is *FRASCA International, Inc.*. They have been in business since 1958, and have developed a wide range of flight simulators, which include Stewart platform mounted simulators.

As far as other applications for parallel manipulators are concerned, it is reported in the *Hexapod* brochure that, "now that the cost of computing strut lengths has fallen dramatically, many companies are offering hexapod-based machines". This is happening in spite of the problems mentioned by Ji [23].

In Merlet's [4] review he states that *Marconi* designed the first commercial parallel manipulator in 1985. This is the six DOF *Gadfly*, designed to be used for the assembly of electronic components. In 1986 *Marconi* designed the *Tetrabot*, a huge hybrid serial-parallel manipulator.

Another company mentioned by Merlet [4] is *Demaurex* who sells the *Delta*, which is a 3-4 DOF manipulator used for very fast pick-and-place tasks involving light loads. Another product is the *Hexa*, which was still under development in 1994. The *Hexa* is a six DOF manipulator based on a design similar to that of the *Delta*. Merlet also mentions a new product, the *SmartTee* which is being developed by *Hughes*.

In his analysis of the design parameters in parallel manipulators, Ji [23] mentions the *NIST Robocrane* capable of manipulating tools and devices to perform a variety of tasks such as cutting, shaping and finishing, excavating and grading.

Ji also list the *Octahedral Hexapod* machine tool developed by *Ingersoll Milling Machines Co.*, which can perform machining operations on large workpieces such as engine blocks. This unique mill consists of a moving tool assembly guided over the workpiece by six ball screw actuators forming a 6–6 Stewart platform as shown in Figure 1.18.

It is reported that modern milling centers such as the *Octahedral Hexapod* machine tool, are capable of 1 m/s velocities over a volume of 1 cubic meter with a resolution of 1 million increments per second. Spindle speeds can be as high as 24000 revolutions per minute.

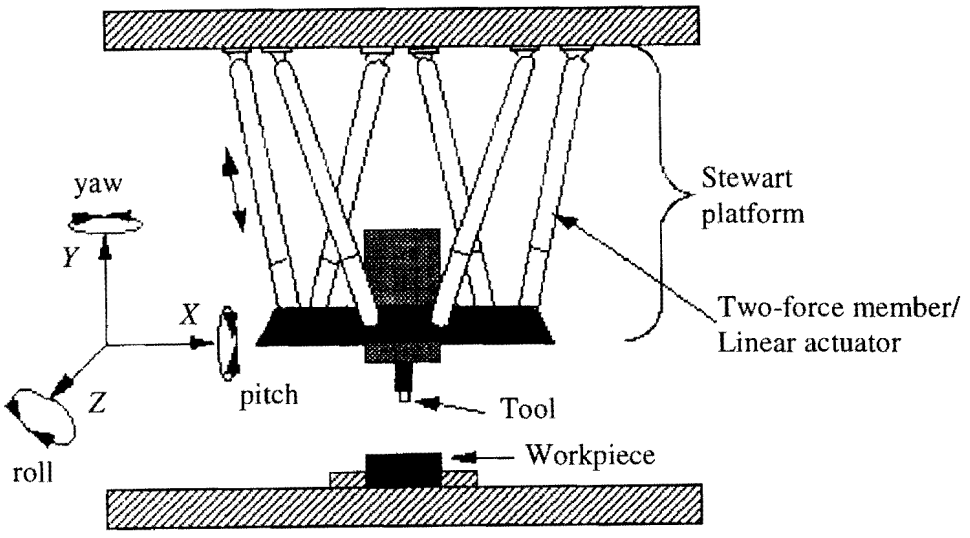

Figure 1.18 Schematic of a Hexapod six-axis machining center.

Zou et al. [25] list a few companies who are specifically involved in designing parallel manipulators used for manufacturing. One of these is the Italian based company *Comau*, who manufactures the *TRICEPT HP*.

The *TRICEPT HP* has three linear actuators, and the end effector is connected to a three-axis wrist, resulting in a total of six degrees of freedom (DOF). According to the manufacturer, the *TRICEPT HP* is a very rigid manipulator, capable of applying a maximum force of 15 kN and lifting up to 500 kg. The wrist can handle a payload of up to 150 kg. Typical applications listed in the technical brochure of the *TRICEPT HP*, includes: assembling with force, deburring, polishing, wood working, aluminum milling, laser and water-jet cutting, as well as spot and laser welding [26].

Zou et al. [25] also refers to *Giddings and Lewis* in the USA, and *Lapik* in Russia. Both companies have apparently developed their own parallel type CNC machine tools.

Geodetic Technology has patented their *Hexapod* 6–3 parallel manipulator (see Figure 1.19) in a number of countries [24]. According to the manufacturer, this machine competes with human adaptability and dexterity. *Geodetic Technology* has been developing hexapod technology since 1988, and it comprises of unique mechanisms, sophisticated control, together with calibration and translation software.

Figure 1.19 The *Hexapod* 6–3 Stewart platform type machine tool (after [24]).

Fanuc Robotics is another company that designed a 6–3 hexapod, the *FLEXTOOL*, which has a base and tooling faceplate connected by six servo actuated legs, resulting in six DOF. The *FLEXTOOL* can precisely move locators, clamps and other end-of-faceplate tooling, to multiple positions for welding and joining [27].

In conjunction with the idea of a reconfigurable Stewart platform proposed by Ji and Song [22], the modular design of parallel manipulators is possible thanks to the German company *INA*. *INA* manufactures high precision joint units, which are ready-to-fit and clearance-free [28]. *INA* also designs telescopic arms, which can be mounted onto precision joints, making the *INA* system ideal for the modular construction of Stewart platforms.

In order to develop hexapod technology as an economical alternative to conventional designs, the *Machine Tool Laboratory (WZL)* of *Aachen RWTH* and the *ISW* of the University of Stuttgart are co-operating with machine tool manufacturers in the research project *"DYNAMIL II"* (Dynamic Innovative Lightweight Designs for Production Machines of the Year 2000) [28]. *INA* is also a partner in this project.

INA is also currently demonstrating the functioning of its joints and telescopic arms for hexapod technology in a reliable machine which was designed by the Institute for Machine Tools of the University of Stuttgart and built jointly by *INA* [28].

1.6 AVAILABLE DESIGN INFORMATION

1.6.1 Introduction

According to Liu et al. [18], there are two fundamental characteristics that set a Stewart platform manipulator apart from other industrial robots: a Stewart platform is a *closed kinematic system* with *parallel links*. These characteristics contribute to the advantages of Stewart platforms.

Wang and Hsieh [29] state that the rigidity and load-carrying capacity of parallel robots are better than those of conventional serial robots. Merlet [4] explains further that the high load / weight ratio is due to the equal distribution of the load on the platform. Each link of a six legged Stewart platform is submitted to only 1/6 of the total weight. Merlet contributes the rigidity of the platform to the stress in the links being mostly traction-compression, which may easily be handled by linear actuators.

According to Merlet [4], another advantage of parallel manipulators is that the position of the end-effector is much less sensitive to the error on the articulated sensors than serial link robots. Geng et al. [30] explain that the reason for the higher accuracy of parallel manipulators is because the positioning error on each actuator is averaged out instead of being accumulated at the end-effector. Merlet [4] also mentions that the high positioning accuracy of these manipulators is also due to their high stiffness, which insures that the deformations of the links are minimal. He emphasizes that the most important advantage of parallel manipulators is their low cost, since mostly standard components can be used. This corresponds to the statement of Geng et al. [30] saying that the mechanical design of the Stewart platform based parallel link manipulator is relative simple. Liu et al. [18] agree, saying that relatively inexpensive commercially available servo actuator technology is used for many Stewart platforms. It is interesting to note that this corresponds to Stewart's [1] original design aims, namely to achieve the most simple and cohesive design with the highest capabilities for a wide range of applications.

The architecture of parallel manipulators is very different from that of serial link manipulators, and Merlet rightfully states that most of the theoretical problems concerning parallel platforms still have to be addressed. According to Merlet, there exists a duality between parallel and serial link manipulators, as easy problems for serial link manipulators are often difficult to solve for parallel manipulators, and vice versa. Merlet mentions the attempts by Waldron and Hunt [31] as well as that of Zamanov and Sotirov [32] to explain this duality.

1.6.2 Kinematic Analysis

Starting in 1987, more and more researchers have become interested in addressing problems concerning parallel manipulators. Merlet [33] points out that, for example, the direct kinematics problem has drawn the attention of many researchers, and is currently still under investigation, as it has not yet been completely solved. Merlet in fact says that Roth, the prestigious researcher of Stanford, has stated that the direct kinematic problem of parallel robots is the "kinematic problem of the century".

Solving the inverse kinematics, i.e. determining the leg lengths once the position and orientation of the top platform are known, is easy to do. Finding the position and orientation of the top platform with the leg lengths known is, however, far more complicated. Researchers have experimented with different techniques to solve the forward direct kinematics with the objective of obtaining the closed form solution for the general 6–6 parallel manipulator. Merlet [4] states that the closed form forward kinematic solution for some special configurations of spatial manipulators has been found, but as yet, no success has been reported for the general 6–6 parallel manipulator. This is confirmed by Innocenti [34] who also mentions that in spite of their relatively simple arrangement, the kinematic analysis of fully-parallel mechanisms is extremely challenging.

The emphasis currently lies on finding the analytical or closed-form solution of the forward kinematics. A closed-form solution is most desirable since it generally reduces the problem to solving one algebraic equation with only one unknown. Accordingly, the degree of the equation provides the number of platform locations in the complex field, and the locations themselves can be found by determining all roots of the equation.

Geng et al., for example, state that in general for a set of leg lengths, the forward kinematics problem can have no solution, or multiple solutions. They also categorize the different approaches used to solve the forward kinematics into iterative (numerical) methods and direct (closed form) solutions. Merlet [4] also states that in general, the forward kinematic analysis has more than one solution.

Innocenti [34] explains that when performing the direct positional analysis of a mechanism, the displacement values of all actuated kinematic pairs are known. Accordingly, all actuators can be thought of as frozen, and the mechanism itself can be regarded as a structure. The direct kinematics of the mechanism is then equivalent to finding all closure configurations of the structure.

Griffis and Duffy [15] point out that the forward displacement analysis of parallel manipulators is important, as it will provide feedback information, i.e. the position and orientation of the moving platform relative to the base, which can be used in a Cartesian controller. They further state that the use

of a Stewart platform as a force / torque sensor in the field of force / control, will be enhanced by a forward analysis of a Stewart platform. Geng et al. [30] also report that in general, the forward kinematics is used in a position feedback control problem, where the lengths are measured by sensors mounted on the actuators.

In their 1993 article, Liu et al. [18] state that the lack of efficient algorithms for solving the kinematic equations is the main obstacle in realizing the potential of the Stewart platform as an industrial robotic manipulator.

The fact that multiple solutions exist for the direct kinematics of a Stewart platform makes the interpretation of the results an important factor. Liu et al. also state that among the solution sets of the forward kinematics, only some are feasible due to mechanical constraints. They distinguish between "mathematical" solutions and "mechanical" solutions of the forward kinematics problem.

1.6.3 Workspace Analysis

1.6.3.1 General Observations

From the geometry of a parallel manipulator, it follows that it is the limited ranges of the actuator legs that determine the size of the workspace. For Stewart's [1] original design, he explains that similar movement of all three legs in the *XYZ* coordinates, results in *XYZ* motion of the platform, and differential movement results in attitude (rotational) movement of the platform. From this Stewart directly relates the linear displacements of the platform, to the amplitude of movement of the legs, and the angular motions are proportional to the spacing of the three points on the platform, relative to the linear motions of the legs. It follows that the smaller the platform size relative to the stroke of the legs, the larger the angular motions.

The determination of parallel manipulator workspaces has come a long way since Stewart [1] did the motion analysis of his flight simulator parallel mechanism in 1965. However, in a recent article Merlet et al. [14] state that the workspace determination of parallel manipulators remains a challenging problem. The solution of this problem is very important in the design and trajectory planning of parallel manipulators. Kumar [11] also states that the point based definition of the workspace is an important design consideration and of considerable theoretical significance.

According to Gosselin [35], many authors have pointed out that the major drawback of parallel manipulators is their limited workspace. He further states that it is therefore of primary importance to develop efficient tools that will allow the determination of their workspace. Moreover, in the context of design, the workspace determination procedure should be simple enough to be included in an

optimization cycle in which, for example, the size of the workspace may be maximized with regard to design variables.

The successful mapping and characterizing of the workspace also assist in eliminating the mechanically infeasible solutions of the forward kinematics. It is indeed believed that the lack of understanding the workspace is a major obstacle in the development of the Stewart platforms into practically useful industrial robots (see Section 1.7).

Unfortunately the determination of the workspace is one of the dualities of serial and parallel manipulators mentioned in Section 0. This corresponds to Kumar's [11] statement that, compared to the research work on workspaces of serial manipulators, much less work has been reported on parallel manipulators. Kumar also says that although parallel manipulators are increasingly being used in robotics research, there is very little evidence of any general approach to workspace analysis and characterization of the reachable and dextrous workspace (defined in Section 1.6.3.6) of such manipulators

Merlet [4] explains that the problem with representing the three dimensional workspace of a spatial manipulator, is that the workspace cannot be de-coupled in two three dimensional workspaces characterizing the possible translational and orientational motions. Although there is no human readable way to represent the complete workspace, some projections of the full workspace can be drawn. He further reports that some researchers represent the possible translations of a parallel robot in a plane, for a fixed orientation and altitude of the mobile platform. Fichter [17] does this simulating the Stewart platform at different points in the Cartesian space. Merlet recommends the use of a geometric algorithm which can take into account the limited range of the actuators, the mechanical limits of the passive joints and the link interferences.

Another technique used to represent and characterize the workspace, is to consider the possible rotation of the end effector around a fixed point. This method is proposed by Merlet, and apparently it takes into account all the constraints limiting the workspace.

In his review, Merlet [4] also reports that he has solved a corollary problem, namely that of verifying that a straight line trajectory lies fully inside the workspace of a parallel manipulator. It is further stated that Merlet addressed the problem of determining the dimensions of a parallel robot so that the corresponding workspace includes a specified task-space.

The workspace boundaries of various planar and spatial parallel manipulators have been studied in the literature using different methods. Some of the more important and interesing methods proposed to date is discussed in the remainder of Section 1.6.3.

1.6.3.2 The Work of Bajpai and Roth

Bajpai and Roth [10] present and analyze the basic kinematic geometry and workspace properties of the simplest closed-chain manipulator, with revolute joints, that can be used to position a point in space. The planar, revolute jointed, five bar chain considered is shown in Figure 1.20.

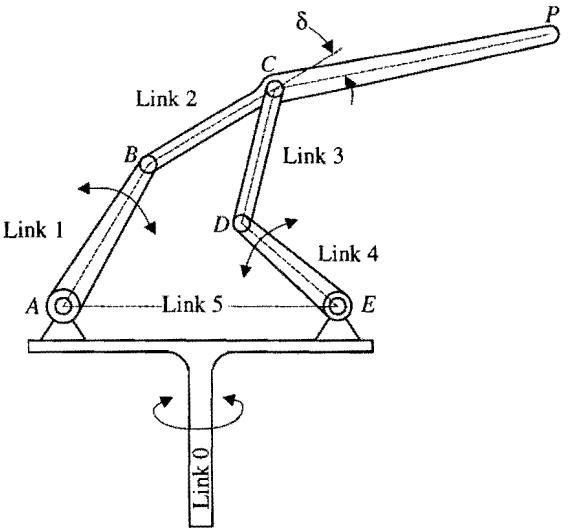

Figure 1.20 Closed loop manipulator with revolute joints (after [10]).

In their analysis of the closed loop manipulator, they emphasize the influence of the link lengths on the reachable workspace. They also comment that unlike the commonly used open-loop manipulators, the entire workspace of a closed-loop manipulator will not in general be freely reachable. Bajpai and Roth derive the conditions for which the complete independent mobility of the driving links of the five bar chain exist. In the end, they are able to suggest a few design rules to be considered when closed loop manipulators are to be built.

1.6.3.3 The Geometric Method of Merlet and Co-workers

The geometric methods introduced by Bajpai and Roth in 1986, are also used by Merlet et al. [14] in a recent article where they consider the workspaces of planar parallel manipulators. The planar three DOF parallel manipulators they consider, are composed of three kinematic chains connecting the mobile platform to the fixed base. It follows that different types of manipulators are obtained depending on the nature of these chains. In particular, they consider the 3-*RPR* manipulator, where the mobile platform is connected to the base via three identical chains (see Figure 1.7). Each chain consists of a revolute joint

(R) attached to the ground, followed by an actuated prismatic joint (P), which is connected to the platform by a revolute joint (R).

They define a fixed reference frame on the base, and a moving reference frame is attached to the platform with its origin fixed at point C. The position of the moving frame is defined by coordinates of point C in the fixed reference frame, and its orientation is given by the angle θ between one axis of the fixed reference frame, and the corresponding axis of the moving frame. Merlet and his co-workers further define an *annular region* as the region which lies between two concentric circles with different radii. It follows that the circle with the largest radius will be referred to as the external circle, and the smaller circle will be referred to as the internal circle. The internal circle may not exist. The assumption is made that no mechanical interference can occur between the links.

The first "type" of workspace considered, is the "constant orientation workspace". This workspace is defined as the region, which can be reached by point C when the orientation of the moving platform is kept constant. For any position of C on the boundary of the workspace, at least one of the link lengths should be at its extreme value. If this it not the case, the platform may move in any direction, and therefore C cannot be located on the boundary of the workspace.

In determining the fixed orientation workspace, the region which can be reached by the endpoint of one of the actuator legs B_i is considered. This region is an annular region ε_i, centered at A_i, i.e. the base point of leg i. The external circle has a radius corresponding to the maximum actuator leg length, and similarly the internal circle has a radius corresponding to the minimum actuator leg length.

Any specific fixed orientation workspace will therefore be the intersection of the three annular regions of point C. similarly, if the revolute joints attached to the ground cannot fully rotate, then point C will only be able to reach an angular sector, and the fixed orientation workspace will be the intersection of the three angular sectors.

Examples of fixed orientation workspaces, as determined by Merlet and his co-workers, are shown in Figure 1.21.

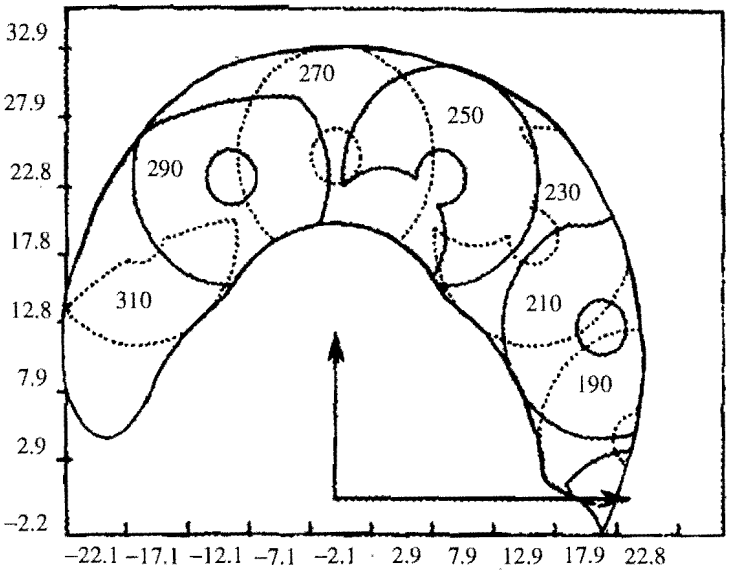

Figure 1.21 Examples of constant orientation workspaces of one of the planar Stewart platform considered by Merlet et al. (after [14]).

They also consider the maximal workspace which is defined as the region the reference point C can reach with at least one orientation. They state that the maximal workspace depends upon the choice of the reference point on the moving platform, and their objective is to geometrically determine the boundary of the maximal workspace. The maximal workspace of another of the manipulators considered by Merlet et al. is shown in Figure 1.22.

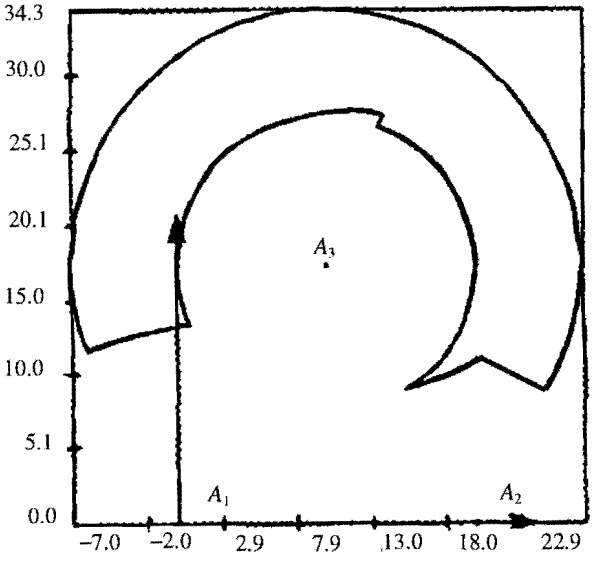

Figure 1.22 An example of the maximal workspace of a planar Stewart platform determined by Merlet et al. (after [14]).

They continue to describe how their geometric algorithms can be applied to determine various other "types" of workspaces. The *inclusive workspace* is defined as the set of all the positions, which can be reached by the reference point, with at least one orientation of the platform in a given interval. This inclusive workspace is obtained from the constant and reachable workspaces. The *total orientation workspace* is also determined, i.e. the region which can be reached by point *C* with every orientation of the platform in a given range. Finally the *dextrous workspace*, which is a particular case of the total orientation workspace, is also determined. This is the region that can be reached by the reference point with any orientation in a given range.

1.6.3.4 Gosselin's Method of Spheres

Moving onto spatial manipulators, Gosselin [35] proposed an algorithm for the determination of the workspace of a parallel mechanism, using a method based on the geometric properties of the workspace. Gosselin points out that many of the methods to determine the workspace of a spatial six DOF parallel manipulator, are based on a complete sampling of the Cartesian space. Instead, Gosselin geometrically obtains the workspace, i.e. the region of the three dimensional Cartesian space that can be attained by the manipulator with a given orientation of the platform.

Gosselin states that, if mechanical interference is neglected, the boundary of the workspace is attained whenever at least one of the actuators reaches one of its limits. This corresponds to the work of Merlet et al. [14] on planar manipulators.

For a given fixed orientation of the platform, the portion of the three dimensional Cartesian space attainable by *i*-th leg is circumscribed by the concentric spheres of radii ρ_i^{min} and ρ_i^{max}. It follows that ρ_i^{min} is the minimum reach of actuator leg *i*, and ρ_i^{max} the maximum reach.

For the given fixed orientation the center of the spheres does not coincide with the center of the joint connecting the *i*-th leg to the base. Considering the local reference frame, which is connected to moving platform, the vector to the platform connection of leg *i* is subtracted in the local reference frame from the base connection of leg *i* to find the center of the spheres (see Figure 1.23).

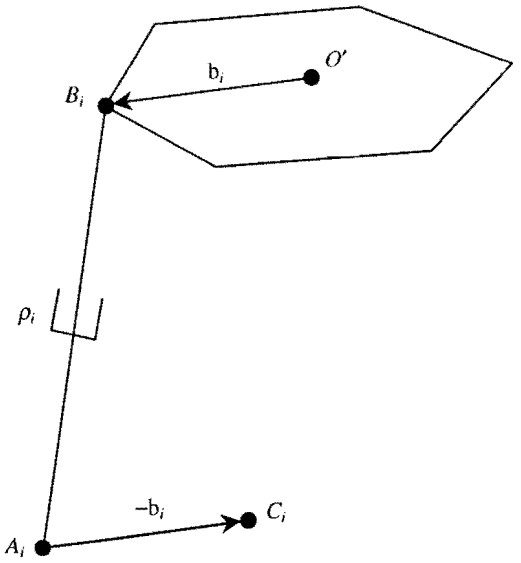

Figure 1.23 Location of the center of the spheres used to compute the workspace (after [35]).

For a given orientation of the platform, the workspace of the parallel manipulator in three-dimensional Cartesian space can be described as the intersection of six regions, each of these regions being the difference of two concentric spheres. Six pairs of concentric circles will be obtained if the intersection of the spheres with a horizontal plane is considered (see Figure 1.24). The intersection of the six annular regions is the section of the workspace contained in the plane.

Gosselin derives an algorithm to find the intersection of the six annular regions, keeping in mind that the boundary of each section will be made up of circular arcs, i.e. portions of circles (see Figure 1.25). Since Gosselin obtains the list of circular arcs, the area of the workspace section can accurately be determined by performing an integration process along the boundary. When the areas of the series of parallel planes are obtained, the volume of the workspace can be obtained by numerically integrating the area of the "slices" containing the workspace sections.

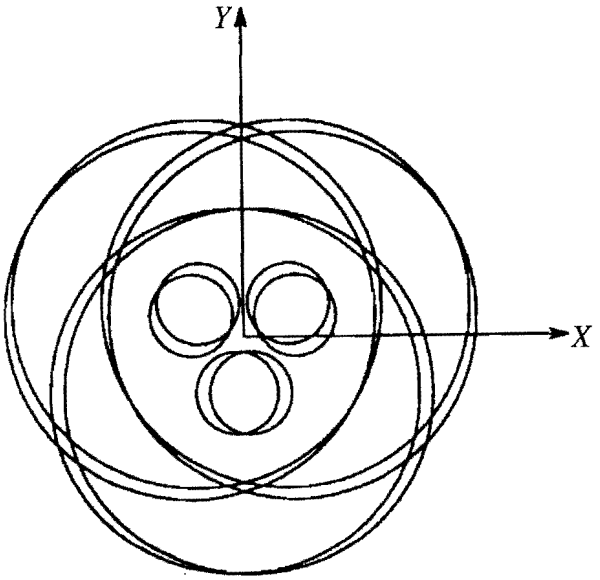

Figure 1.24 An example of the six concentric circles obtained if the intersection of the spheres with a horizontal plane ($z = 512$ mm) is considered (after [35]).

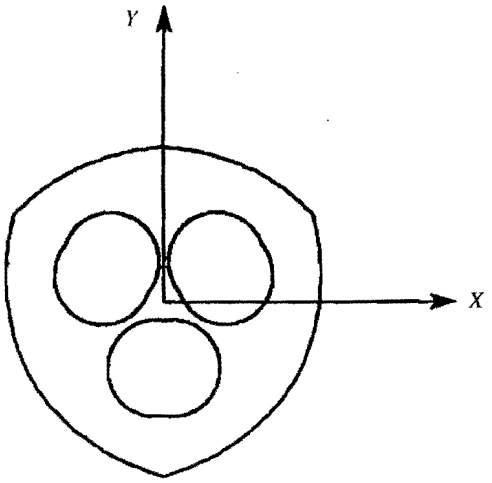

Area = 55168 mm^2

Figure 1.25 Boundary of the workspace for $z = 512$ mm (after [35]).

Gosselin also demonstrates the ability of his method to determine the workspace of a spatial mechanism. As a representative example, the workspace of the parallel manipulator developed at the French national institute for research in computer science and control (*INRIA*) has been studied [35]. The *INRIA* prototype is a six DOF fully parallel manipulator, and the volume of the workspace was also determined (see Figure 1.26).

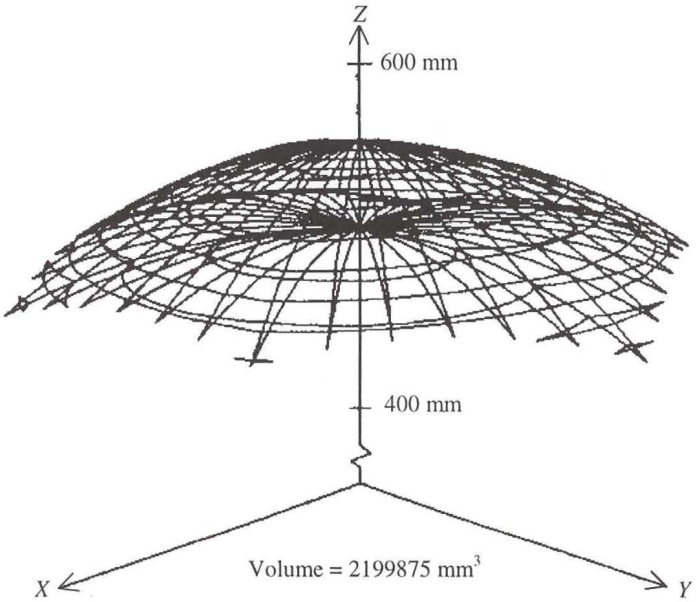

Figure 1.26 Boundary surfaces of the reachable workspace of the *INRIA* manipulator (after [35]).

1.6.3.5 Kumar's Method Based on Screw Theory

In his attempt to characterize the workspaces of parallel manipulators, Kumar [11] defines the *reachable workspace* as the volume or space within which a reference point on the hand or end effector can be made to coincide with any point in space. The reference point on the manipulator end effector is on the workspace boundary when the manipulator is at full extension in any direction. Because the end effector does not possess the ability to translate along the direction of maximal extension, the manipulator is at a positional singularity.

Kumar uses screw theory to express the necessary condition for the end effector to be on the workspace boundary. This condition can be expressed as: the instantaneous joint screws all being reciprocal to a zero pitch screw through the reference point on the end effector along the direction of full extension.

From a geometrical viewpoint, a parallel manipulator is considered to be a collection of n serial manipulators all of which have a common base and end effector. The i-th chain possesses m_i single DOF revolute joints each capable of 360° rotation.

Kumar isolates the i-th serial chain, and denotes its reachable workspace as R_i, i.e. the workspace of the resulting serial manipulator once the other $n-1$ chains have been removed. The resulting serial manipulator consists of the base, the links in the i-th chain, and the end effector.

Kumar points out that the configuration in which the joint screws are reciprocal to a zero pitch screw passing through the reference point does not necessarily imply that the reference point lies on a boundary. When the reference point of a parallel manipulator is at the workspace boundary, all the twists available to the end effector, (about which the end effector can twist), are reciprocal to a zero pitch wrench whose axis passes through the reference point on the end effector.

In general, there is a set of k possible configurations that satisfy the condition of reciprocity to a zero pitch screw through the reference point. For a serial chain with m joints, $k = 2^{(m-1)}$. The method Kumar uses to generate the workspace boundary, consists in basic terms of finding all of the k possible configurations, and determining which loci of the reference point are on the workspace boundary. There is a special consideration in order to accommodate mechanisms in which all joint screws span a screw system of order less than six (for example a planar mechanism).

The first example considered by Kumar, is a five bar linkage, which is a two DOF parallel manipulator similar to the one analyzed by Bajpai and Roth [10] and shown in Figure 1.20. The manipulator consists of two serial chains, a 2-*R* (Link 1 in Figure 1.20) and a 3-*R* chain (Links 3 & 4 in Figure 1.20). For a given position of the reference point *P* in Figure 1.20, the 2-*R* chain assumes one of two configurations, and for each configuration, the 3-*R* has two possible configurations. Hence, there are $2^2 = 4$ possible solutions for the inverse kinematics. The direct kinematics has two solutions.

If a zero pitch wrench is applied at the end point, and swept through 360° in the plane, the workspace boundaries can easily be traced (see Figure 1.27).

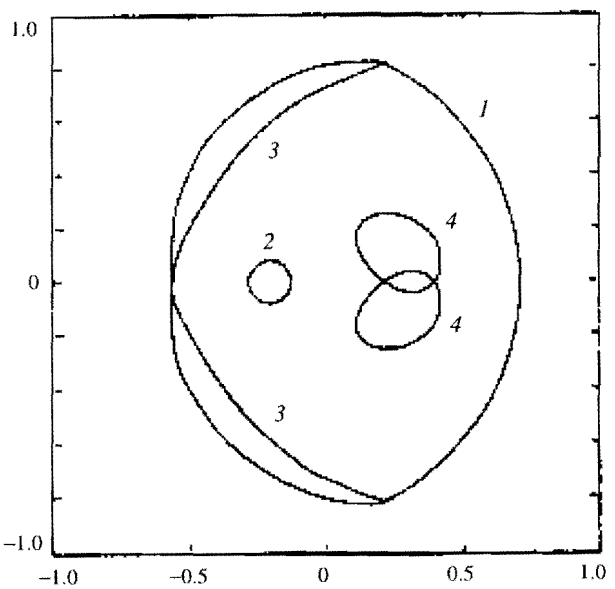

Figure 1.27 The workspace boundaries of the two DOF planar parallel manipulator (after [11]).

The second example considered by Kumar, is a three DOF planar parallel manipulator, where the end effector is constrained by three serial chains each of which possesses three revolute joints as depicted in Figure 1.4.

Having 3-*R* chains, results in $2^3 = 8$ possible solutions for the inverse kinematics. The number of solutions or closures to the direct kinematics, is at most six. The boundary of the workspace of this mechanism consist out of contours generated from analytically derived algebraic expressions, since they are arcs of circles or parts of coupler curves of which explicit closed form expressions exist (see Figure 1.28).

In determining the dextrous workspace of a parallel manipulator, Kumar proves that if the reference point of a parallel manipulator is at the boundary of its dextrous workspace, there exists at least one chain such that a zero pitch screw is reciprocal to all the joint screws in that chain.

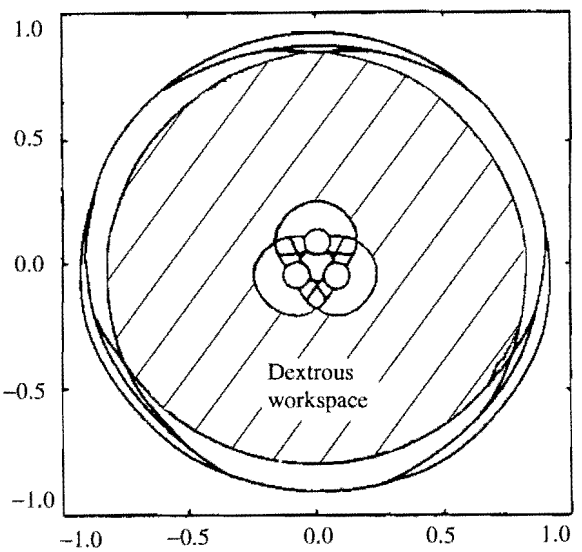

Figure 1.28 Workspace boundary of the planar three DOF parallel manipulator (after [11]).

After the workspace boundary is computed, Kumar identifies the closed regions that are completely bounded by workspace contours. Each closed region is then tested for dexterity, i.e. for a particular region any convenient point Q is tested: Firstly the ability of the manipulator to provide all attitudes of the end-effector with the reference point at Q is tested, and secondly for all attitudes of the end effector, the ability to complete a 360° rotation about any (all) axis (axes) through Q is tested.

As an extension to the definition of the dextrous workspace, Kumar also defines the controllable dextrous workspace. "A point Q belongs to the controllable dextrous workspace if: (a) the reference point of the end effector can reach Q, (b) the manipulator can provide the end effector any (every)

attitude with its reference point at Q, and (c) for any reference attitude of the end effector, the manipulator can produce a complete rotation of the end effector about any (every) axis through the reference point, such that , during the rotation, the end effector does not *lose* or *gain* a degree of freedom."

1.6.3.6 Haug et al.'s Continuation Method

So far each proposed method successfully determines the workspaces of a certain type of manipulator. Haug et al. [12] suggest a more broadly applicable numerical algorithm for mapping the boundaries of manipulator workspaces.

In simplest terms, the initial step of their numerical method consists of the non-trivial task of finding an initial point on the workspace boundary. Starting from an assembled configuration of the manipulator, a unit vector **c** in the output-space is selected, and the ray emanating from the starting point along vector **c** is traced until the workspace boundary is encountered. Once a boundary point is found, they use a continuation method to proceed stepwise along the solution curve. A computer code is implemented in the final stage of their method to map the boundary of the accessible output set, until a closed trajectory is found. The continuation method is extended to accommodate bifurcation points, where more than one solution curve intersect.

A planar redundantly controlled serial manipulator, a planar Stewart platform and a spatial Stewart platform are analyzed by Haug and his co-workers. They determine both the exterior boundary of the accessible output set, as well as the exterior-interior bifurcation point connecting curves. They suggest that these "interior" curves often represent local impediments to motion or controllability and are therefore of practical importance.

As an extention to the work done on determining the reachable workspace boundaries of various manipulators, Haug et al. [8] also analyzed the dextrous workspace of manipulators. Apparently Kumar and Waldron [36] introduced the concept of a dextrous workspace. The dextrous workspace is a space within which every point can be reached by a reference point on the manipulator's hand (end-effector), with the hand (end-effector) in any desired orientation. The importance of the dextrous workspace lies in the statement of Haug et al. [8] that "methods for characterizing the region in space in which a manipulator can both position and control the orientation of a working body, throughout specified ranges of inputs and outputs are not well developed."

Haug and his co-workers [8] address the existing need for characterizing the region in space in which a manipulator can both position and control the orientation of a working body, throughout specified ranges

of inputs and outputs. One of the objectives of their research is to define analytical criteria for the boundary of the set of points that can be reached by a given point on the working body. Throughout the set of points, specified ranges of rotation of the working body must be achieved.

It is of practical interest and importance to note that, as stated by Haug et al. [8], the necessary conditions for boundaries of dextrous workspaces are often less complex than associated conditions for the boundaries of workspaces without any dexterity requirement. This is consistent with experience in constrained optimization, where the introduction of additional constraints causes the boundary of the feasible solution set, in the present case the dextrous accessible output set, to become more regular and in many cases easier to compute.

Considering that the determination of workspaces of planar parallel manipulators is already a challenging problem to solve, the situation worsens significantly when spatial manipulators are considered. To handle general parallel robots with arbitrary link geometry, a numerical approach is essential. The numerical approach suggested by Haug et al. [8, 12] is very complicated and not easily implemented.

1.6.3.7 The Method of Wang and Hsieh

Wang and Hsieh [29] present what they call "a systematic method for the numerical analysis of the extreme reaches, and reachable workspace of general parallel robots". They formulate an *optimization problem* in order to find the extreme reach of the manipulator. The distance between the center of the end-effector, and a fixed base point with respect to any given search direction is maximized or minimized depending on the desired objective.

In their article, Wang and Hsieh refer to Haug et al.'s [8, 12] continuation numerical method for determining the workspaces of multi-body mechanical systems. They point out that explicit expressions of the constraint equations and Jacobian matrix of the mechanism is necessary if Haug's method is to be used. It may be difficult to derive these expressions for general parallel robots having complex coupled kinematic loops and multi-DOF joints.

Wang and Hsieh handle the kinematic constraint equations in an implicit and systematic way, and their method does not require the computation of the constraint Jacobian matrix. Various types of joints are taken into account and the advantages of efficient recursive computational schemes are exploited.

The extreme reach is defined as the extreme distance between a base point and the center point of the end-effector. Wang and Hsieh denote l as a straight line defined by a fixed base point B and a unit vector $\mathbf{u}$. The reachable workspace boundary is intersected by the straight line l as shown in Figure 1.29.

The current position of the end effector is $\mathbf{P}_{OC}(\bar{\mathbf{q}})$, in which $\bar{\mathbf{q}}$ is the joint variable vector. The objective is to find the farthest (or nearest) position with respect to B that the center point C of the end effector coincident with l without violating the kinematic constraints.

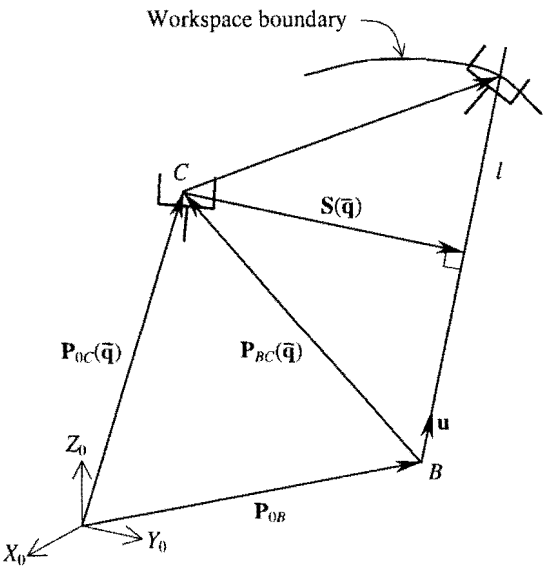

Figure 1.29 Definition of the extreme reach (after [29]).

The perpendicular distance from C to l is given by $\mathrm{S}(\bar{\mathbf{q}})$. Wang and Hsieh formulate the problem of finding the extreme reach as follows: "Find the optimum value of $\bar{\mathbf{q}}$ that maximizes (or minimizes) the Euclidian norm of $\mathbf{P}_{BC}(\bar{\mathbf{q}})$, subject to $\mathrm{S}(\bar{\mathbf{q}})=0$ and the kinematic constraints of the closed loops of the driving mechanisms." The search direction $\mathbf{u}$ (see Figure 1.29) is maintained by means of the equality constraint $\mathrm{S}(\bar{\mathbf{q}})=0$, ensuring that the perpendicular distance from C to l is zero.

Using this problem formulation, the boundaries of the reachable workspace are determined by slicing the space into equally spaced horizontal planes along the vertical axis. The intersection point of the plane and the vertical axis is used as the base point from which the maximum and minimum reaches are determined (see Figure 1.30).

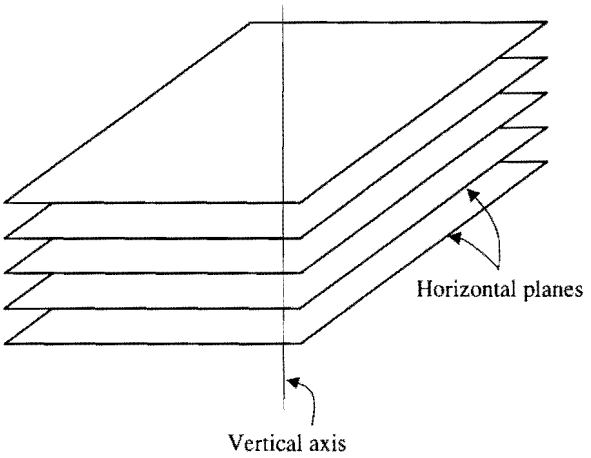

Figure 1.30 Space slicing strategy (after [29]).

The search directions lie on the plane, and are constantly incremented until a closed envelope is determined for each horizontal plane (see Figure 1.31).

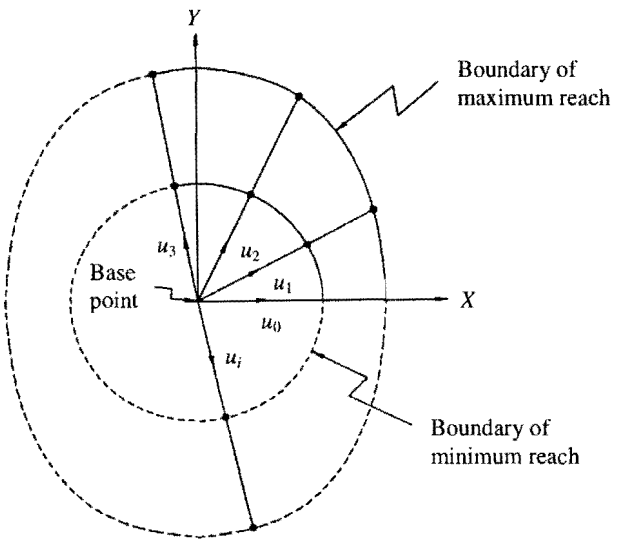

Figure 1.31 Workspace boundaries of a plane (after [29]).

Finally three dimensional curve fitting techniques are used to plot the boundary surfaces of the reachable workspace.

The objective function of the constrained nonlinear optimization problem constructed by Wang and Hsieh is:

$$\underset{\bar{q}}{\text{minimize}} \left\| K\mathbf{u} - \mathbf{P}_{BC}(\bar{\mathbf{q}}) \right\|^2$$

Where the constant K depends on whether the maximum or minimum reach has to be found. For the maximum reach, the value associated with K is very large so as to overestimate the maximum reach of the manipulator. The minimum reach is found by setting $K = 0$.

A combined solution procedure is used to solve the above highly non-linear optimization problem. Instead of using an ordinary steepest decent method, Wang and Hsieh uses a combined method which first uses the cyclic coordinate descent (CCD) method to find a good approximation to the solution vector, and then uses a quasi-Newton method to converge to the solution to the desired degree of precision.

Although the proposed method is numerically stable and computationally efficient, multiple local optimal points may exist so that there is no guarantee that the method will converge to the global solution. The reason for the different possible local optimal points is the fact that the kinematic loops may be closed in several different configurations, and each may end up in a different extreme reach. Wang and Hsieh suggest that this complication be overcome by solving the optimization problem for various initial approximations. The best solution among the alternatives may then be picked.

Wang and Hsieh consider, as an example, a platform-type parallel robot which has six revolute joints, six universal joints and six spherical joints (see Figure 1.32). The center points of the universal joints and spherical joints coincide with the vertices of the platforms. The three dimensional workspace boundaries obtained, as well as the working areas at different planes, are shown in Figure 1.33.

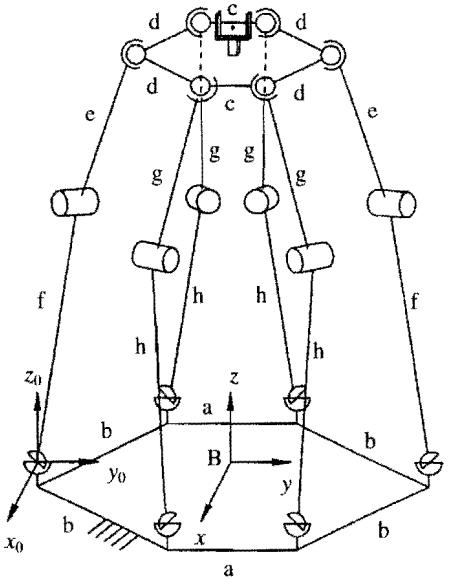

Figure 1.32 A platform type fully parallel robot (after [29]).

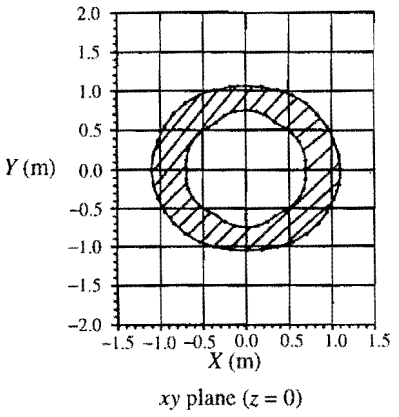

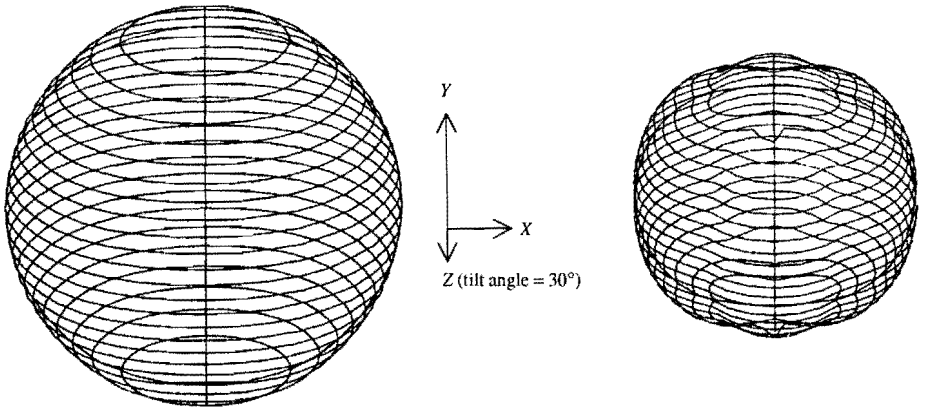

Figure 1.33 Boundary surfaces of the reachable workspace determined by Wang and Hsieh [29].

1.7 MOTIVATION FOR THIS STUDY

Merlet concludes his 1994 review of the development of parallel manipulators by saying: "Parallel manipulators present various advantages which can be useful in many robotic tasks. Although interesting theoretical problems remain to be solved, the current state of the art has enabled prototypes and commercial manipulators to be designed. Although the concept of a parallel manipulator is too recent and too different from the design of most classical manipulators to be widely accepted and frequently chosen by the designers of robotic systems, it is strongly felt that their use in many robotic tasks is so necessary that they will become indispensable in the near future".

Unfortunately this promise has, as yet, not been fulfilled. In fact, as recently as 1996 Ji [23] states that the use of platform manipulators is still mainly in an experimental stage. The biggest reason for this seems to be the lack of rational synthesis tools for the design of practically useful platform manipulators.

In particular, as is evident from this survey, the problems of the forward kinematics and workspace determination remains to be satisfactorily solved. This study addresses the latter problem. It is believed that if the workspace is understood and its characterization properly done, then many design problems will easily be solved. In particular, workspace characterization will assist in solving design problems relating to, amongst others, the determination of the relative sizes of the platforms; the positioning of the joints; the determination of acceptable ranges of translation and rotation for which the platform is stable; the determination of the ranges of leg displacements, and in assessing the problems caused by leg interference.

The literature reports on a number of different methods for the determination of the manipulator workspaces. Some of the more important methods are summarized in Section 1.6.3. Each approach has its own advantages, but all the proposed methods appear to be complicated in one way or the other, and cannot be generally applied to a wide range of platform devices. The urgent need therefore exists for a general, yet easily implemented methodology for the determination and characterization of manipulator workspaces.

In this study a novel optimization approach to solving the workspace problem is introduced. An attempt is made to demonstrate that this approach is not only general, but may also be easily implemented to determine various types of accessible workspaces.

Finally it should be mentioned that, although the approach presented here was independantly conceived, it has certain features that are philosophically similar to that of the recent optimization method of Wang and Hsieh [29], and which is summarized in Section 1.6.3.7.

Chapter 2

2 AN OPTIMIZATION APPROACH TO THE DETERMINATION OF PLANAR MECHANISM WORKSPACES

2.1 INTRODUCTION

In this chapter an optimization approach is used to determine the workspace boundaries of two different types of planar mechanisms. The proposed optimization approach is a new and easily implemented numerical approach, which is based on a novel constrained optimization algorithm that has the considerable advantage that it may easily be automated.

The work presented here is motivated by, and stems from, the foundation paper of Haug et al. [12] which represents the state-of-the-art of computing workspaces of manipulators by the continuation method. In their paper, Haug and his co-workers emphasize the need for refined computer codes by means of which workspaces may easily be obtained.

In this chapter accessible output sets for manipulators are defined and criteria for determining their boundaries are stated. A method, based on the definition of the boundary, is developed by means of which the boundary may be mapped. In simplest terms the method consists of finding a suitable initial radiating point(s) in the output coordinate space, and then determining the points of intersection of a representative pencil of rays, which emanates from the radiating point(s), with the boundary of the accessible set. The points of intersection are determined through an optimization approach in which a proven robust dynamic constrained optimization algorithm of Snyman [37, 38] and Snyman et al. [39] is used.

The planar examples considered here are purposefully chosen to be identical to that of Haug et al. [12], so as to allow for a valid assessment of the new approach. In particular, the method is illustrated by its application to a planar Stewart platform and a planar redundantly controlled serial manipulator.

2.2 ACCESSIBLE OUTPUT SETS

In accordance with Haug et al. [12], *generalized coordinates* $\mathbf{q} = [q_1, q_2, ..., q_{nq}]^T \in R^{nq}$ are defined that characterize the position and orientation of each body in the mechanism. In the neighborhood of an *assembled configuration* of the mechanism, generalized coordinates satisfy m independent holonomic *kinematic constraint equations* of the form:

$$\Phi(\mathbf{q}) = \mathbf{0} \tag{2.1}$$

where $\Phi : R^{nq} \rightarrow R^{m}$ is a smooth function.

Mechanisms are usually designed to produce a certain functionality, where the motion of the mechanism is to be controlled by specifying the values of selected generalized coordinates, called *input coordinates*. As described by Haug et al. [12] these coordinates form a subset of the mechanism generalized coordinates, and their values are controlled by external influences with the intent of controlling the motion of the mechanism. The vector of input coordinates is denoted by $\mathbf{v} = [v_1, v_2, ..., v_{nv}]^T$.

To define the desired functionality of a mechanism, some measure of output, that is controlled by mechanism inputs, must be defined. *Output coordinates* constitute a subset of mechanism generalized coordinates that define the useful functionality of the mechanism. Output coordinates are distinct from input coordinates and are denoted by $\mathbf{u} = [u_1, u_2, ..., u_{nu}]^T$. Generalized coordinates that are neither input coordinates, nor output coordinates, are called *intermediate coordinates* denoted by $\mathbf{w} = [w_1, w_2, ..., w_{nw}]^T$, where $nw = nq - nq - nq$.

Inequality constraints are usually imposed on the input variables and often also apply to the intermediate variables. They take the form

$$\mathbf{v}^{min} \leq \mathbf{v} \leq \mathbf{v}^{max} \tag{2.2}$$

and

$$\mathbf{w}^{min} \leq \mathbf{w} \leq \mathbf{w}^{max} \tag{2.3}$$

The *accessible output set* of a manipulator is the collection of all achievable output coordinates of the manipulator. To be more precise in characterizing the accessible output set for a manipulator, the generalized coordinates are partitioned as follows:

$$\mathbf{q} = [\mathbf{u}^T, \quad \mathbf{v}^T, \quad \mathbf{w}^T]^T \tag{2.4}$$

In terms of this partition the constraint equations (2.1) may be written as:

$$\Phi(\mathbf{u},\mathbf{v},\mathbf{w}) = \mathbf{0} \tag{2.5}$$

The accessible output set A is therefore simply defined as:

$$A \equiv \{\, \mathbf{u} \in R^{nu} : \Phi(\mathbf{u},\mathbf{v},\mathbf{w}) = \mathbf{0}\,;\ \mathbf{v} \text{ satisfying (2.2) and } \mathbf{w} \text{ satisfying (2.3)} \,\} \tag{2.6}$$

Intuitively the *boundary* ∂A of the accessible output set may be defined as:

$$\partial A \equiv \{\, \mathbf{u} \in R^{nu} : \mathbf{u} \in A \ \text{ and } \exists \text{ a } \mathbf{s} \in R^{nu} \text{ such that for } \mathbf{u}' = \mathbf{u} + \lambda\mathbf{s},\ \lambda \in R$$
$$\text{arbitrary small and either positive or negative, no } \mathbf{v} \text{ and } \mathbf{w} \text{ exist that satisfy} \tag{2.7}$$
$$\Phi(\mathbf{u}', \mathbf{v}, \mathbf{w}) = \mathbf{0} \text{ as well as inequalities (2.2) and (2.3)} \,\}$$

2.3 FINDING A POINT ON ∂A

A distinction is made with respect to system of equations (2.1) and (2.5), between two possibilities:

Case (i): where $m = nv$ and, given **u** and **w**, system (2.5) may easily be solved to give **v** in terms of **u** and **w**:

$$\mathbf{v} = \mathbf{v}(\mathbf{u},\mathbf{w}) \tag{2.8}$$

This is typically the situation with parallel manipulators where the inverse kinematics is easy to solve.

Case (ii): where $m = nu$ and, given **v** and **w**, system (2.5) may easily be solved to give **u** in terms of **v** and **w**:

$$\mathbf{u} = \mathbf{u}(\mathbf{v},\mathbf{w}) \tag{2.9}$$

This again is typical for serially linked manipulators where the forward kinematics is relatively easy to solve.

First consider first *Case (i)*. Assume that a radiating point $\mathbf{u}^0$ of A is available, and for the moment assume that it is interior to the accessible set. It is now proposed that, consistent with the definition of ∂A in (2.7), a point $\mathbf{u}^b$ on the boundary in the direction $\mathbf{s} \in R^{nu}$ from $\mathbf{u}^0$ be determined by solving the following constrained optimization problem:

Problem (i):

$$\underset{\mathbf{u},\mathbf{w}}{\textit{maximize}} \quad \left\|\mathbf{u}-\mathbf{u}^0\right\|$$

$$\textit{such that:} \quad \begin{aligned} \mathbf{v}^{\min} &\le \mathbf{v}(\mathbf{u},\mathbf{w}) \le \mathbf{v}^{\max} \\ \mathbf{w}^{\min} &\le \mathbf{w} \le \mathbf{w}^{\max} \end{aligned}$$

$$\textit{and subject to equality constraints:} \quad \mathbf{h}(\mathbf{u},\mathbf{s})=\mathbf{0},\ \mathbf{h}\in \mathrm{R}^{nu-1}$$

which defines a point on the parameterized straight line ray, $\mathbf{u}(\lambda)=\mathbf{u}^0+\lambda\mathbf{s},\ \lambda\in\mathrm{R}$. Here $\|\cdot\|$ denotes the Euclidean norm. {For example, if $nu=2$, $\mathbf{u}=[x,y]^{\mathrm{T}}$, $\mathbf{u}^0=[x^0,y^0]^{\mathrm{T}}$, and $\mathbf{s}=[\mathrm{s}_x,\mathrm{s}_y]^{\mathrm{T}}$, then $\mathbf{u}=\mathbf{u}^0+\lambda\mathbf{s}$ has the components $x=x^0+\lambda\mathrm{s}_x$; $y=y^0+\lambda\mathrm{s}_y$ and it follows that: $\mathrm{h}(\mathbf{u},\mathbf{s})=(x-x^0)/\mathrm{s}_x-(y-y^0)/\mathrm{s}_y=0$ } (see Figure 2.1)

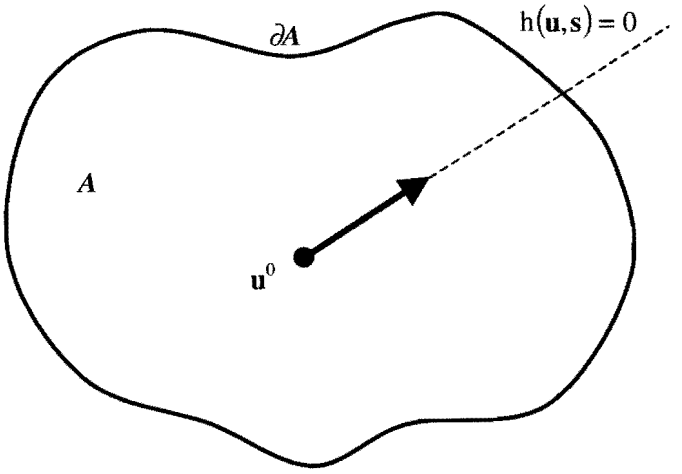

Figure 2.1 Ray in A from $\mathbf{u}^0$ to ∂A.

For *Case (ii)* the associated constrained optimization problem is given by:

Problem (ii):

$$\underset{\mathbf{v},\mathbf{w}}{\textit{maximize}} \quad \left\|\mathbf{u}(\mathbf{v},\mathbf{w})-\mathbf{u}^0\right\|$$

$$\textit{such that:} \quad \begin{aligned} \mathbf{v}^{\min} &\le \mathbf{v} \le \mathbf{v}^{\max} \\ \mathbf{w}^{\min} &\le \mathbf{w} \le \mathbf{w}^{\max} \end{aligned}$$

$$\textit{and subject to equality constraints:} \quad \mathbf{h}(\mathbf{u}(\mathbf{v},\mathbf{w}),\mathbf{s})=\mathbf{0}$$

where the equality constraint defines a point $\mathbf{u}$ on the straight line through $\mathbf{u}^0$ in the direction $\mathbf{s}$.

Note that should $\mathbf{u}^0$ be chosen to be exterior to A, then the optimization problems above obviously become *minimization* problems.

In this chapter, the presentation will be restricted to planar mechanisms. In Chapter 3 the methodology developed here for and applied to planar mechanisms, will be extended to spatial mechanisms.

2.4 BASIC METHODOLOGY FOR MAPPING THE BOUNDARY OF A PLANAR ACCESSIBLE SET

Assume a planar manipulator with a two-dimensional accessible set $\boldsymbol{A}$, and also for the moment assume that $\boldsymbol{A}$ is convex, which certainly will not always be the case. Also assume, for the moment, that the radiating point $\mathbf{u}^0$ is an interior point as shown in Figure 2.2.

The boundary $\partial \boldsymbol{A}$ may now be numerically mapped by solving the appropriate optimization problem ((i) or (ii)) for N successive rays, with respective directions $\mathbf{s}^i, i = 0,1,2,...,N$, emanating at angular intervals of δ (where for example $\delta = 360^\circ/N$) from $\mathbf{u}^0 = [x^0, y^0]^T$ as depicted in Figure 2.2.

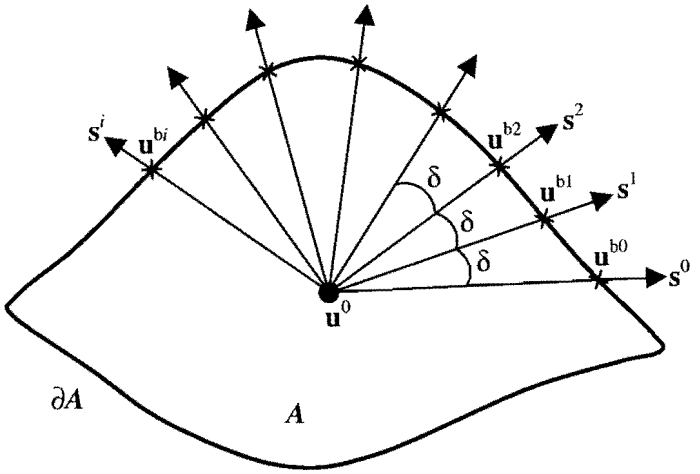

Figure 2.2 Numerical map of $\partial \boldsymbol{A}$; $\mathbf{u}^{bi}$, $i = 0,1,...,N$.

Questions now arise in connection with details of the implementation of the methodology. The first question relates to how an *initial* radiating point $\mathbf{u}^0$ may be obtained. Depending on the particular geometry of each case, a suitable choice for $\mathbf{u}^0$ may be self-evident. If not, it is suggested that, in *Case (i)*, $\mathbf{u}^0$ may be obtained from equation (2.8) by solving for $\mathbf{u}$ in:

$$\overline{\mathbf{v}} = \mathbf{v}(\mathbf{u}, \overline{\mathbf{w}}) \qquad (2.10)$$

where

$$\overline{\mathbf{v}} = \left(\mathbf{v}^{\min} + \mathbf{v}^{\max}\right)/2$$
$$\overline{\mathbf{w}} = \left(\mathbf{w}^{\min} + \mathbf{w}^{\max}\right)/2$$

In practice this may be done by solving the least squares optimization problem

$$\underset{\mathbf{u}}{minimize} \ \left\|\mathbf{v}(\mathbf{u}, \overline{\mathbf{w}}) - \overline{\mathbf{v}}\right\|^2 \qquad (2.11)$$

In *Case (ii)*, if an obvious choice for $\mathbf{u}^0$ is not available, then an indication may be obtained from equation (2.9):

$$\mathbf{u}^0 = \mathbf{u}(\overline{\mathbf{v}}, \overline{\mathbf{w}}) \tag{2.12}$$

The second question concerns the strategy to be adopted if non-convexity of $\boldsymbol{A}$ interferes with the mapping as illustrated in Figure 2.3, where as result of the non-convexity, two boundary points $\mathbf{u}_1^b$ and $\mathbf{u}_2^b$ exist.

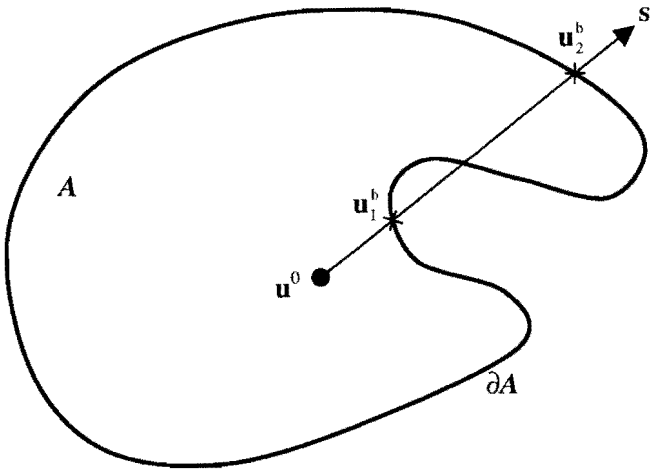

Figure 2.3 Complication if $\boldsymbol{A}$ is non-convex.

If this happens, it will be necessary to adjust $\mathbf{u}^0$ such that the boundary point $\mathbf{u}^b$ is unique for a prescribed search direction $\mathbf{s}$. The precise strategy to be adopted will be described separately in the later sections dealing with the application of the methodology. A final question that must be addressed, is what procedure to adopt if the boundary mapping approaches a bifurcation point. The procedure to deal with such an eventuality is also described in the sections dealing with the applications.

2.5 APPLICATION TO THE PLANAR SERIAL MANIPULATOR

Although the emphasis of this study is on determining the workspaces of parallel manipulators, the versatility of the optimization method should at least correspond to that of Haug et al's [12] continuation method. Consequently, the serial manipulator studied by Haug et al. [12] is also investigated in this section using the optimization approach.

2.5.1 Geometry of the Planar Serial Manipulator

The redundantly controlled serial manipulator shown in Figure 2.4 was therefore purposefully taken from Haug et al. [12]. This is a planar manipulator with three links, and three revolute joints.

Revolute joint 1 is the connection between the serial manipulator and the ground. The global coordinate system is fixed with the origin coinciding with joint 1. The orientation angle of link 1 relative to the

positive X-axis, is indicated by θ_1, and is measured in a right hand sense about the origin of the fixed global coordinate system. Similarly θ_2 and θ_3 measures the orientation angles of respectively link 2 with link 1, and link 3 with link 2. Depending on the configuration of the serial manipulator, the orientation angles can be positive, or negative.

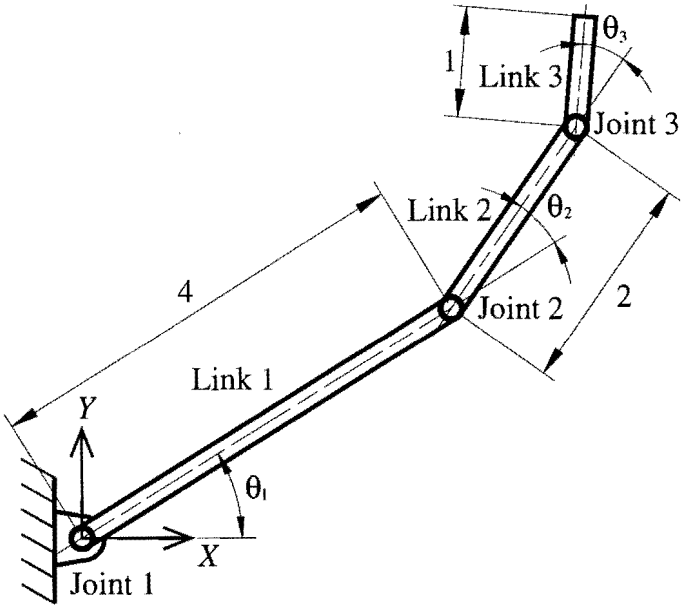

Figure 2.4 Planar serial manipulator with redundant input.

The working point P is the end point of link 3, which is the position where in practice some end effector is mounted. The accessible region of the working point depends on the upper and lower orientation angle limitations. In accordance to Haug et al. [12], the same limitations are imposed on all three orientation angles. Expressing the constraint equations in terms of the orientation angles in radians, gives:

$$-\frac{\pi}{3} = \theta_i^{\min} \le \theta_i \le \theta_i^{\max} = \frac{\pi}{3} \tag{2.13}$$

This choice of angle limits clearly causes the workspace to be symmetric about the positive X-axis, and one also intuitively expects the workspace to be non-convex.

2.5.2 Constraint Equations of the Planar Serial Manipulator

With reference to Section 2.2 , equation (2.13) is the serial manipulator version of the general inequality constraints (2.2). Here the orientation angles are obviously the *input variables*, i.e. $\mathbf{v} = [\theta_1, \theta_2, \theta_3]^T$, and the global coordinates of the working point P are the *output coordinates*, i.e. $\mathbf{u} = [x, y]^T$. There are no *intermediate coordinates* required in describing the serial manipulator.

The serial manipulator therefore has five generalized coordinates (2.4):

$$\mathbf{q} = \left[\mathbf{u}^T, \mathbf{v}^T\right]^T = \left[x, y, \theta_1, \theta_2, \theta_3\right]^T$$

Having only two degrees of freedom, and three inputs, makes the serial manipulator redundantly controlled. This means that the same output coordinates can be obtained with different sets of input coordinates. The situation becomes clearer when looking at the two kinematic constraint equations corresponding to general form (2.5). Doing the forward kinematic analysis for the serial manipulator, gives expressions for the output coordinates in terms of the input angles ($\theta_i, i = 1, 2, 3$):

$$\begin{aligned} x &= 4\cos\theta_1 + 2\cos(\theta_1 + \theta_2) + \cos(\theta_1 + \theta_2 + \theta_3) \\ y &= 4\sin\theta_1 + 2\sin(\theta_1 + \theta_2) + \sin(\theta_1 + \theta_2 + \theta_3) \end{aligned} \tag{2.14}$$

Having two equations in three variables results in the existence of multiple solutions for a particular choice of (x, y).

Rewriting equation (2.14) in the general form (2.5), gives:

$$\mathbf{\Phi}(\mathbf{u}, \mathbf{v}) = \begin{bmatrix} u_1 - 4\cos(v_1) - 2\cos(v_1 + v_2) - \cos(v_1 + v_2 + v_3) \\ u_2 - 4\sin(v_1) - 2\sin(v_1 + v_2) - \sin(v_1 + v_2 + v_3) \end{bmatrix} = \mathbf{0} \tag{2.15}$$

from which explicit expressions for $\mathbf{u}$ follows:

$$\mathbf{u}(\mathbf{v}) = \begin{bmatrix} 4\cos(v_1) + 2\cos(v_1 + v_2) + \cos(v_1 + v_2 + v_3) \\ 4\sin(v_1) + 2\sin(v_1 + v_2) + \sin(v_1 + v_2 + v_3) \end{bmatrix} \tag{2.16}$$

The inequality constraints given by expression (2.13) can be written in the standard form (2.2):

$$\begin{gathered} \mathbf{v}^{min} \le \mathbf{v} \le \mathbf{v}^{max} \\ \text{where } \mathbf{v}^{min} = \left[\theta_1^{min}, \theta_2^{min}, \theta_3^{min}\right]^T \text{ and } \mathbf{v}^{max} = \left[\theta_1^{max}, \theta_2^{max}, \theta_3^{max}\right]^T \end{gathered} \tag{2.17}$$

Notice that the serial manipulator can be classified under *Case (ii)* of Section 2.3. Expressions (2.17), (2.16) and (2.15) which were specifically derived for the serial manipulator, correspond to the general expressions (2.2), (2.9) and (2.5). The boundary ∂A of the accessible set of the serial manipulator may therefore be numerically determined by applying the basic methodology described in Section 2.4 and in which optimization *Problem (ii)* of Section 2.3 is successively solved.

The specific constrained optimization method used in solving the optimization problems is the dynamic trajectory method of Snyman [37], [38] for unconstrained optimization, applied to penalty function formulations (Snyman et al. [39], Snyman [40]) of the constrained problems. The particular computer code used is *LFOPCV3* (Snyman [40]).

2.5.3 Discussion of Results for the Planar Serial Manipulator

2.5.3.1 Outer Accessible Workspace Boundary

Figure 2.5 shows the outer accessible workspace boundary obtained.

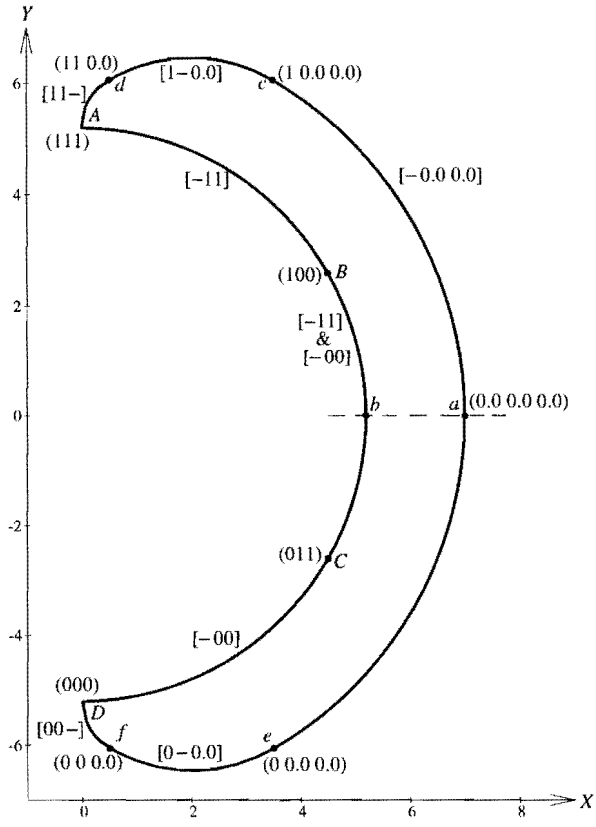

Figure 2.5 Boundary of the accessible output set of the planar serial manipulator.

With the workspace being symmetrical about the positive X-axis, only the top half is computed. The radiating point for determining the workspace is chosen to be at the origin of the global coordinate system, i.e. $\mathbf{u}^0 = [0, 0]^T$. This choice for the radiating point allows for the separation of the outer workspace boundary into a far and a near boundary.

Looking at only the top half of the accessible output set, it is clear that the near and far boundaries are smooth curves, which meet at an *extreme point A*. The working point of the serial manipulator will be at this extreme point A, if the input angles take on their respective maximum values, i.e. $\mathbf{v}_i = \mathbf{v}_i^{\max}$ for $i = 1, 2, 3$. The output coordinates of point A are determined by substituting these maximum values of $\mathbf{v}_i$ in equation (2.16), resulting in $\mathbf{u}^A = [0.0,\ 5.1962]^T$.

For the top half, the outer boundary is mapped by successively solving optimization *Problem (ii)* for successive rays emanating from the radiating point $\mathbf{u}_0$ which, for the far boundary, is effectively an

interior point. The *maximization* is carried out for successive search directions $\mathbf{s}_i, i = 1, 2, ..., N$, each corresponding to a radiating angle ψ_i. Here $\psi_1 = 0$ and $\psi_N = \pi/2$, with the other angles suitably and monotonically spaced in between. Clearly $\psi_N = \pi/2$ corresponds to the ray passing through $\mathbf{u}^A$.

As soon as the point *A* is reached, *Problem (ii)* becomes a *minimization* problem since, for the mapping of the near boundary, $\mathbf{u}^0$ is now an exterior point. The inner boundary is now mapped by successively carrying out the minimization, but now for successive angles decreasing from $\psi_{1'} = \pi/2$ and $\psi_{N'} = 0$. The bottom half of the workspace boundary is simply a mirror image of the top half.

In the mapping, depending on the curvature of the workspace boundary, provision is made for adjusting the angular interval between rays so as to ensure sufficient accuracy.

Haug et al. [12] not only manage to determine the accessible workspace boundaries of the serial manipulator, they also describe the behavior of the manipulator associated with different curves of the workspace. Their method enables them to find the bifurcation points located within, and on the boundaries of the accessible output set. These bifurcation points are numbered, and each curve connecting two bifurcation points is "described" with reference to those input variables that remain fixed, and those input variables that vary as the manipulator advances along the specific curve.

Here, an alternative and more concise notation for labeling the bifurcation points and boundary curves is proposed. This should facilitate the discussion of the results.

The serial manipulator working point *P* will coincide with a bifurcation point if all the input angles are fixed at (usually) either their maximum or minimum allowable values. If for each input angle ($\theta_i, i = 1, 2, 3$), the state is indicated by setting $X_i := 0$ for the minimum allowable value and $X_i := 1$ for the maximum allowable value, then the configuration of the manipulator at a specific bifurcation point may be indicated and labeled by a triplet enclosed in round brackets, $(X_1\ X_2\ X_3)$. Thus point *A* in Figure 2.5 where all three input angles have maximum values is, for example, labeled by $(1\ 1\ 1)$.

The boundary curves may be labeled in a similar manner. Usually, as one moves from one bifurcation point to the next along a particular boundary curve, the value of one of the input angles, say *j*, varies from one extreme bound to the other. This may be indicated by setting $X_j := -$ and $X_i := 0$ or 1 for $i \neq j$, depending on whether input angle *i* assumes a minimum or maximum value. The curve may therefore be labeled by a triplet enclosed in square brackets, $[X_1\ X_2\ X_3]$.

On closer inspection of the results for the far boundary *aA* in Figure 2.5, three distinct curves are identified. Along curve *ac* the serial manipulator is stretched and the three links form a straight line. The working point will advance along this curve as it moves on an arc of radius $= 4+2+1=7$, with center of radius at the origin of the global coordinate system.

The proposed notation for labeling the boundary curves and bifurcation points is slightly modified to accommodate curves and points where the input variables take on fixed values other than the extreme values corresponding to bounds.

Curve ce is labeled [– 0.0 0.0] indicating that input variable v_1 varies between its minimum and maximum values, while input variables v_2 and v_3 both remain fixed at 0.0. The top half of curve *ce* [– 0.0 0.0] is curve *ac*, where input variable v_1 varies between zero and its maximum value. Point *c* is labeled as (1 0.0 0.0) indicating that $\mathbf{v}^c = [v_1^{max}, 0.0, 0.0]^T$ while point *a* is labeled (0.0 0.0 0.0) indicating that $\mathbf{v}^a = [0.0, 0.0, 0.0]^T$. The global coordinates of point *c* are $\mathbf{u}^c = [3.5,\ 6.0622]^T$. The bottom half of curve *ce* [– 0.0 0.0] is curve *ae* where input variable v_1 varies between zero and its minimum value, while v_2 and v_3 remain fixed at 0.0. Point *e* is labeled (0 0.0 0.0) indicating that $\mathbf{v}^e = [v_1^{min}, 0.0, 0.0]^T$, and the global coordinates of point *e* are $\mathbf{u}^e = [3.5,\ -6.0622]^T$

With v_1 fixed at $v_1^{max} = \pi/3$, the working point will map the curve *cd* [1 – 0.0] as it moves on an arc of radius $= 2+1=3$ with the center of radius coinciding with the position of revolute joint 2. The mirror image of curve *cd* [1 – 0.0] is curve *ef* [0 – 0.0], where v_1 is fixed at $v_1^{min} = -\pi/3$. Finally with input variables v_1 and v_2 both fixed at their maximum values, curve *dA* [1 1 –] lies on an arc of radius $= 1$, with center of radius situated at revolute joint 3. It follows that the mirror image of curve *dA* [1 1 –] is curve *fD* [0 0 –], where input variables v_1 and v_2 both fixed at their minimum values.

The inner boundary of the workspace is an arc of radius $= 5.1962$ which joins bifurcation points *A* and *D*. The arc radius is the shortest possible distance from the global coordinate system origin to the working point, and can be obtained with both input variables v_2 and v_3 either at their maximum, or minimum values. Curve *AD* in fact consist of two overlapping bifurcation curves *AC* [– 1 1], and *BD* [– 0 0]. The global coordinates of any bifurcation point can easily be determined from equation (2.16).

Clearly in this specific case, the near boundary could have been obtained by a simple and obvious geometrical construction, rather than by the general optimization mapping used here.

2.5.3.2 Curves Connecting Bifurcation Points

For the serial manipulator under consideration, four bifurcation points are situated inside the workspace boundaries, namely points *E*, *F*, *G* and *H* as shown in Figure 2.6.

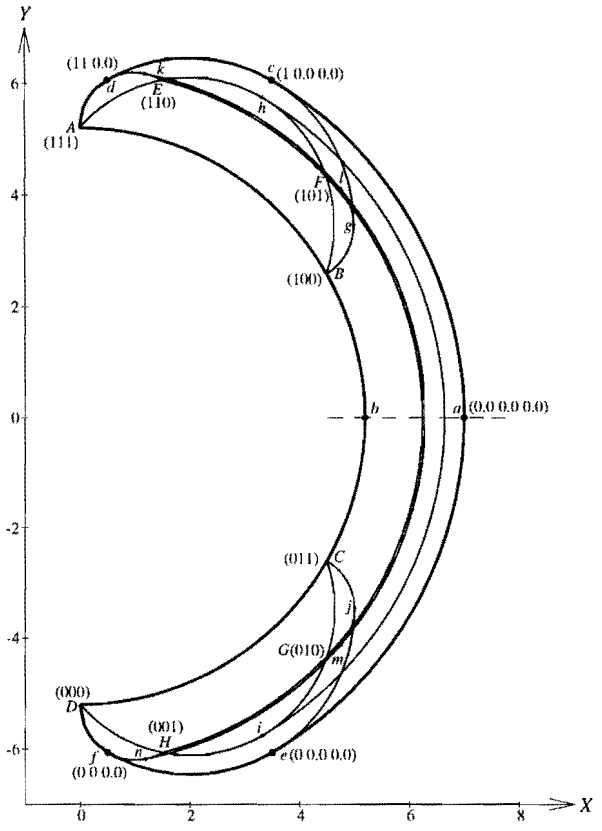

Figure 2.6 Interior bifurcation points and curves of the planar serial manipulator.

Figure 2.6 also shows interior curves connecting these bifurcation points. For clarity, a magnified view of the upper segments is shown in Figure 2.7. The interior curves connecting the bifurcation points, are mapped using forward kinematic analyses. Taking curve AdE $[1\ 1\ -]$ as an example: M points along curve AdE $[1\ 1\ -]$ can easily be mapped by setting $v_1 = v_1^{max}$, $v_2 = v_2^{max}$ and $v_3 = v_3^j$, where

$$v_3^j = v_3^{max} - \frac{j}{M}\left(v_3^{max} - v_3^{min}\right)$$

and solving for each setting j, $j = 0, 1, 2, \ldots, M$ equation (2.16) directly to give the corresponding output coordinates $\mathbf{u}(\mathbf{v})$.

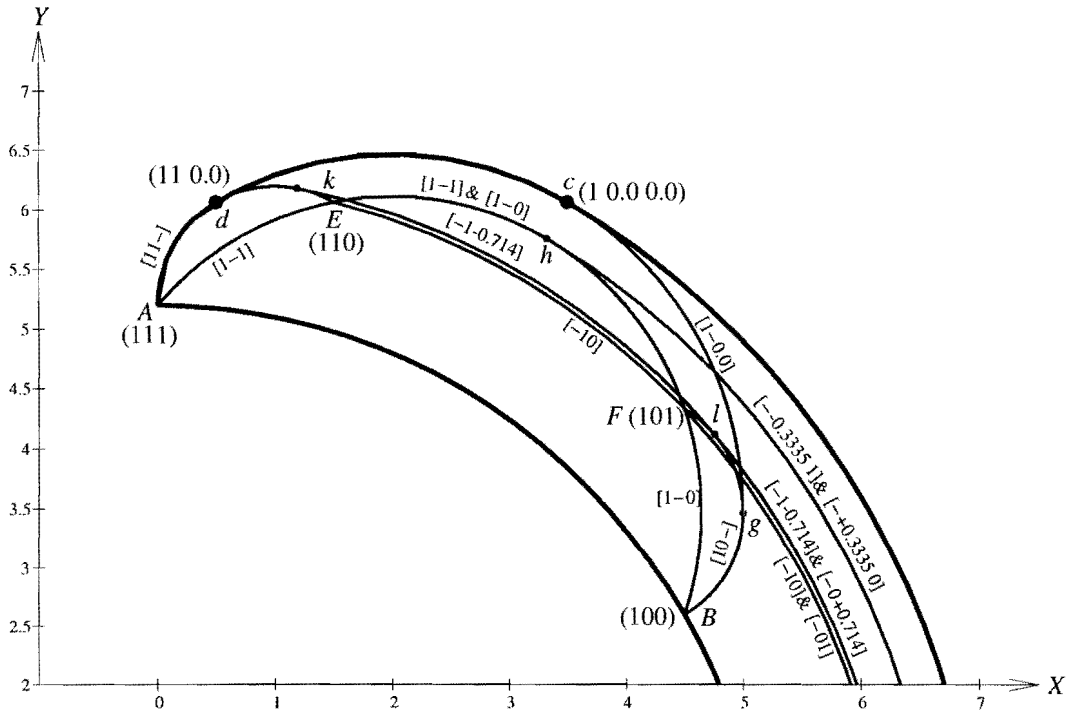

Figure 2.7 Magnified view of upper part of boundary and bifurcation curves of planar serial manipulator.

Curve *cg* $[1\ -\ 0.0]$ does not connect any bifurcation points, but is the interior extension of the second arc *de* on the far boundary described in Section 2.5.3.1. The mapping of this curve is done in a similar manner to that described for curve *AE* above. Curve *ej* $[0\ -\ 0.0]$ is the mirror image of curve *cg* $[1\ -\ 0.0]$.

The final two interior paths to be dealt with, are path *hi* and path *klmn* also reported by Haug et al. [12]. Path *hi* lies on an arc with radius $= 6.64575$, and center point at $(0.0,\ 0.0)$. The radius is obtained by solving optimization *Problem (ii)* with $-\pi/3 = v_i^{min} \le v_i \le v_i^{max} = \pi/3$ for $i = 1$ and 2, and $v_3 = v_3^{max} = \pi/3$.

Here it was noticed that with variation in the search direction, v_1 varies, but v_2 remains constant at the value $v_2 = -0.3335$. If v_3 is fixed at $v_3 = v_3^{max} = \pi/3$, then carrying out the optimization for different search directions, v_1 varies again but v_2 takes on the constant value $v_2 = +0.3335$. The respective computed curves *hi* $[-\ -0.3335\ \ 1]$ and *ih* $[-\ +0.3335\ \ 1]$ coincide as shown.

Path *klmn* is computed similarly and lies on an arc of radius 6.2915. This curve consists of two partially overlapping curves *km* $[-\ \ 1\ \ -0.714]$, and *ln* $[-\ \ 1\ \ +0.714]$ as shown in Figure 2.6.

It should be stated that the respective constant values (0.3335 and 0.714) assumed by v_2 for the curves *ih* and *ln* differ slightly from that (0.3241 and 0.7499) reported by Haug et al. [12].

2.6 APPLICATION TO THE PLANAR STEWART PLATFORM

In the remaining part of this study, the emphasis falls on Stewart platform workspaces, and specifically how the optimization approach is utilized in analyzing and characterizing the different workspaces. This section deals with determining the exterior boundaries of the accessible workspace of a planar Stewart platform, as well as finding the bifurcation point connecting curves.

2.6.1 Geometry of the Planar Stewart Platform

The geometry of the planar Stewart platform considered here is taken from Haug et al. [12], and is as shown in Figure 2.8.

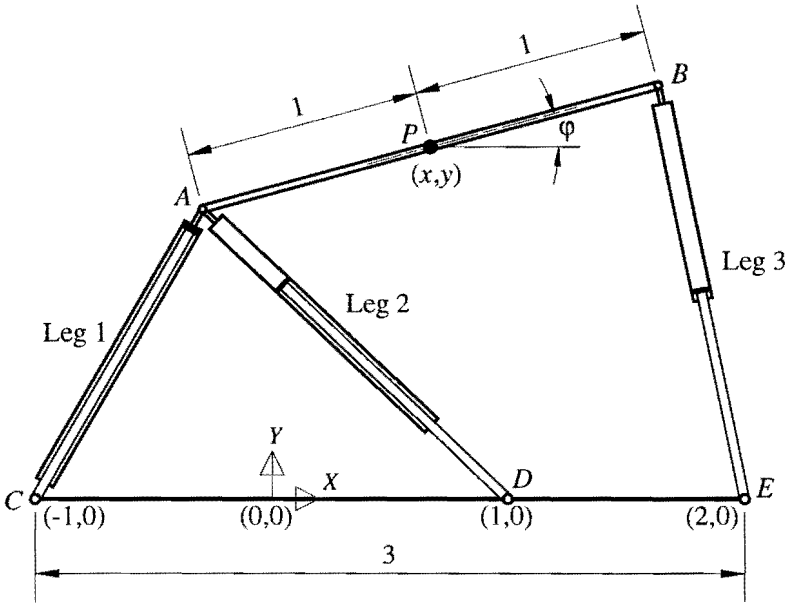

Figure 2.8 Planar Stewart platform.

The moving upper platform is connected to the fixed base via three linear actuators such as, for example, hydraulic cylinders. The base can in general be fixed in any orientation but in this case it is fixed horizontally. The global coordinate system was chosen to be on the base, with the origin midway between joints *C* and *D*, and with the directions of the axes as shown in Figure 2.8.

The lower ends of the actuator legs are connected to the base at points *C*, *D* and *E* with respective global coordinates $(-1,0)$, $(1,0)$ and $(2,0)$. The upper ends of actuator legs 1 and 2 are both connected to the left hand side of the top platform at point *A*. Actuator leg 3 has its upper end connected to the right side

of the top platform at B. The working point P is at the center of the top platform at global position (x, y) with the platform making an angle φ with the horizontal.

Each of the three actuator legs is a variable length linear actuator with its length indicated by l_i, $i = 1, 2, 3$. There are limitations on the maximum and minimum lengths of linear actuators, and therefore the accessible region of the working point P is determined by the constraints on the actuator lengths which are formally expressed as:

$$0 < l_i^{\min} \leq l_i < l_i^{\max} \tag{2.18}$$

for $i = 1, 2, 3$

The actual leg length limits that are used, are the same as the limits specified by Haug et al. [12], and are given in Table 2.1.

Leg i	$l_i^{\min}$	$l_i^{\max}$
1	$\sqrt{2}$	2
2	$\sqrt{2}$	2
3	1	$\sqrt{3}$

Table 2.1 Minimum- and maximum lengths of the actuator legs.

2.6.2 Constraint Equations of the Planar Stewart Platform

Clearly for the planar Stewart platform, and with reference to the definitions given in Section 2.2, the actuator leg lengths are the *input variables*, i.e. $\mathbf{v} = [l_1, l_2, l_3]^T$, on which the inequality constraints (2.18) are imposed corresponding to the general constraints (2.2). The global coordinates of the working point are the *output variables*, i.e. $\mathbf{u} = [x, y]^T$. The rotation angle φ of the top platform is the one and only *intermediate coordinate*, i.e. $\mathrm{w} = \varphi$. Here, no inequality constraints of the general form (2.3), are imposed on the intermediate variable w.

The generalized coordinates (2.4) for the Stewart platform are given by

$$\begin{aligned} \mathbf{q} &= \begin{bmatrix} \mathbf{u}^T & \mathbf{v}^T & \mathbf{w}^T \end{bmatrix}^T \\ &= \begin{bmatrix} \mathbf{u}^T & \mathbf{v}^T & \mathrm{w} \end{bmatrix}^T \\ &= [x,\ y,\ l_1,\ l_2,\ l_3,\ \varphi]^T \end{aligned} \tag{2.19}$$

This system clearly has three degrees of freedom, since the configuration of the system is uniquely defined by any three of these coordinates. This implies the existence of three kinematic constraint equations of the form (2.5), specifying the interrelationships between the coordinates.

From the geometry shown in Figure 2.8, the inverse kinematics may easily be performed to give the actuator lengths in terms of x, y and φ:

$$\begin{aligned} l_1^2 &= (x - \cos\varphi + 1)^2 + (y - \sin\varphi)^2 \\ l_2^2 &= (1 - x + \cos\varphi)^2 + (y - \sin\varphi)^2 \\ l_3^2 &= (x + \cos\varphi - 2)^2 + (y - \sin\varphi)^2 \end{aligned} \tag{2.20}$$

The above may be rewritten in the standard form (2.5) for the constraint equations as:

$$\mathbf{\Phi}(\mathbf{u},\ \mathbf{v},\ \mathrm{w}) = \begin{bmatrix} \mathrm{v}_1^2 - (\mathrm{u}_1 - \cos(\mathrm{w}) + 1)^2 - (\mathrm{u}_2 - \sin(\mathrm{w}))^2 \\ \mathrm{v}_2^2 - (1 - \mathrm{u}_1 + \cos(\mathrm{w}))^2 - (\mathrm{u}_2 - \sin(\mathrm{w}))^2 \\ \mathrm{v}_3^2 - (\mathrm{u}_1 + \cos(\mathrm{w}) - 2)^2 - (\mathrm{u}_2 - \sin(\mathrm{w}))^2 \end{bmatrix} = \mathbf{0} \tag{2.21}$$

from which the explicit expressions for $\mathbf{v}$ follow:

$$\mathbf{v} = \mathbf{v}(\mathbf{u}, \mathrm{w}) = \begin{bmatrix} \sqrt{(\mathrm{u}_1 - \cos(\mathrm{w}) + 1)^2 + (\mathrm{u}_2 - \sin(\mathrm{w}))^2} \\ \sqrt{(1 - \mathrm{u}_1 + \cos(\mathrm{w}))^2 + (\mathrm{u}_2 - \sin(\mathrm{w}))^2} \\ \sqrt{(\mathrm{u}_1 + \cos(\mathrm{w}) - 2)^2 + (\mathrm{u}_2 - \sin(\mathrm{w}))^2} \end{bmatrix} \tag{2.22}$$

Inequalities (2.18) may also be written in the standard form:

$$\begin{gathered} \mathbf{v}^{\min} \le \mathbf{v} \le \mathbf{v}^{\max} \\ \text{where } \mathbf{v}^{\min} = \left[l_1^{\min}, l_2^{\min}, l_3^{\min}\right]^{\mathrm{T}} \text{ and } \mathbf{v}^{\max} = \left[l_1^{\max}, l_2^{\max}, l_3^{\max}\right]^{\mathrm{T}} \\ \text{and } \mathbf{v} = \mathbf{v}(\mathbf{u}, \mathrm{w}) \text{ as given by (2.22)} \end{gathered} \tag{2.23}$$

Now expressions (2.23), (2.21) and (2.22) for the planar Stewart platform, clearly correspond to *Case (i)* of Section 2.3 , specified in general by expressions (2.2), (2.5) and (2.8).

The method used to determine the boundary ∂A of the accessible output set for the planar Stewart platform is similar to the method used for the serial manipulator. The only difference is that for the planar Stewart platform optimization *Problem (i)* is successively solved. The computer code *LFOPCV3* [40] is again used to solve the optimization problems.

Note that here there is no explicit restriction (2.3) on w. This implies that there are no limitations on the orientation angle of the top platform, therefore the workspace boundary is solely dependant on the limitations imposed on the actuator leg lengths. This is called the *accessible* or *reachable workspace* defined by Kumar [11] as the "volume or space within which a reference point on the hand or end effector of a manipulator can be made to coincide with any point in the volume or space".

2.6.3 Discussion of Accessible Workspace Results for the Planar Stewart Platform

2.6.3.1 Outer Accessible Workspace Boundary

The computed outer boundaries of the accessible workspaces for two different situations are shown in Figure 2.9 and Figure 2.10. For the cases depicted here, the *boundary mapping* was done at intervals of $\delta = 5^\circ$ (see Figure 2.2).

Figure 2.9 shows the boundary of the accessible output set of the *standard* planar Stewart platform for which the limits on the actuator lengths, given in Table 2.1, are such as to prevent a singular configuration from occurring. Such a singularity will occur if the upper platform is allowed to take on a position that is collinear with any of the actuators (Haug et al. [41]).

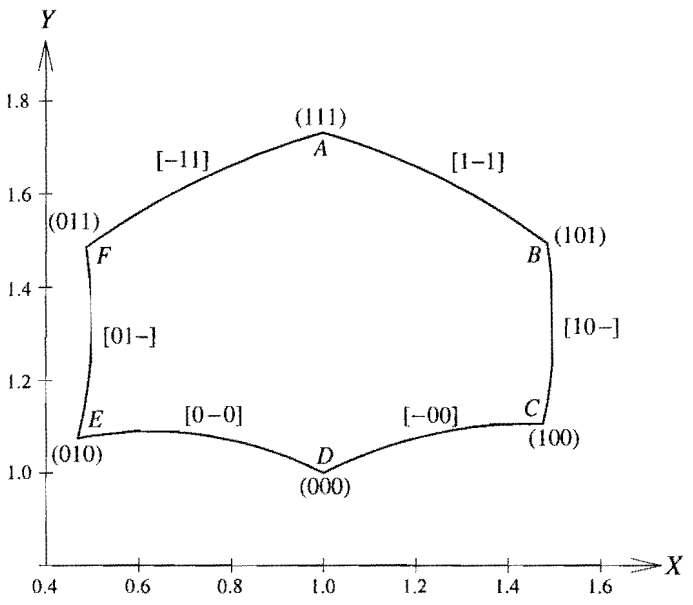

Figure 2.9 Boundary of the accessible output set of the *standard* planar Stewart platform $(1 \le l_3 \le \sqrt{3})$.

The methodology described in Section 2.4, represented by the least squares problem (2.11), is used to find the central radiating point for the planar Stewart platform. The central point for the *standard* planar Stewart platform is $\mathbf{u}^0 = [0.99996 \quad 1.374791]^T$.

Figure 2.10 shows the results for the *modified* planar Stewart platform, where the limitations on actuator leg 3 is relaxed to $1 \le l_3 \le 3$. This was also done by Haug et al. [12] to allow for collinearity to occur. The central radiating point for this second situation is $\mathbf{u}^0 = [0.95169 \quad 1.69061]^T$.

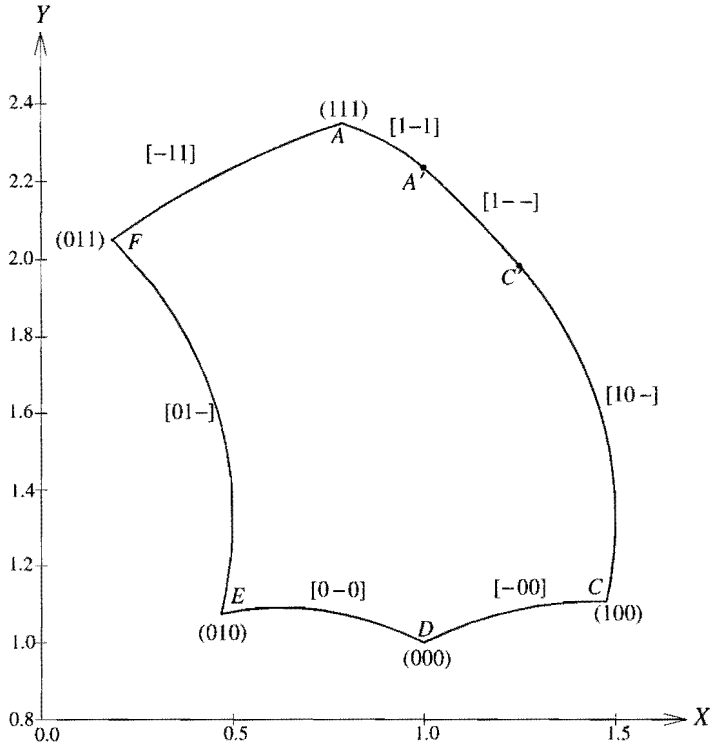

Figure 2.10 Boundary of the accessible output set of the *modified* planar Stewart platform ($1 \le l_3 \le 3$).

One notices that the boundary of the workspace for the standard case is defined by six smooth curves intersecting at distinct corners *A*, *B*, *C*, *D*, *E* and *F*. On closer inspection of the results, it becomes clear that one may easily relate the various curves of the workspace boundary to the behavior of the Stewart platform. This was indeed done by Haug et al. [12] in identifying the corners as bifurcation points and numbering them. The individual boundary curves were then labeled according to the numbers of the bifurcation points they connected and the variation of the actuator lengths were tabulated for each curve.

With reference to Section 2.5.3.1 the newly proposed notations for labeling the bifurcation points and boundary curves are also applied here to describe the workspace of the planar Stewart platform. Labeling the bifurcation points in the proposed manner indicates which actuator legs are at their minimum values, and which assume their maximum lengths when the manipulator working point coincides with any specific bifurcation point. Thus point *A* in Figure 2.9 and Figure 2.10, where all three legs have maximum values is, labeled by $(1\ 1\ 1)$. The other boundary bifurcation points of the standard planar Stewart platform are similarly labeled as shown in Figure 2.9.

Similarly, the square bracket triplets with which the boundary curves are labeled, indicate which legs remain fixed at either their minimum or maximum bounds, and which legs vary from one extreme to the other as the manipulator working point moves from one extreme to the other. Consider, as an example, boundary curve AB connecting bifurcation point A $(1\ 1\ 1)$ to bifurcation point B $(1\ 0\ 1)$ in Figure 2.9. This curve is labeled by $[1\ -\ 1]$, indicating that legs 1 and 3 remain fixed at their respective maximum lengths, and leg 2 varies from its maximum length (working point coinciding with A) to its minimum length (working point coinciding with B). The other boundary curves are labeled in a similar manner.

The precise mapping of the bifurcation point corners is done by, having identified through the boundary mapping procedure the three active constraints at the corner, then minimizing $\left\|\mathbf{v}(\mathbf{u}, w) - \mathbf{v}^a\right\|^2$ with respect to $\mathbf{u}$ and w, where $\mathbf{v}^a$ corresponds to the leg lengths associated with the three identified equality constraints. This bifurcation point mapping is automatically done by the computer code as it maps the boundary.

The results for the modified planar Stewart platform is qualitatively the same as for the standard platform, except that for the modified case there is only five smooth boundary curves with bifurcation point B $(1\ 0\ 1)$ lying inside the workspace. Here the two smooth boundary curves AB and BC of the standard case blend into a single smooth boundary curve AC, which consists of three parts: AA' $[1\ -\ 1]$, $A'C'$ $[1\ -\ -]$, and $C'C$ $[1\ 0\ -]$. It is clear that along $A'C'$ the platform is stretched to be collinear with actuator leg 1 so that only the single constraint $l_1 = l_1^{max}$ is active.

The point A' may be determined in a manner similar to the way in which the corner bifurcation points were obtained by minimizing, with regard to $\mathbf{u}$ and $\mathbf{v}$, the following error function:

$$e(\mathbf{u}, w) = \left(v_1(\mathbf{u}, w) - v_1^{max}\right)^2 + \left(v_3(\mathbf{u}, w) - v_3^{max}\right)^2 + \left(u_2 - (u_1 + 1)\tan(w)\right)^2 \qquad (2.24)$$

The first two terms of error function (2.24) correspond with the two active constraints at A' and the last term to the collinearity condition which also applies at A'. Similarly, point C' is determined by setting $v_1(\mathbf{u}, w) = v_1^{max}$, $v_2(\mathbf{u}, w) = v_2^{min}$ and $u_2 = (u_1 + 1)\tan(w)$. In both cases the optimization code *LFOPCV3* [40] reduces the error value to zero, giving the desired solutions.

A comparison between the workspace boundaries obtained and depicted here, with the results of Haug et al. [12], shows that equally accurate results are obtained with relative ease using the basic optimization approach.

2.6.3.2 Curves Connecting Bifurcation Points

From further inspection of Figure 2.9 and Figure 2.10, it is apparent that in the standard case only six, and in the modified case only five of the eight bifurcation points occur on the boundary. The remaining two points for the standard case are $G(1\ 1\ 0)$ and $H(0\ 0\ 1)$, and occur in the interior. For the modified case point $B(1\ 0\ 1)$ is also an interior point. These interior bifurcation points, at which in each case three constraints are active, may be determined in exactly the same manner as previously described for the boundary bifurcation points. For the standard case bifurcation points G and H almost coincide in the **u** plane. The precise respective coordinates are:

$$\text{for } G(1\ 1\ 0),\ u_1 = 0.92857151,\ u_2 = 1.3608971,\ w = -0.38025119$$

$$\text{and for } H\ (0\ 0\ 1), u_1 = 0.93166249,\ u_2 = 1.363325,\ w = 0.37183426$$

These results are exactly the same as those given by Haug et al. [12].

To complete the picture, interior curves connecting boundary bifurcation points to interior bifurcation points, and along which only one of the actuator lengths is allowed to vary, were also computed. These interior curves are of importance since, according to Haug et al. [42], limits on controllability of the planar Stewart platform are associated with configurations lying on the interior curves.

The method of mapping the interior curves is described with reference to the representative curve connecting boundary bifurcation point $A(1\ 1\ 1)$ to $G(1\ 1\ 0)$. Along this curve $[1\ 1\ -]$, $v_1 = v_1^{max}$, $v_2 = v_2^{max}$ and v_3 varies between v_3^{max} and v_3^{min}. M points along this curve may be mapped by successively solving, for $j = 1,2,3,...,M$, the following set of non-linear equations:

$$\begin{aligned} v_1(\mathbf{u}, w) - v_1^{max} &= 0 \\ v_2(\mathbf{u}, w) - v_2^{max} &= 0 \\ v_3(\mathbf{u}, w) - v_3^{j} &= 0 \end{aligned} \qquad (2.25)$$

$$\text{where } v_3^{j} = v_3^{max} - \frac{j}{M}\left(v_3^{max} - v_3^{min}\right)$$

This may readily be done by minimizing the sum of the squares of the residual errors, again using the *LFOPCV3* optimization code. For clarity, the computed interior curves are shown separately on Figure 2.11 and Figure 2.12 for the two individual platforms.

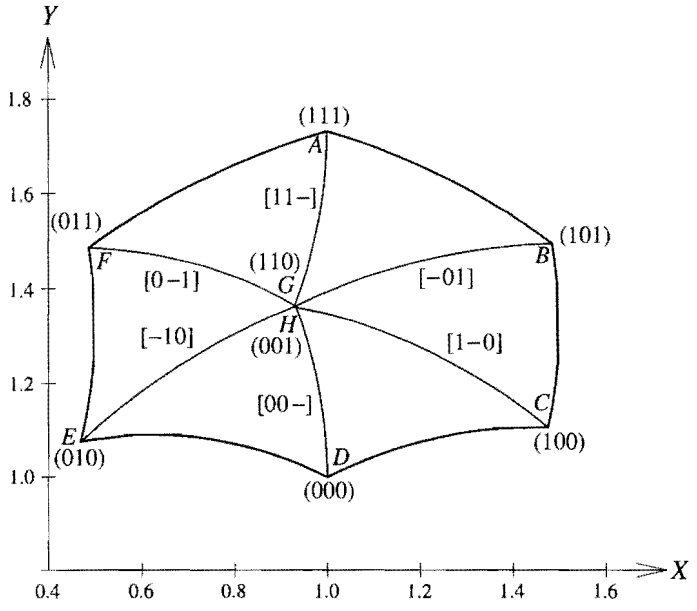

Figure 2.11 Computed curves for the *standard* planar Stewart platform ($1 \le l_3 \le \sqrt{3}$).

A final matter of interest concerns paths FH $[0\ -\ 1]$ and HD $[0\ 0\ -]$ for the *modified* planar Stewart platform shown in Figure 2.12. Along each of these paths there are respective points F' and D' at which, with leg 1 at its minimum position, a collinear and singular configuration is assumed. These points F' and D' are computed in a manner similar to the determination of A' and C' described in Section 2.6.3.1, but now with $v_1 = v_1^{\min}$. The circular arc $F'D'$, of radius $1+\sqrt{2}$ and center at global coordinates $(x, y) = (-1, 0)$, therefore designates the path of the working point when the planar Stewart platform assumes a collinear configuration with actuator leg 1 at its minimum position.

This concludes the presentation of the accessible workspace results for the planar Stewart platform. From an implementation point of view, it is important to state that all the techniques described here, and used to generate the workspace boundary and bifurcation curves, are integrated in a *Fortran* computer code *PLANSTEW* that is easy to use. The user specifies the limits on the leg lengths, and the code then automatically computes and plots the accessible workspace boundaries, as well as the curves connecting the bifurcation points situated on the outer boundary with those situated inside the accessible output set. The code *PLANSTEW* is available from the author on request. The details of the code is explained in Appendix A.

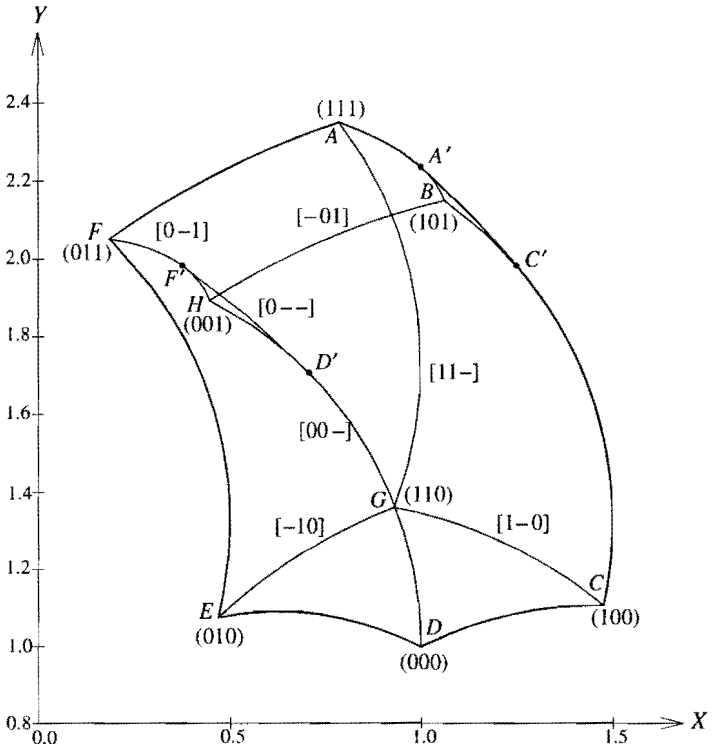

Figure 2.12 Computed curves for the *modified* planar Stewart platform ($1 \leq l_3 \leq 3$).

Note that nothing has been said about the values that the orientation angle φ assumes within the workspace. While determining the boundaries of the *accessible* workspace, the main interest is the maximum allowable displacement from the radiating point $\mathbf{u}^0$ irrespective of orientation. The value of the orientation angle φ is only a concern if it is apparent that the top platform assumes a flipped configuration where interference of the legs with each other becomes a possibility.

The next section deals with determining the *dexterous workspace* of the planar Stewart platform, where the orientation angle plays a primary role.

2.6.4 Determining the Dexterous Workspace of the Planar Stewart Platform

2.6.4.1 Introduction

The *dextrous workspace* of a parallel manipulator is *defined* by Haug et al. [8] as: "(the boundary of) the set of points that can be reached by a given point on the working body and at which specified *ranges* of rotation of the working body can be achieved." Clearly the dextrous workspace is not unique but depends on the specified ranges of rotations. It is also apparent that for any non-zero range of orientations the dextrous workspace will be a subset of the accessible workspace.

Haug et al. [8] explain that it is important to distinguish between the dexterous workspace and the accessible workspace of a manipulator. The literature often discusses the "workspace" of a manipulator, yet it often happens that the manipulator cannot "work" while following a continuous path within this so called workspace [43, 44], because it is essentially an accessible rather than a dextrous workspace and contains points at which no range of rotation is possible.

From the definition of a dextrous workspace it follows that for any given manipulator, a range of dextrous workspaces exists. Once the dexterity requirements for the manipulator are stipulated, the dexterous workspace within which the specific dexterity requirements are satisfied, can be determined. Adjusting the dexterity requirements will obviously result in a completely different dextrous workspace.

Haug et al. [8] mention that dexterity requirements for a manipulator are often stated in terms of ranges of mobility, normally rotatability, that must be achieved at each point in the desired accessible output set.

For the planar Stewart platform under consideration, any range of rotatability will be specified with relation to the orientation angle φ of the top platform, i.e. φ must be able to assume *all* values in the range $[\varphi_{min} - \varphi_{max}]$ at *any* point in the associated dextrous workspace.

With the orientation angle φ of the planar Stewart platform defined as the intermediate coordinate w ($w = \varphi$, see Section 2.6.2), one may naïvely expect that any such dexterity requirement can directly be translated to inequality constraints imposed on the intermediate coordinate of the form.

$$w_{min} \leq w \leq w_{max} \tag{2.26}$$

Seeing that expression (2.26) corresponds to expression (2.3), it is possible to solve optimization *Problem (i)* with the additional inequalities as given by expression (2.26). With reference to Section 2.3 this would imply maximizing the displacement from the radiating point $\mathbf{u}^0$ with inequality constraints imposed in both the actuator leg lengths (input coordinates) and the orientation angle of the top platform (intermediate coordinate).

The optimum solution to this problem (maximum displacement from $\mathbf{u}^0$) does however not yield points at the boundary where *all* orientations in the range $[\varphi_{min} - \varphi_{max}]$ are possible. In fact in general one may expect only one possible orientation in the range at a specific boundary point, and therefore the boundary thus obtained will not coincide with the boundary of the dextrous workspace for $[\varphi_{min} - \varphi_{max}]$.

In order to compute the dextrous workspace for the range $[\varphi_{min} - \varphi_{max}]$, denoted by $\boldsymbol{A}[\varphi_{min} - \varphi_{max}]$, it is necessary to first consider the fixed orientation accessible workspace $\boldsymbol{A}[\varphi_{fix}]$.

2.6.4.2 The Fixed Orientation Accessible Workspace of the Planar Stewart Platform

Consider the situation where a single dexterity requirement needs to be defined for the planar Stewart platform. This is the case where the accessible workspace for a fixed orientation of the moving platform is to be determined. Such a *fixed orientation* requirement is expressed as an equality:

$$\varphi = \varphi_{fixed} \tag{2.27}$$

and the associated accessible workspace is denoted by $\boldsymbol{A}[\varphi_{fix}]$.

Equation (2.27) is in actual fact an equality constraint fixing the value of the intermediate coordinate, i.e.

$$w = w_{fixed} \tag{2.28}$$

If, instead of the additional inequality constraints (2.26), an additional equality constraint (2.28) is added to optimization *Problem (i)*, the optimum solution will correspond to a position where the *fixed orientation* requirement is achieved. The *modified* optimization *Problem (i)* is:

***Modified* Problem (i)**:

$$\underset{\mathbf{u},w}{\text{maximize}} \ \left\|\mathbf{u} - \mathbf{u}^0\right\|$$

$$\text{such that:} \quad \mathbf{v}^{min} \le \mathbf{v}(\mathbf{u}, w) \le \mathbf{v}^{max}$$

$$\text{and subject to equality constraints:} \quad \begin{matrix} \mathbf{h}(\mathbf{u},\mathbf{s}) = \mathbf{0}, \ \mathbf{h} \in \mathrm{R}^{nu-1} \\ w = w_{fix} \end{matrix}$$

Solving the modified problem yields a point on the boundary of the fixed orientation accessible workspace. The complete boundary of $\boldsymbol{A}[\varphi_{fix}]$ may now be numerically mapped as before, by solving the modified problem for successive rays emanating from $\mathbf{u}^0$ at angular intervals δ (see Figure 2.2).

2.6.4.3 Computed Fixed Orientation Accessible Workspaces of the Planar Stewart Platform

The fixed orientation workspace $\boldsymbol{A}[0^\circ]$ where the top platform is fixed in a horizontal orientation, i.e., $\varphi = \varphi_{fixed} = 0^\circ$, is shown in Figure 2.13. The angular unrestricted accessible workspace is shown for

comparison purposes. The fixed orientation workspace is clearly a proper subset of the accessible workspace.

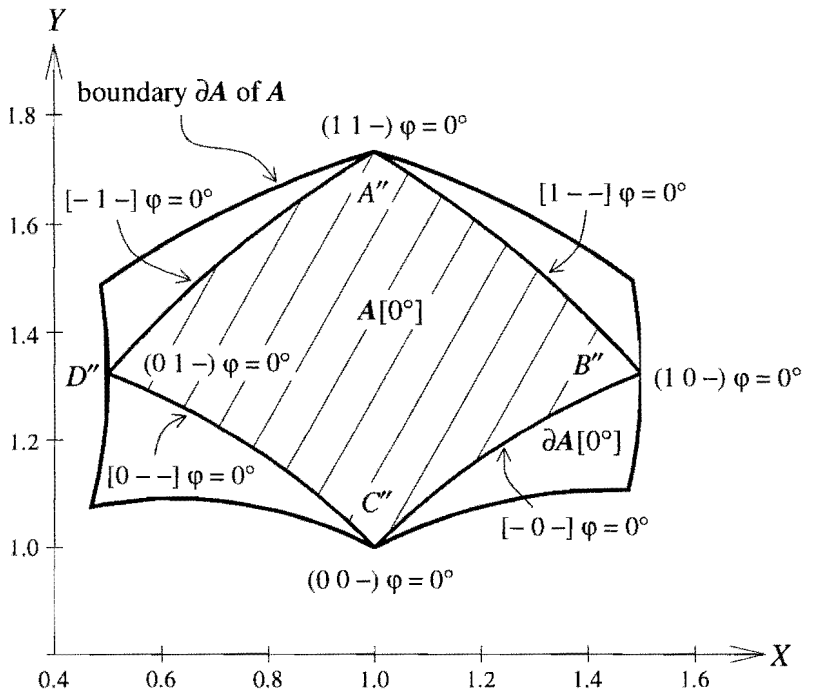

Figure 2.13 Fixed orientation workspace $A[0^\circ]$ inside the unrestricted accessible workspace A.

As an extension to the proposed labeling notation (see Sections 2.5.3 and 2.6.3), the bifurcation points and boundary curves of the fixed orientation accessible output set $A[0^\circ]$ are also labeled. Here the labeling notation is slightly modified to include the specification of the fixed orientation $\varphi = 0^\circ$.

The mapping of each of the four boundary curves is characterized by the active "search direction" equality constraint, the active "fixed orientation" equality constraint and also a single active inequality constraint. This means that only one actuator leg is at an extreme length as the working point advances along the fixed orientation boundary curves shown in Figure 2.13.

Each of the four bifurcation points therefore correspond to the position of the working point with at least two legs at extreme lengths. Consider for example bifurcation point B'', which is labeled $(1\ \ 0\ \ -)\ \varphi = 0^\circ$. This label indicates that for the dexterity requirement $\varphi = 0^\circ$, the working point coincides with bifurcation point B'' if $l_1 = l_1^{\max}$ and $l_2 = l_2^{\min}$. The length of actuator leg 3 is determined by the fixed orientation $\varphi = 0^\circ$.

As a result of the choice of leg length limits, the top platform is horizontal when it is in its highest possible and lowest possible positions. This is why bifurcation points $A''(1\ \ 1\ \ -)\ \varphi = 0^\circ$ and

$C''(0\ \ 0\ \ -)\ \varphi = 0^\circ$ in Figure 2.13 respectively coincide with bifurcation points $A(1\ \ 1\ \ 1)$ and $C(0\ \ 0\ \ 0)$ in Figure 2.9. The choice of the actuator leg length limits allows labeling bifurcation points A'' and C'' as: $A''(1\ \ 1\ \ 1)\ \varphi = 0^\circ$ and $C''(0\ \ 0\ \ 0)\ \varphi = 0^\circ$.

The fixed orientation boundary curves are labeled in a similar manner. Boundary curve $A''B''$ is, for example, labeled $[1\ \ -\ \ -]\ \varphi = 0^\circ$ showing that $l_1 = l_1^{max}$ as the working point advances along this curve. Actuator leg 2 varies from its minimum length at bifurcation point B'' to its maximum length at bifurcation point A'', and once again, l_3 is determined by the fixed orientation $\varphi = 0^\circ$. The other bifurcation points and boundary curves are similarly labeled (see Figure 2.13).

2.6.4.4 Using Fixed Orientation Workspaces to Determine a Dextrous Workspace

The mapping of the fixed orientation workspace may now be extended to determine the dextrous workspace $A[\varphi_{min} - \varphi_{max}]$ where the dexterity requirement is:

φ to assume *all* values in the range $[\varphi_{min} - \varphi_{max}]$ at *any* point in the dextrous workspace (2.29)

It should be clear that $A[\varphi_{min} - \varphi_{max}]$ is given by the intersection of all possible $A[\varphi_{fix}]$, $\varphi_{fix} \in [\varphi_{min} - \varphi_{max}]$. Since it is expected that $A[\varphi_{fix}]$ varies in a "continuous" manner with φ_{fix}, the reasonable assumption is now made that $A[\varphi_{min} - \varphi_{max}]$ may be obtained by simply considering the intersection of the extreme fixed angle sets, i.e.

$$A[\varphi_{min} - \varphi_{max}] = A[\varphi_{min}] \bigcap A[\varphi_{max}] \tag{2.30}$$

The validity of assumption (2.30) may in practice be reinforced by checking whether at the intermediate central value, φ_i, the following condition is satisfied:

$$\{A[\varphi_{min}] \bigcap A[\varphi_{max}]\} \subset A[\varphi_i] \tag{2.31}$$

where $\varphi_i = (\varphi_{min} + \varphi_{max})/2$.

{Indeed for the examples considered here condition (2.31) is more than satisfied – see Figure 2.13 where $A[\varphi_i] = A[0^\circ]$.}

Thus, if the orientation of the top platform is fixed to the minimum value as specified in the fixed orientation requirement, i.e. $\varphi = \varphi_{fixed} = \varphi_{min}$, the minimum fixed orientation workspace $A[\varphi_{min}]$ is mapped. Next the maximum fixed orientation ($\varphi = \varphi_{fixed} = \varphi_{max}$) set $A[\varphi_{max}]$ is mapped. The intersection or overlapping area is the dextrous workspace $A[\varphi_{min} - \varphi_{max}]$ within which the full dexterity requirement (2.29) is met.

2.6.4.5 Computed Dextrous Workspace

As an example of the application of the above methodology, consider the following rotatability requirement for the top platform of the planar Stewart platform:

$$\varphi \text{ to assume } \textit{all} \text{ values in range } [(-10^\circ)-(10^\circ)] \text{ at } \textit{any} \text{ point in } \boldsymbol{A}[(-10^\circ)-(10^\circ)]$$

The minimum fixed orientation workspace $\boldsymbol{A}[-10^\circ]$ and maximum fixed orientation workspace $\boldsymbol{A}[10^\circ]$ are shown in Figure 2.14. The intersection or overlap of these two workspaces gives the dextrous workspace $\boldsymbol{A}[(-10^\circ)-(10^\circ)]$, indicated by the shaded region, within which the full range rotatability is achieved.

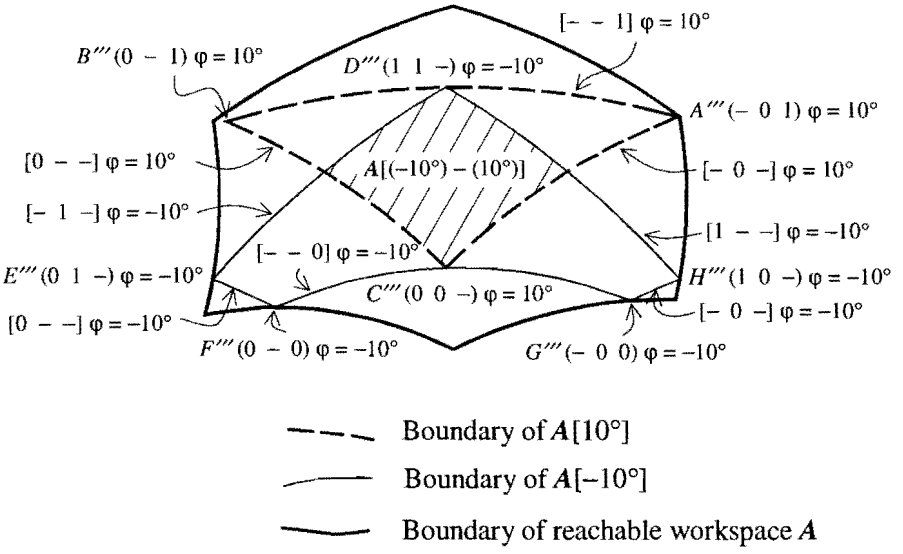

Figure 2.14 Dextrous accessible output set $\boldsymbol{A}[(-10^\circ)-(10^\circ)]$.

In accordance with the work of Haug et al. [8], the boundaries of the dexterous accessible output sets for which φ achieves the full ranges $[(-5^\circ)-(5^\circ)]$, $[(-10^\circ)-(10^\circ)]$ and $[(-15^\circ)-(15^\circ)]$ of rotatability are respectively shown in Figure 2.15. These boundaries are plotted together with the boundaries of the fixed orientation workspace $\boldsymbol{A}[0^\circ]$ and of the orientationally unrestricted workspace $\boldsymbol{A}$.

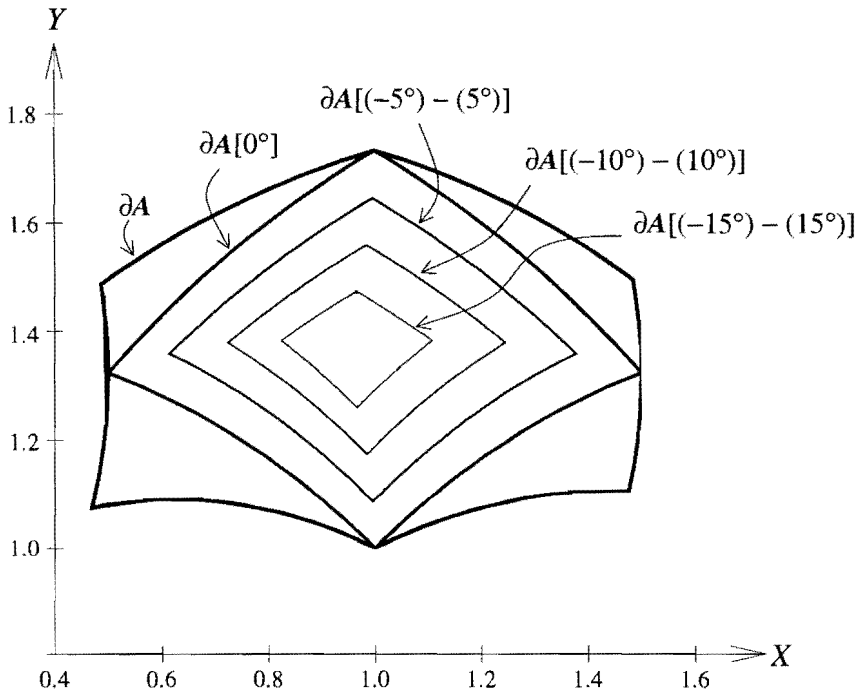

Figure 2.15 Dextrous accessible output sets for different full-range rotatability requirements.

Figure 2.15 correspond exactly to the results obtained by Haug et al. [8], and when analyzed, the results confirm the accuracy of the method proposed here.

The orientationally unrestricted accessible workspace is, as expected, bounded by the exterior boundary ∂A shown in Figure 2.15. For each search direction, the top platform is "displaced" further and further away the radiating point $\mathbf{u}^0$, as far as the leg length limits allow. It follows that for each point along the boundary of the reachable workspace, the orientation of the top platform depends on the extreme lengths of the two "active" actuator legs of that search direction.

As soon as the orientation of the top platform is fixed the maximum displacement from $\mathbf{u}^0$ is limited by the first actuator leg reaching its extreme length. This explains why the fixed orientation workspaces $A[\varphi_{fix}]$ are smaller than the unrestricted accessible workspace. Forcing the orientation of the top platform to remain fixed, prohibits any further rotation of the top platform. With no orientation limits imposed, the top platform can be tilted differently for each search direction, allowing for a maximum displacement from $\mathbf{u}^0$ which corresponds to an orientation with more than one actuator leg reaching its extreme value.

2.7 CONCLUSION

The optimization approach presented in this chapter successfully determines the workspaces of the planar manipulators investigated here. It is evident that this new optimization approach represents a very promising general tool for determining *and* analyzing manipulator workspaces. Computing the boundary of the workspace using the optimization approach allows the various sections of the workspace boundary, to be related to the behavior of the manipulator.

A new and concise notation for labeling the different bifurcation points and curves is also introduced here. It is believed that this, in general, greatly facilitates the description of the behavior of mechanisms within and on the boundary of the associated workspaces.

The computer code *PLANSTEW* demonstrates the ability to automate the process to allow the user to automatically map both outer boundaries of the accessible output sets and interior curves. The interior curves represent configurations at which controllability or mobility of the manipulator may be limited.

As far as the dextrous workspace is concerned, the approach proposed by Haug et al. [8] can successfully account for full range rotatability requirements of closed loop manipulators. However, one of the concluding remarks of Haug et al. is: "...the computations that result in solving the necessary conditions of the boundaries of the accessible output sets, however are shown to be tedious even for the planar manipulators studied". In contrast, the approach presented here may easily be implemented and automated.

The optimization approach also accounts for the full range rotatability requirements, and because the dexterity requirement is simply treated as an additional equality constraint, the dextrous accessible output set is easily mapped.

In the next chapter, the optimization approach, as developed here for planar manipulators, is extended to apply to a six-legged spatial Stewart platform.

Chapter 3

3 THE DETERMINATION OF THE ORIENTATIONALLY UNCONSTRAINED SPATIAL MANIPULATOR WORKSPACES

3.1 INTRODUCTION

The methodology proposed for, and applied to the determination of the workspaces of *planar* mechanisms in Chapter 2 may readily be extended to apply to spatial mechanisms, such as the Stewart platforms considered by Haug et al. [12] and Liu et al. [18].

Taking the 6–3 Stewart platform of Liu et al. [18] as a representative example, the "planar" optimization approach, developed in Chapter 2, is used in this chapter to map three-dimensional workspaces of this six–DOF manipulator. The geometry of this 6–3 Stewart platform is shown in Figure 3.1.

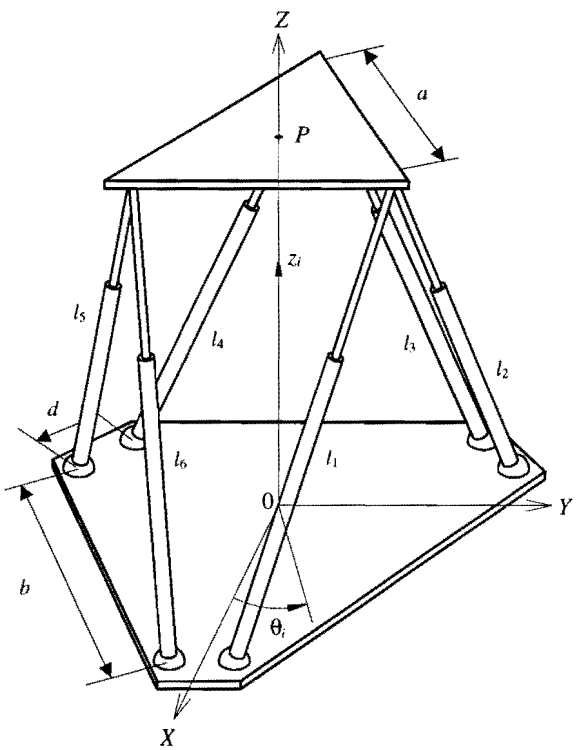

Figure 3.1 Geometry of the 6–3 Stewart platform.

The workspaces to be considered in this study are:

(i) the orientationally unconstrained reachable workspace A, with boundary denoted by ∂A,

(ii) the fixed orientation workspace $A[\alpha_{fix}, \beta_{fix}, \gamma_{fix}]$, with boundary indicated by $\partial A[\alpha_{fix}, \beta_{fix}, \gamma_{fix}]$, and

(iii) an example of a dextrous workspace $A[\alpha_{fix}, \beta_{fix}, \gamma_{min} - \gamma_{max}]$, with boundary $\partial A[\alpha_{fix}, \beta_{fix}, \gamma_{min} - \gamma_{max}]$.

The corresponding different types of workspaces, (i), (ii) and (iii), were defined and determined for the planar Stewart platform considered in Section 2.6. Case (i) of the 6–3 Stewart platform is dealt with in this chapter, while cases (ii) and (iii) are dealt with in Chapter 4.

3.2 GEOMETRY OF THE 6–3 STEWART PLATFORM

As for the planar Stewart platform described in Section 2.6.1 the spatial Stewart platform also has a moving upper platform, as well as a fixed base. The base is a semi-regular hexagon, which in this case is also fixed in a horizontal position, while the upper platform is an equilateral triangle.

Figure 3.1 shows the global coordinate system fixed at the center of the base with the global Z-axes pointing vertically upwards. The working point P of the spatial Stewart platform is at the centroid of the upper triangular platform.

The spatial Stewart platform has six linear actuator legs connecting the moving upper platform, to the fixed base. The bottom ends of the actuator legs are connected to the six vertices of the base, while the top ends of the legs are connected to the three vertices of the upper platform as shown in Figure 3.1. The base platform connections are ball-and-socket (spherical) joints, while the moving platform connections are gimbals. Fichter [17] proposed these gimbals as described in Section 1.4. This arrangement is referred to as a 6–3 Stewart platform (see Section 1.4).

Varying the lengths of the linear actuators, indicated by l_i, $i = 1, 2, ..., 6$, will not only change the position of the upper platform, but also its orientation, adding up to the six DOF of the manipulator.

Adopting the definitions of Liu et al. [18], the position of the upper platform is given by the global coordinates of the working point P denoted here by (x, y, z), and the orientation of the upper platform is given by the orientation angles (α, β, γ). Liu et al. explain the orientation angles as, firstly rotating the top platform about the OX-axis through an angle α, then about the OY-axis through an angle β, and finally

about the axis radiating form the manipulator working point and fixed perpendicular to the top platform through an angle γ.

According to Liu et al. [18], the defined orientation angles have a physical meaning in that the α and β angles define an "approach vector" of the top platform, while the γ angle defines the roll of the top platform about the approach vector.

As with the planar Stewart platform, the orientationaly unconstrained reachable workspace of the spatial Stewart platform defines the *accessible* region of the working point P, and is determined by the limitations on the actuator leg lengths (see Section 2.2).

The actuator leg lengths are again the *input variables*, i.e. $\mathbf{v} = [l_1, l_2, l_3, l_4, l_5, l_6]^T$ on which the following inequality constraints, corresponding to expression (2.18) in the planar case (Section 2.6.1), are imposed:

$$0 < l_i^{\min} \leq l_i \leq l_i^{\max} \tag{3.1}$$

for $i = 1, 2, 3, ..., 6$.

Liu et al. [18] apply their kinematic analyses to an example where they propose certain dimensions for the top and bottom platforms, as well as for the actuator leg limits. In order for this example to be used for comparison purposes in the current optimization approach, the dimensions of the 6–3 Stewart platform analyzed in this chapter is in accordance with the example of Liu et al. [18].

It is important to note that, although different minimum and maximum leg length limits were prescribed for the different legs of the planar Stewart platform, here all six actuator legs of the spatial manipulator have the same leg length limits, i.e. $l_i^{\min} = 8.0$ and $l_i^{\max} = 15.0$ for $i = 1, 2, 3, ..., 6$. The dimensions of the top and base platforms are: $a = 10.0$, $b = 15.0$ and $d = 1.0$ (see Figure 3.1).

3.3 CONSTRAINT EQUATIONS OF THE 6–3 STEWART PLATFORM

With reference to Section 2.2, the global coordinates of the working point P on the 6–3 Stewart platform are the *output coordinates*, i.e. $\mathbf{u} = [x, y, z]^T$, and the orientation angles of the upper platform, are the *intermediate coordinates*, i.e. $\mathbf{w} = [\alpha, \beta, \gamma]^T$.

The defined input, output and intermediate coordinates of the 6–3 Stewart platform correspond to the definitions of these coordinates given in Section 2.6.2. This explains the correlation between the generalized coordinates of the spatial and planar Stewart platforms.

The spatial Stewart platform has 12 generalized coordinates compared the 6 of the planar Stewart platform. The spatial platform coordinates are:

$$\begin{aligned}\mathbf{q} &= \left[\mathbf{u}^{\mathrm{T}} \quad \mathbf{v}^{\mathrm{T}} \quad \mathbf{w}^{\mathrm{T}}\right]^{\mathrm{T}} \\ &= \left[x,\ y,\ z,\ l_1,\ l_2,\ldots,\ l_6,\ \alpha,\ \beta,\ \gamma\right]^{\mathrm{T}}\end{aligned} \tag{3.2}$$

The spatial Stewart platform obviously has six degrees of freedom, and the six kinematic constraint equations of general form (2.1), are the six equations expressing the length of each leg in terms of the position and orientation coordinates. These analytical expressions can readily be found by doing the inverse kinematic analysis as described by Liu et al. [18]. These expressions, corresponding to (2.20) for the planar case, are as follows:

$$\begin{aligned}
l_1 &= \sqrt{\left(X_{T1} - \tfrac{d}{2\sqrt{3}} - \tfrac{b}{\sqrt{3}}\right)^2 + \left(Y_{T1} - \tfrac{d}{2}\right)^2 + Z_{T1}^2} \\
l_2 &= \sqrt{\left(X_{T1} - \tfrac{d}{2\sqrt{3}} + \tfrac{b}{2\sqrt{3}}\right)^2 + \left(Y_{T1} - \tfrac{d}{2} - \tfrac{b}{2}\right)^2 + Z_{T1}^2} \\
l_3 &= \sqrt{\left(X_{T2} + \tfrac{d}{\sqrt{3}} + \tfrac{b}{2\sqrt{3}}\right)^2 + \left(Y_{T2} - \tfrac{b}{2}\right)^2 + Z_{T2}^2} \\
l_4 &= \sqrt{\left(X_{T2} + \tfrac{d}{\sqrt{3}} + \tfrac{b}{2\sqrt{3}}\right)^2 + \left(Y_{T2} + \tfrac{b}{2}\right)^2 + Z_{T2}^2} \\
l_5 &= \sqrt{\left(X_{T3} - \tfrac{d}{2\sqrt{3}} + \tfrac{b}{2\sqrt{3}}\right)^2 + \left(Y_{T3} + \tfrac{d}{2} + \tfrac{b}{2}\right)^2 + Z_{T3}^2} \\
l_6 &= \sqrt{\left(X_{T3} - \tfrac{d}{2\sqrt{3}} - \tfrac{b}{\sqrt{3}}\right)^2 + \left(Y_{T3} + \tfrac{d}{2}\right)^2 + Z_{T3}^2}
\end{aligned} \tag{3.3}$$

where

$$\begin{aligned}
X_{T1} &= x + \tfrac{a}{\sqrt{3}}\left[\sin(\alpha)\sin(\beta)\sin(\gamma+60^\circ) + \cos(\beta)\cos(\gamma+60^\circ)\right] \\
Y_{T1} &= y + \tfrac{a}{\sqrt{3}}\cos(\alpha)\sin(\gamma+60^\circ) \\
Z_{T1} &= z + \tfrac{a}{\sqrt{3}}\left[\sin(\alpha)\cos(\beta)\sin(\gamma+60^\circ) - \sin(\beta)\cos(\gamma+60^\circ)\right] \\
X_{T2} &= x - \tfrac{a}{\sqrt{3}}\left[\sin(\alpha)\sin(\beta)\sin(\gamma) + \cos(\beta)\cos(\gamma)\right] \\
Y_{T2} &= y - \tfrac{a}{\sqrt{3}}\cos(\alpha)\sin(\gamma) \\
Z_{T2} &= z - \tfrac{a}{\sqrt{3}}\left[\sin(\alpha)\cos(\beta)\sin(\gamma) - \sin(\beta)\cos(\gamma)\right] \\
X_{T3} &= x + \tfrac{a}{\sqrt{3}}\left[\sin(\alpha)\sin(\beta)\sin(\gamma-60^\circ) + \cos(\beta)\cos(\gamma-60^\circ)\right] \\
Y_{T3} &= y + \tfrac{a}{\sqrt{3}}\cos(\alpha)\sin(\gamma-60^\circ) \\
Z_{T3} &= z + \tfrac{a}{\sqrt{3}}\left[\sin(\alpha)\cos(\beta)\sin(\gamma-60^\circ) - \sin(\beta)\cos(\gamma-60^\circ)\right]
\end{aligned} \tag{3.4}$$

In expressions (3.3) and (3.4) a is the length of the sides of the upper equilateral triangular moving platform, and b and d are respectively the short and long sides of the hexagonal base (see Figure 3.1).

Expression (3.3) is written in standard form (2.5) as:

$$\mathbf{\Phi}(\mathbf{u}\quad \mathbf{v}\quad \mathbf{w}) = \begin{bmatrix} v_1^2 - \left(X_{T1} - \frac{d}{2\sqrt{3}} - \frac{b}{\sqrt{3}}\right)^2 - \left(Y_{T1} - \frac{d}{2}\right)^2 - Z_{T1}^2 \\ v_2^2 - \left(X_{T1} - \frac{d}{2\sqrt{3}} + \frac{b}{2\sqrt{3}}\right)^2 - \left(Y_{T1} - \frac{d}{2} - \frac{b}{2}\right)^2 - Z_{T1}^2 \\ v_3^2 - \left(X_{T2} + \frac{d}{\sqrt{3}} + \frac{b}{2\sqrt{3}}\right)^2 - \left(Y_{T2} - \frac{b}{2}\right)^2 - Z_{T2}^2 \\ v_4^2 - \left(X_{T2} + \frac{d}{\sqrt{3}} + \frac{b}{2\sqrt{3}}\right)^2 - \left(Y_{T2} + \frac{b}{2}\right)^2 - Z_{T2}^2 \\ v_5^2 - \left(X_{T3} - \frac{d}{2\sqrt{3}} + \frac{b}{2\sqrt{3}}\right)^2 - \left(Y_{T3} + \frac{d}{2} + \frac{b}{2}\right)^2 - Z_{T3}^2 \\ v_6^2 - \left(X_{T3} - \frac{d}{2\sqrt{3}} - \frac{b}{\sqrt{3}}\right)^2 - \left(Y_{T3} + \frac{d}{2}\right)^2 - Z_{T3}^2 \end{bmatrix} = \mathbf{0} \qquad (3.5)$$

where

$$\begin{aligned} X_{T1} &= u_1 + \tfrac{a}{\sqrt{3}}\left[\sin(w_1)\sin(w_2)\sin(w_3 + 60^\circ) + \cos(w_2)\cos(w_3 + 60^\circ)\right] \\ Y_{T1} &= u_2 + \tfrac{a}{\sqrt{3}}\cos(w_1)\sin(w_3 + 60^\circ) \\ Z_{T1} &= u_3 + \tfrac{a}{\sqrt{3}}\left[\sin(w_1)\cos(w_2)\sin(w_3 + 60^\circ) - \sin(w_2)\cos(w_3 + 60^\circ)\right] \\ X_{T2} &= u_1 - \tfrac{a}{\sqrt{3}}\left[\sin(w_1)\sin(w_2)\sin(w_3) + \cos(w_2)\cos(w_3)\right] \\ Y_{T2} &= u_2 - \tfrac{a}{\sqrt{3}}\cos(w_1)\sin(w_3) \\ Z_{T2} &= u_3 - \tfrac{a}{\sqrt{3}}\left[\sin(w_1)\cos(w_2)\sin(w_3) - \sin(w_2)\cos(w_3)\right] \\ X_{T3} &= u_1 + \tfrac{a}{\sqrt{3}}\left[\sin(w_1)\sin(w_2)\sin(w_3 - 60^\circ) + \cos(w_2)\cos(w_3 - 60^\circ)\right] \\ Y_{T3} &= u_2 + \tfrac{a}{\sqrt{3}}\cos(w_1)\sin(w_3 - 60^\circ) \\ Z_{T3} &= u_3 + \tfrac{a}{\sqrt{3}}\left[\sin(w_1)\cos(w_2)\sin(w_3 - 60^\circ) - \sin(w_2)\cos(w_3 - 60^\circ)\right] \end{aligned} \qquad (3.6)$$

from which in turn, given **u** and **w**, one may solve for **v**:

$$\mathbf{v} = \mathbf{v}(\mathbf{u},\ \mathbf{w}) = \begin{bmatrix} \sqrt{\left(X_{T1} - \frac{d}{2\sqrt{3}} - \frac{b}{\sqrt{3}}\right)^2 + \left(Y_{T1} - \frac{d}{2}\right)^2 + Z_{T1}^2} \\ \sqrt{\left(X_{T1} - \frac{d}{2\sqrt{3}} + \frac{b}{2\sqrt{3}}\right)^2 + \left(Y_{T1} - \frac{d}{2} - \frac{b}{2}\right)^2 + Z_{T1}^2} \\ \sqrt{\left(X_{T2} + \frac{d}{\sqrt{3}} + \frac{b}{2\sqrt{3}}\right)^2 + \left(Y_{T2} - \frac{b}{2}\right)^2 + Z_{T2}^2} \\ \sqrt{\left(X_{T2} + \frac{d}{\sqrt{3}} + \frac{b}{2\sqrt{3}}\right)^2 + \left(Y_{T2} + \frac{b}{2}\right)^2 + Z_{T2}^2} \\ \sqrt{\left(X_{T3} - \frac{d}{2\sqrt{3}} + \frac{b}{2\sqrt{3}}\right)^2 + \left(Y_{T3} + \frac{d}{2} + \frac{b}{2}\right)^2 + Z_{T3}^2} \\ \sqrt{\left(X_{T3} - \frac{d}{2\sqrt{3}} - \frac{b}{\sqrt{3}}\right)^2 + \left(Y_{T3} + \frac{d}{2}\right)^2 + Z_{T3}^2} \end{bmatrix} \qquad (3.7)$$

and where X_{T1}, Y_{T1}, Z_{T1}, X_{T2}, Y_{T2}, Z_{T2}, X_{T3}, Y_{T3} and Z_{T3} are given by expressions (3.6).

Finally, (2.1) may more concisely be rewritten as

$$\mathbf{v}^{\min} \le \mathbf{v} \le \mathbf{v}^{\max}$$

$$\textit{where } \mathbf{v}^{\min}\left[l_1^{\min}, l_2^{\min}, \ldots, l_6^{\min}\right]^T \textit{ and } \mathbf{v}^{\max}\left[l_1^{\max}, l_2^{\max}, \ldots, l_6^{\max}\right]^T \qquad (3.8)$$

$$\textit{and } \mathbf{v} = \mathbf{v}(\mathbf{u},\ \mathbf{w}) \textit{ as given by (3.7)}$$

Thus expressions (3.2), (3.3), (3.5), (3.7) and (3.8) here respectively correspond to (2.19), (2.20), (2.21), (2.22) and (2.23) for the planar Stewart platform.

The orientationally unconstrained reachable workspace is computed with no limits on the orientation angles. As will be discussed in Chapter 4, limitations are of course imposed on the angles when the fixed orientation and dextrous workspaces are considered.

3.4 MAPPING THE ACCESSIBLE WORKSPACE OF THE 6–3 STEWART PLATFORM

3.4.1 Introduction

Two options exist by which the reachable workspace of the spatial manipulator can be mapped using the basic methodology presented for the planar accessible set (see Section 2.4).

The first option is to consider the three-dimensional workspace to be represented by a set of *horizontal* slices. For any horizontal *slice*, $z = z_i$, $i = 1, 2, ..., N_S$, the associated two dimensional workspace of the working point P may be determined in a manner analogous to that described for the planar Stewart platform in Section 2.6.2. A composite of the N_S workspace slices then yields a representation of the three-dimensional workspace.

It follows that, for a particular horizontal slice i, the boundary of the workspace $\partial \boldsymbol{A}_i$ may be mapped by solving optimization *Problem (i)* (see Section 2.3) for successive rays emanating from an interior radiating point, but now subject to an additional equality constraint:

$$u_3 = z = z_i \tag{3.9}$$

where z_i designates the height of the slice.

To complete the three dimensional representation of the workspace of the spatial Stewart platform, the boundaries $\partial \boldsymbol{A}_i$ of N_S *slices* are computed. This means that for each *slice i*, the equality constraint equation will be assigned as follows:

$$z_i = z^{\max} - \frac{i}{N_S}\left(z^{\max} - z^{\min}\right) \tag{3.10}$$

for $i = 1, 2, ..., N_S$.

In equation (3.10), $z^{\min}$ and $z^{\max}$ are respectively the lowest and highest possible positions of the working point P measured in terms of the global coordinate system.

For each height z_i, rays emanating in the XY-plane from an interior radiating point will be maximized to determine the boundary $\partial \boldsymbol{A}_i$ of the workspace of *slice i*. With the global Z-axis pointing vertically

upwards from the center of the lower platform, the obvious choice for the radiating point of every *slice*, is at the fixed height z_i of that *slice*, and at the origin of the *XY*-plane.

Alternative to taking horizontal slices, the determination of planar workspace boundaries may also be carried out for successive vertical planes through the central axis *0Z*. This option is preferable as it avoids, to a greater extent than the first option, complications due to non-convexity. The idea is to avoid situations where two boundary points may exist for any specific search direction.

For each plane *i* through *0Z*, there corresponds a unique angle θ_i that the plane makes with the *0X* axis. For this plane the relationship $y_i / x_i = \tan\theta_i$ applies, and therefore in the optimization to determine $\partial \boldsymbol{A}_i$ for this plane, equality constraint (3.9) is replaced by

$$u_{2i} - u_{1i}\tan(\theta_i) = 0 \tag{3.11}$$

The construction of the three-dimensional reachable workspace, is carried out by determining the planar boundaries $\partial \boldsymbol{A}_i$ for a fan of N_P planes, where each plane has a different value of θ_i:

$$\theta_i = \frac{i}{N_P}\left(\frac{2\pi}{3}\right) \tag{3.12}$$

for $i = 1, 2, \ldots, N_P$

It is apparent from the geometry of the spatial 6–3 Stewart platform that the global *Z* axis is a three fold symmetry axis, and therefore it is only necessary to map a third of the complete workspace, corresponding to the θ_i range: $0^\circ - 120^\circ$.

For each plane the same central point, $z^0 = \left(z^{\max} + z^{\min}\right)/2$ on *0Z*, may be used as interior radiating point, i.e.

$$\mathbf{u}^0 = \left(0, 0, z^0\right) \tag{3.13}$$

With the dimensions of the spatial Stewart platform as given in Section 3.2, the exact coordinates of $\mathbf{u}_0$ are:

$$\mathbf{u}^0 = (0, 0, 7.804)$$

3.4.2 Computed Accessible Workspace for the 6–3 Stewart Platform

The vertical plane through the *0X*-axis ($\theta = 0^\circ$) of the computed reachable workspace is shown in Figure 3.2

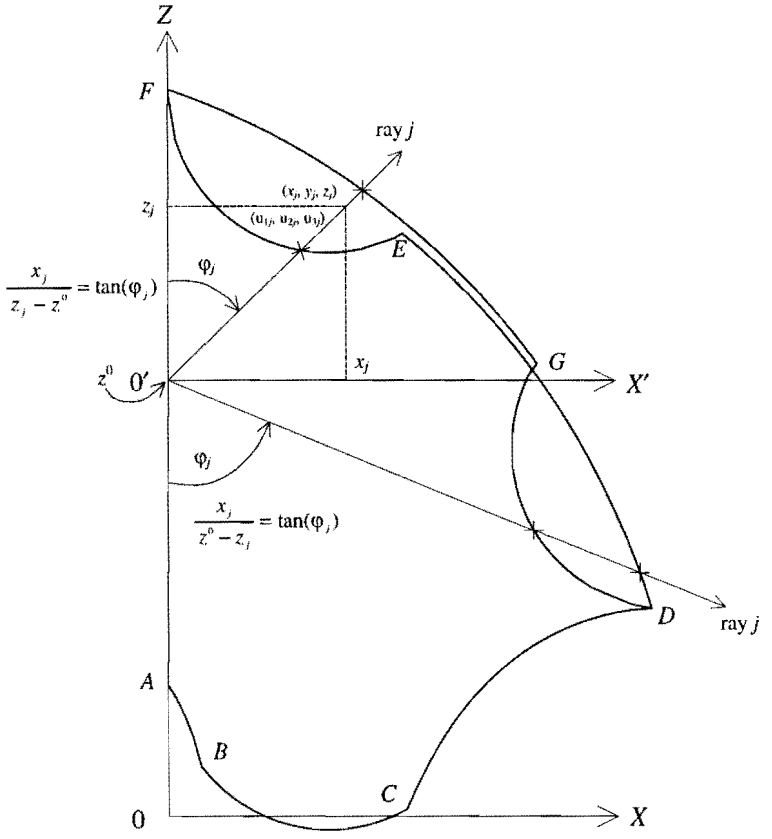

Figure 3.2 Boundaries of the accessible sets for the vertical plane through the *0X*-axis ($\theta = 0^\circ$).

Apparently two different reachable boundaries seem to exist when no constraints are placed on the orientation of the top platform. As will become clear later, the inner boundary corresponds to a near global constrained local optimum solution to optimization *problem (i)*, whereas the outer boundary consists of the global maxima. These two different optima along a ray correspond to the respective maximum displacements of two different *types* of platform configurations as will be shown later.

As explained in Section 3.4.1 two options exist with which the complete accessible workspace can be mapped, namely *vertical planes*, and *horizontal slices*. Although Figure 3.2 shows the accessible sets for the vertical plane through the *0X*-axis ($\theta = 0^\circ$), these results could have been obtained using both options mentioned above. The *vertical planes* option consists of a pencil of rays, restricted to the vertical plane through the *0X*-axis, emanating from the radiating point $\mathbf{u}^0$ at angular intervals. As for the *horizontal slices* option, Figure 3.2 can be mapped using horizontal rays, perpendicular to the *0Z*-axis and restricted to the vertical plane through the vertical plane through the *0X*-axis.

It follows that if the *horizontal slices* option is to be implemented, the highest possible and lowest possible positions of the working point have to be computed before hand to set the upper and lower

bounds between which the horizontal rays are to be incremented. The highest possible position is not a problem, as it is situated at point *F* on the *0Z*-axis, and can therefore easily be determined. Curve *ABCD*, however occupies a lower region than point *A* which is the lowest possible position of the working point if the working point is restricted to move along the *0Z*-axis. Consequently it will be difficult to implement the *horizontal slices* option, as the lower bound of the range of horizontal rays forms part of curve *BC* and cannot be easily determined as part of an automated process. The better option of the two, and the one used here, is the *vertical planes* option, which is easy to implement as the pencil of rays are incremented through the range $0^{\circ} - 180^{\circ}$.

It follows that for each ray restricted to a specific *vertical plane* and intersecting the radiating point $\mathbf{u}_0$ (3.13), a straight line relation must hold. With φ_j defined as the inclination angle between any specific ray *j* and the *0Z*-axis, the following equation must hold:

$$\sqrt{x_j^2 + y_j^2} - (z^0 - z_j)\tan(\varphi_j) = 0 \tag{3.14}$$

Equation (3.14) is rewritten to give the additional equality constraint needed to fix the direction of any specific ray *j*.

$$\sqrt{u_{1j}^2 + u_{2j}^2} - (z^0 - u_{3j})\tan(\varphi_j) = 0 \tag{3.15}$$

The vertical plane is covered by a pencil of N_R rays where each ray *j* has an inclination angle φ_j:

$$\varphi_j = \frac{j}{N_R}(\pi) \tag{3.16}$$

for $j = 0, 1, 2, \ldots, N_R$

Consequently, if *j* = 0, the first ray of each vertical plane will lie parallel to the *0Z*-axis, pointing in the *negative* Z-direction. The first of the two different reachable workspace boundaries in the vertical plane through the *0X*-axis, is mapped by performing an upward sweep of the radiating ray for successive inclination angles given by (3.16) and imposing equation (3.15) as additional equality constraint (see Figure 3.3).

The maximum displacement (from the radiating point $\mathbf{u}_0$) is found for successive rays $j = 1, 2, \ldots, N_R$, using as starting point for each optimization procedure the solution of the previous ray, $j = 0, 1, 2, \ldots, (N_R - 1)$. This limits the possibility of the platform "jumping" between different configurations as the rays are incremented. This procedure works well except for curve *EF* in Figure 3.3. The details of how curve *EF* is mapped, is explained in Appendix B.

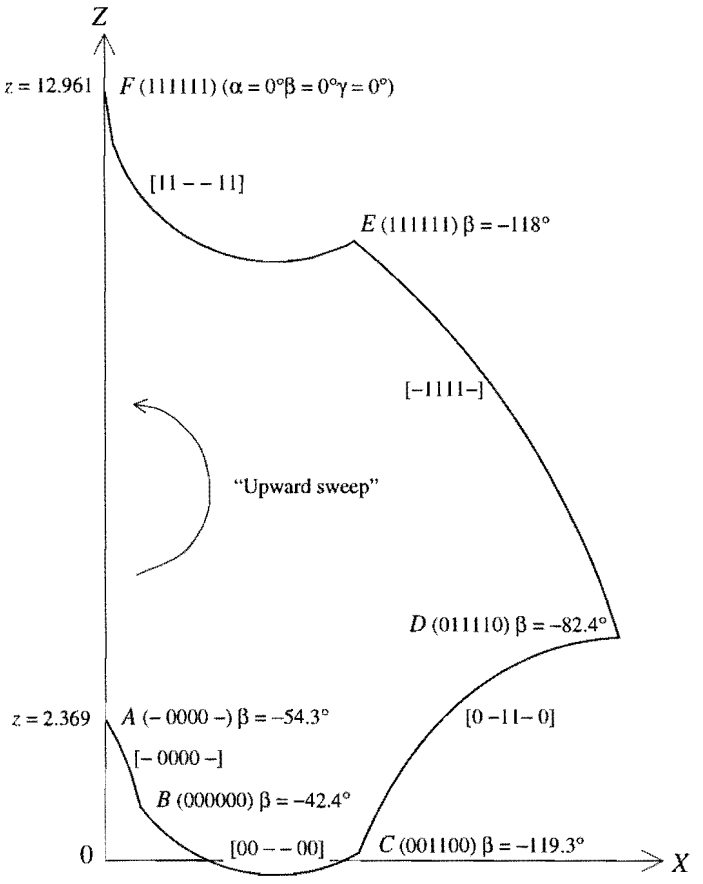

Figure 3.3 "Upward sweep" reachable workspace boundary in the vertical plane through the *0X*-axis.

Using the notation introduced in Chapter 2 and referring to Figure 3.3, the bifurcation points and boundary curves of the vertical plane through the *0X*-axis are labeled in order to differentiate between the two types of reachable boundaries that exist. The curves are now described, with the radiating ray sweeping counter clockwise upwards from the vertical, with relationship (3.15) imposed for successive ray angles φ_j given by (3.16).

The lowest possible position of the working point along the *0Z*-axis is at a height of $z = 2.369$. This is point $A(-\ 0\ \ 0\ \ 0\ \ 0\ -)\,[0^\circ\ \ -54.3^\circ\ \ 0^\circ]$, which clearly is not a bifurcation point where all the actuator legs are at the specific extreme lengths.

Liu et al. [18] report that with all the actuator legs at their minimum lengths and with no platform rotation, the global coordinates of the manipulator working point are $(0,\ 0,\ 2.646)$. Using the proposed notation, this bifurcation point Liu et al. found will be labeled $(0\ \ 0\ \ 0\ \ 0\ \ 0\ \ 0)\ [0^\circ\ \ 0^\circ\ \ 0^\circ]$ The orientation angles of the top platform with the working point coinciding with point $A(-\ 0\ \ 0\ \ 0\ \ 0\ -)$ are: $\alpha = 0^\circ$, $\beta = -54.3^\circ$ and $\gamma = 0^\circ$ as indicated by the notation adopted above.

The fact that β, (which measures the rotation of the top platform about the *0Y*-axis) is the only non-zero orientation angle, indicates that actuator legs 1 and 6 have the same lengths with the working point coinciding with point $A(-\ 0\ \ 0\ \ 0\ \ 0\ -)$.

With the results of the optimization approach, the exact lengths of legs 1 and 6 of point $A(-\ 0\ \ 0\ \ 0\ \ 0\ -)$ are obtained as:

$$l_1 = l_6 = 9.759$$

Considering the above actuator leg lengths, as well as the substantial angle the top platform makes with the *0Y*-axis ($\beta = -54.3^\circ$), it is clear that the upper platform is in a "flipped" orientation at point $A(-\ 0\ \ 0\ \ 0\ \ 0\ -)$. Although this is a mathematically feasible orientation, mechanically it may not be possible due to the actuator legs interfering with each other, and the limited rotations of the joints connecting the legs with the base and moving platform.

Purely mathematically, the working point of the "flipped" top platform advances along boundary curve $AB[-\ 0\ \ 0\ \ 0\ \ 0\ -]$ until it reaches bifurcation point $B\ (0\ \ 0\ \ 0\ \ 0\ \ 0\ \ 0)$, where all the actuator legs take on their minimum lengths, and the orientation angles of the top platform are: $\alpha = 0^\circ$, $\beta = -42.4^\circ$ and $\gamma = 0^\circ$.

The top platform remains in its flipped orientation as the working point advances from bifurcation point $B\ (0\ \ 0\ \ 0\ \ 0\ \ 0\ \ 0)$ along curves $BC[0\ \ 0\ -\ -\ 0\ \ 0]$, $CD[0\ -\ 1\ \ 1\ -\ 0]$ and $DE[-\ 1\ \ 1\ \ 1\ \ 1\ -]$. It is interesting to note that the extreme bifurcation points $B\ (0\ \ 0\ \ 0\ \ 0\ \ 0\ \ 0)$, and $E\ (1\ \ 1\ \ 1\ \ 1\ \ 1\ \ 1)$ are asymmetrically placed off the *0Z*-axis. With the manipulator working point coinciding with bifurcation point $E\ (1\ \ 1\ \ 1\ \ 1\ \ 1\ \ 1)$, the top platform is in an extreme flipped orientation ($\alpha = 0^\circ$, $\beta = -118^\circ$ and $\gamma = 0^\circ$), which explains the existence of curve $EF\ [1\ \ 1\ -\ -\ 1\ \ 1]$. Starting in the flipped orientation ($\beta = -118^\circ$) at bifurcation point $E\ (1\ \ 1\ \ 1\ \ 1\ \ 1\ \ 1)$, curve *EF* denotes the path along which actuator legs 3 and 4 are retracted until the top platform is out of this flipped configuration. Actuator legs 3 and 4 are then extended again as the working point advances along the rest of the curve $EF\ [1\ \ 1\ -\ -\ 1\ \ 1]$ and eventually reaches bifurcation point $F\ (1\ \ 1\ \ 1\ \ 1\ \ 1\ \ 1)$ where the top platform is horizontally orientated ($\alpha = 0^\circ$, $\beta = 0^\circ$ and $\gamma = 0^\circ$). This completes the upward sweep of the radiating ray.

Point F $(1 \quad 1 \quad 1 \quad 1 \quad 1 \quad 1)$ is at a height of $z = 12.961$ which corresponds to Liu et al.'s [18] reported global coordinates of the manipulator working point $(0,\ 0,\ 12.96)$, when all the actuator legs are at their maximum lengths.

Following the upward sweep the mapping may be continued by initiating a subsequent downward sweep. It follows that equation (3.14) can be changed so that the rays for any specific vertical plane are incremented starting with the initial ray parallel to the *positive* Z-direction and incrementing φ_j through 180° ending with the final ray parallel to the *negative* Z-direction. Constraint equation (3.14) now becomes:

$$\sqrt{x_j^2 + y_j^2} - (z_j - z^0)\tan(\varphi_j) = 0 \tag{3.17}$$

Which can once again be rewritten in terms of the generalized coordinates to give:

$$\sqrt{u_{1j}^2 + u_{2j}^2} - (u_{3j} - z^0)\tan(\varphi_j) = 0 \tag{3.18}$$

The reachable workspace in the vertical plane through the *0X*-axis is now re-mapped using equality (3.18) instead of (3.15), and incrementing φ_j as given by expression (3.16), resulting in a downward sweep of the radiating ray.

Here again the maximum displacements of the respective rays $j = 1, 2, \ldots, N_R$ are found using as starting point for the successive optimizations, the solution for the previous ray, $j = 0, 1, 2, \ldots, (N_R - 1)$.

Figure 3.4 shows the re-mapped reachable workspace boundary in the vertical plane through the *0X*-axis ($\theta_i = 0^\circ$). Starting from bifurcation point F $(1 \quad 1 \quad 1 \quad 1 \quad 1 \quad 1)$ where the top platform is horizontally orientated ($\alpha = 0^\circ$, $\beta = 0^\circ$ and $\gamma = 0^\circ$), the working point advances along the curve *FG* $[- \quad 1 \quad 1 \quad 1 \quad 1 \quad -]$ as the platform moves away from the *0Z*-axis. Although curve *FG* $[- \quad 1 \quad 1 \quad 1 \quad 1 \quad -]$ in Figure 3.4 carries the same label as curve *DE* $[- \quad 1 \quad 1 \quad 1 \quad 1 \quad -]$ in Figure 3.3, the two boundary curves do not coincide as is evident from the earlier composite Figure 3.2. The reason for this is that the top platform is now positively tilted as the working point advances along curve *FG* $[- \quad 1 \quad 1 \quad 1 \quad 1 \quad -]$ in Figure 3.4, while the top platform is in a negatively flipped orientation as the working point advances along curve *DE* $[- \quad 1 \quad 1 \quad 1 \quad 1 \quad -]$ in Figure 3.3. The positively tilted orientation of the top platform is $\alpha = 0^\circ$, $\beta = 31.9^\circ$ and $\gamma = 0^\circ$ when the manipulator working point coincides with bifurcation point G $(0 \quad 1 \quad 1 \quad 1 \quad 1 \quad 0)$ in Figure 3.4.

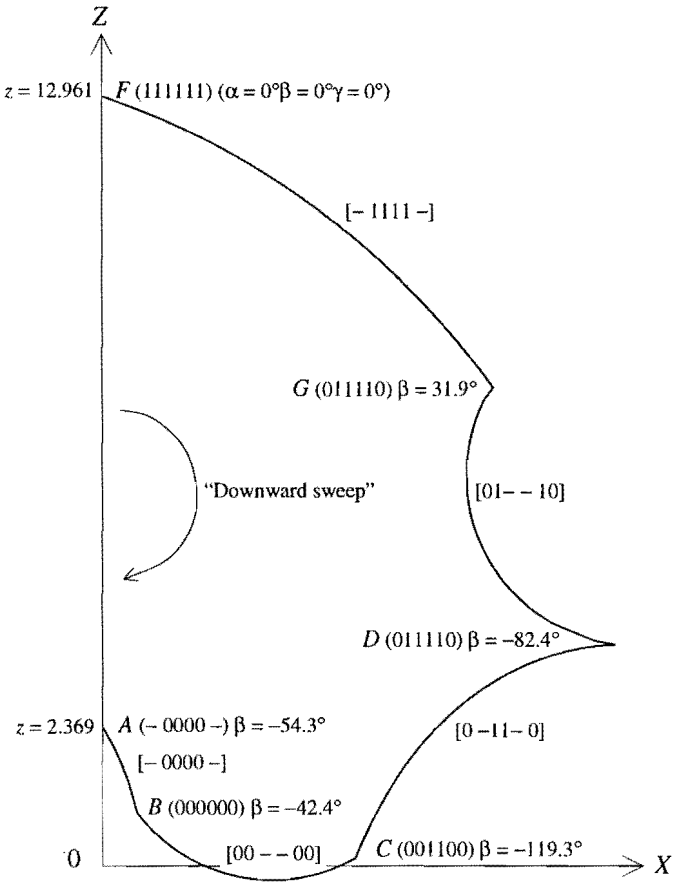

Figure 3.4 "Downward sweep" reachable workspace boundary in the vertical plane through the *0X*-axis $(\theta = 0^\circ)$.

The "downward sweep" re-mapped reachable boundary in Figure 3.4 shows a boundary curve *GD* $[0\ \ 1\ \ -\ \ -\ \ 1\ \ 0]$ between bifurcation points $G(0\ \ 1\ \ 1\ \ 1\ \ 1\ \ 0)$ and $D(0\ \ 1\ \ 1\ \ 1\ \ 1\ \ 0)$. The behavior along curve *GD* $[0\ \ 1\ \ -\ \ -\ \ 1\ \ 0]$ in Figure 3.4 is similar to that along curve *EF* $[1\ \ 1\ \ -\ \ -\ \ 1\ \ 1]$ in Figure 3.3. Starting at bifurcation point $G(0\ \ 1\ \ 1\ \ 1\ \ 1\ \ 0)$, actuator legs 3 and 4 are retracted as the manipulator working point advances along the first portion of curve *GD* $[0\ \ 1\ \ -\ \ -\ \ 1\ \ 0]$. This action forces the top platform from the positively tilted orientation at bifurcation point $G(0\ \ 1\ \ 1\ \ 1\ \ 1\ \ 0)$ $(\alpha = 0^\circ,\ \beta = 31.9^\circ$ and $\gamma = 0^\circ)$, into the negatively flipped orientation $(\alpha = 0^\circ,\ \beta = -82.36^\circ$ and $\gamma = 0^\circ)$ with the manipulator working point coinciding with bifurcation point $D\ (0\ \ 1\ \ 1\ \ 1\ \ 1\ \ 0)$. The manipulator working point follows the last portion of curve *GD* $[0\ \ 1\ \ -\ \ -\ \ 1\ \ 0]$ as actuator legs 3 and 4 are extended, so that these legs take on their maximum leg lengths when bifurcation point $D\ (0\ \ 1\ \ 1\ \ 1\ \ 1\ \ 0)$ is reached.

Comparing Figure 3.3 with Figure 3.4 shows, as is also apparent from the composite Figure 3.2, that the bottom portion of the mapped reachable boundary is the same independent of whether the upward sweep or downward sweep mapping is done.

Looking at the results obtained, it is evident that the reachable workspace is characterized by different boundary curves corresponding to different types of orientations of the top platform. More specifically, analyzing the reachable boundary in the vertical plane through the *0X*-axis, shows that the negatively flipped orientation is *not* mechanically feasible at all positions where the mathematical solution exists.

Although the computation of the workspace was restricted here to the plane through the *0X*-axis ($\theta = 0^{\circ}$), it may be done in a straight forward similar manner for any other vertical plane through *0Z*, i.e. for any other θ value.

The demonstration of the successful mapping of the workspace in the vertical plane through the *0X*-axis proves that the optimization approach adopted here is a tool with which the mathematically complete reachable workspace can be mapped. The mapping of such a complete workspace is of course of limited practical use if it encloses mechanically infeasible regions. However, if the spherical and gimbal joint limits are taken into consideration, and the actuator legs are prohibited to interfere while mapping the reachable workspace, the complete workspace will be mechanically feasible and of practical value. These aspects will be addressed in the future research envisaged and is also discussed in more detail in Chapter 5.

In the next chapter the complete fixed orientation workspace $A[\alpha_{fix}, \beta_{fix}, \gamma_{fix}]$, with boundary $\partial A[\alpha_{fix}, \beta_{fix}, \gamma_{fix}]$, as well as an example of a complete dextrous workspace $A[\alpha_{fix}, \beta_{fix}, \gamma_{min} - \gamma_{max}]$, with boundary $\partial A[\alpha_{fix}, \beta_{fix}, \gamma_{min} - \gamma_{max}]$ are determined.

Chapter 4

4 DETERMINATION OF THE DEXTROUS WORKSPACE OF THE 6–3 STEWART PLATFORM

4.1 INTRODUCTION

It is of particular importance to be able to compute the fixed orientation and dextrous workspaces of a spatial parallel manipulator. Merlet [4] states that in contrast to common serial link mechanisms with three intersecting wrist joint axes, the (orientationally unconstrained reachable) workspace of a (spatial) parallel manipulator cannot be decoupled in two three-dimensional workspaces characterizing the possible translational and orientational motions. The fixed orientation and dextrous workspaces are however useful projections of the reachable workspace that can easily be presented in a human readable way.

The study of the different workspaces of the 6–3 Stewart platform is continued in this chapter with the objective of determining typical dextrous workspace of practical importance.

The dextrous workspace of the planar Stewart platform is defined in Section 2.6.4.1. The corresponding dexterity requirements for the 6–3 Stewart platform is stated in terms of ranges of rotatability of the orientation angles. In general these dexterity requirements may be specified by the triplet:

$$[\alpha_{min} - \alpha_{max}\,,\ \beta_{min} - \beta_{max}\,,\ \gamma_{min} - \gamma_{max}] \tag{4.1}$$

which indicates that the orientation angles α, β and γ must be able to assume *all* values in the respective ranges $[\alpha_{min} - \alpha_{max}]$, $[\beta_{min} - \beta_{max}]$ and $[\gamma_{min} - \gamma_{max}]$ at *any* point in the associated dextrous workspace denoted by $\boldsymbol{A}[\alpha_{min} - \alpha_{max}\,,\ \beta_{min} - \beta_{max}\,,\ \gamma_{min} - \gamma_{max}]$. This is an extension of, and in agreement with, the notation proposed for the planar case.

For the purpose of this study, the general dexterity requirement (4.1) is restricted to:

$$[\alpha_{fix}\,,\ \beta_{fix}\,,\ \gamma_{min} - \gamma_{max}] \tag{4.2}$$

indicating that only γ must be able to assume *all* values in the range $[\gamma_{min} - \gamma_{max}]$, while α and β must respectively assume the fixed values α_{fix} and β_{fix} at *any* point in the associated dextrous workspace denoted by $\boldsymbol{A}[\alpha_{fix}, \beta_{fix}, \gamma_{min} - \gamma_{max}]$.

4.2 Fixed Orientation Accessible Workspace of the 6–3 Stewart Platform

It was shown in Section 2.6.4.4 that two fixed orientation accessible workspaces may be used to determine the planar dextrous workspace. The same procedure is proposed here for the spatial case, and therefore it is important to be able to determine any specified fixed orientation accessible workspace.

Any fixed orientation requirement for the 6 – 3 Stewart platform, i.e. $[\alpha_{fix}, \beta_{fix}, \gamma_{fix}]$ implies three equalities:

$$\alpha = \alpha_{fix}, \ \beta = \beta_{fix} \ \text{and} \ \gamma = \gamma_{fix} \tag{4.3}$$

These three equality constraints (4.3) correspond to the single equality prescribed for the planar Stewart platform (2.27), and here fix the intermediate coordinates of the 6–3 Stewart platform, i.e.:

$$\mathbf{w} = \begin{bmatrix} w_1 \\ w_2 \\ w_3 \end{bmatrix} = \begin{bmatrix} w_{1\,fix} \\ w_{2\,fix} \\ w_{3\,fix} \end{bmatrix} = \mathbf{w}_{fix} \tag{4.4}$$

Here vertical planes will be used (see Section 3.4.1) to map the fixed orientation accessible workspace of the 6–3 Stewart platform.

Apart from the three equalities fixing the intermediate coordinates (4.4), two additional equalities are needed to specify the search direction of each ray in its associated vertical plane. Equality (3.11) defines the orientation of each vertical plane, and depending on whether the plane is to be mapped starting at the lowest possible or highest possible position of the working point, equality (3.15) or equality (3.18) respectively fixes the direction of the ray in the vertical plane.

Thus the "fixed orientation" accessible workspace in vertical plane i, $(i = 0, 1, 2, ..., N_p)$, making an angle θ_i with the *0X*-axis, may be mapped by solving *modified* optimization problem (i) (see Section 2.6.4.2) for j successive rays $(j = 0, 1, 2, ..., N_R)$. These successive rays emanate from $\mathbf{u}^0$ (3.13) at angular intervals δ. In *modified* optimization problem (i), $\mathbf{h}(\mathbf{u}, \mathbf{s}) = \mathbf{0}$ is given by (3.11) and either (3.15) *or* (3.18), and $\mathbf{w} = \mathbf{w}_{fix}$ is given by (4.4).

4.2.1 Results of the Fixed Orientation Accessible Workspace of the 6–3 Stewart Platform

Corresponding to the horizontally fixed orientation accessible workspace $A[0^\circ]$, that was determined for the planar Stewart platform in Section 2.6.4.3, the "horizontally" fixed orientation accessible workspace $A[0^\circ, 0^\circ, 0^\circ]$ of the 6–3 Stewart platform is mapped here. Figure 4.1 shows the upper and lower isometric views of the boundary $\partial A[0^\circ, 0^\circ, 0^\circ]$ of the three-dimensional fixed orientation accessible workspace $A[0^\circ, 0^\circ, 0^\circ]$ of the 6–3 Stewart platform.

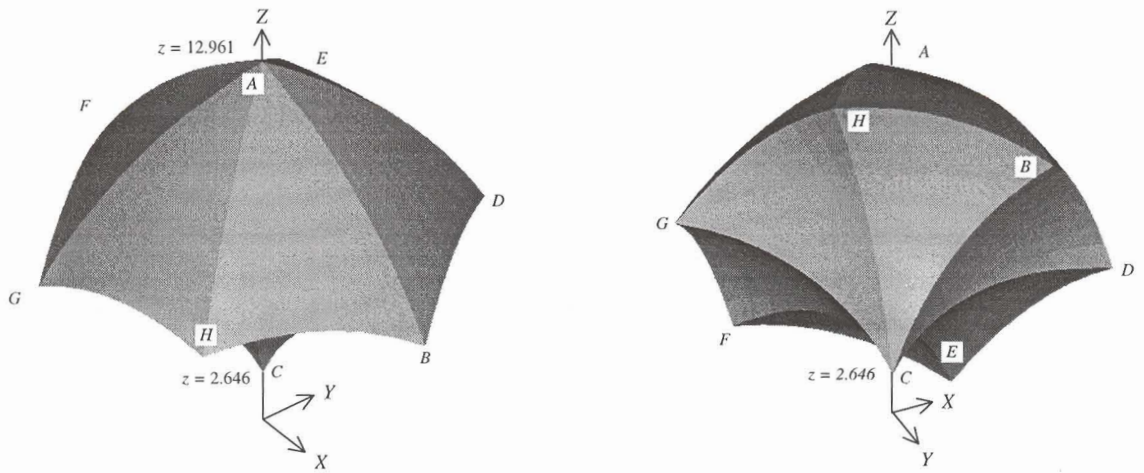

Figure 4.1 Isometric view of the three-dimensional fixed orientation accessible workspace $A[0^\circ, 0^\circ, 0^\circ]$.

The boundary surfaces of $A[0^\circ, 0^\circ, 0^\circ]$ are unique and are independent of whether the vertical planes, used for mapping the workspace, are traced by sweeping from the lowest possible or highest possible working point position.

Note that the lowest possible point ($z = 2.646$) and the highest possible point ($z = 12.961$) on the boundary $\partial A[0^\circ, 0^\circ, 0^\circ]$ and on the *0Z*-axis correspond exactly to the reported (Liu et al. [18]) global coordinates of the working point when all the actuator legs respectively take on their minimum and maximum lengths.

Also note the three fold symmetry of the workspace $A[0^\circ, 0^\circ, 0^\circ]$ about the *0Z*-axis where each third of the workspace spans 120°, and consists of two convex boundary surfaces comprising the upper portion of $A[0^\circ, 0^\circ, 0^\circ]$, and two concave boundary surfaces comprising the lower portion of $A[0^\circ, 0^\circ, 0^\circ]$.

There are also definite bifurcation lines present where the boundary surfaces intersect each other. The vertical bifurcation lines are spaced at 60° rotation intervals, and there are curved "horizontal"

bifurcation lines at the intersection of the upper convex and lower concave boundary surfaces. The previously proposed labeling notation (see Sections 2.5.3 and 2.6.3) is applied to label the fixed orientation accessible workspace $A[0^\circ, 0^\circ, 0^\circ]$.

The proposed optimization approach may be used to map and label the fixed orientation accessible boundary $\partial A[0^\circ, 0^\circ, 0^\circ]$ in any isolated vertical plane i making an angle θ_i with the $0X$-axis. The results for three planes of particular interest, are depicted in Figure 4.2 (a), (b) & (c) for the respective cases: (a) $\partial A[0^\circ, 0^\circ, 0^\circ][\theta_i = 0^\circ]$, (b) $\partial A[0^\circ, 0^\circ, 0^\circ][\theta_i = 30^\circ]$ and (c) $\partial A[0^\circ, 0^\circ, 0^\circ][\theta_i = 60^\circ]$.

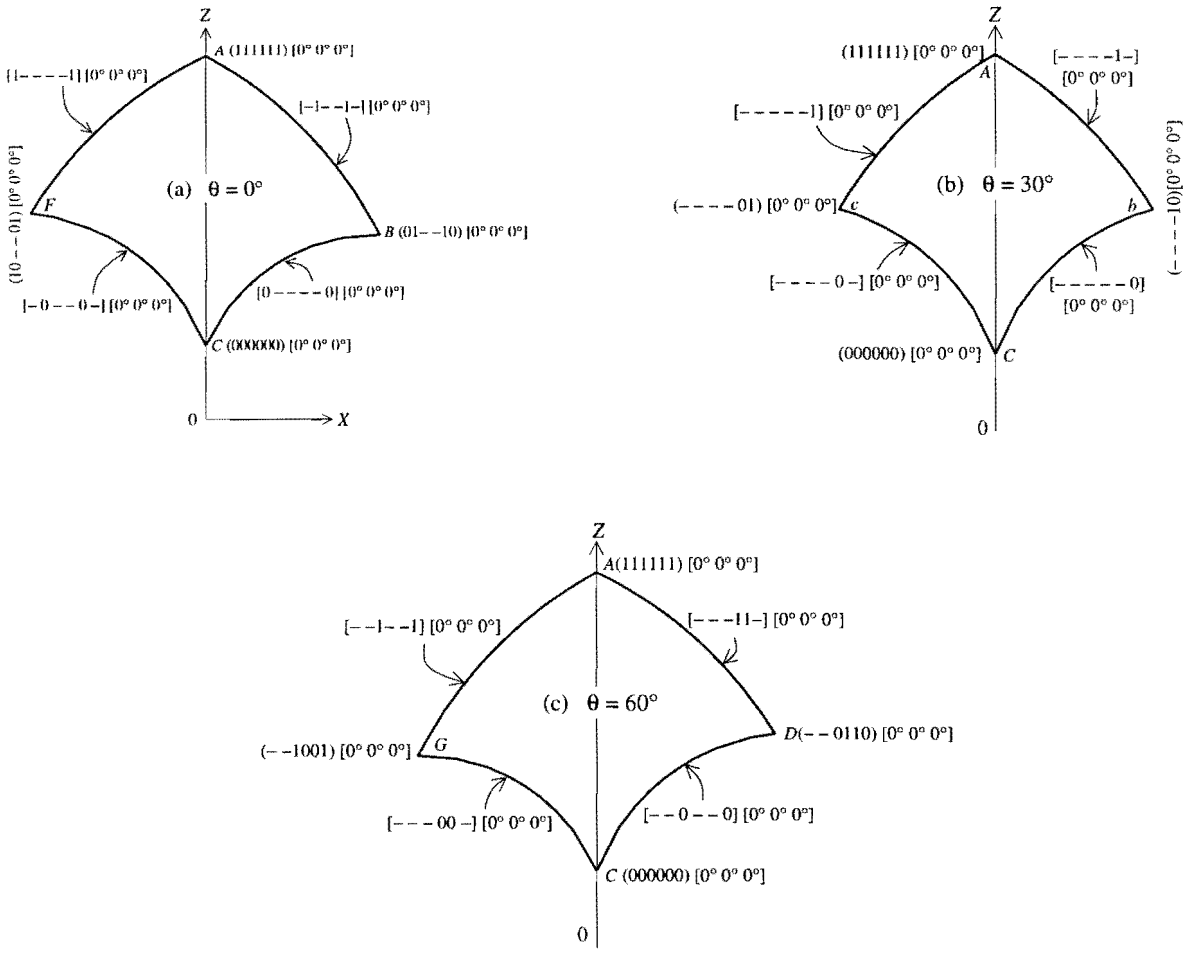

Figure 4.2 $\partial A[0^\circ, 0^\circ, 0^\circ]$ for (a) $\theta_i = 0^\circ$, (b) $\theta_i = 30^\circ$ and (c) $\theta_i = 60^\circ$.

These three vertical sections may be used to describe the behavior of the 6–3 Stewart platform for the working point coinciding with any point on the boundary surfaces defined by the vertices A, B, C and D, as well as the vertices A, F, G and C (see Figure 4.1).

Consider the vertical section through the *0X*-axis at $\theta_i = 0^\circ$, shown in Figure 4.2 (a) together with the related coplanar vertical section *AFC* at $\theta_i = 180^\circ$. It is clear that the lowest possible position of the manipulator working point in $A\,[0^\circ, 0^\circ, 0^\circ]$ is bifurcation point C $(0\ 0\ 0\ 0\ 0\ 0)\ [0^\circ, 0^\circ, 0^\circ]$ where all the actuator legs are at their minimum lengths.

The manipulator working point will follow bifurcation line *CB* $[0 - - - - 0]\ [0^\circ, 0^\circ, 0^\circ]$ as it moves away from its lowest possible position and maintains the fixed orientation $\alpha = 0^\circ, \beta = 0^\circ$ and $\gamma = 0^\circ$. Actuator legs 1 and 6 remain fixed at their minimum lengths while actuator legs 2, 3, 4 and 5 vary. Similarly, bifurcation line *BA* $[- 1 - - 1 -]\ [0^\circ, 0^\circ, 0^\circ]$ represents the path of the manipulator working point with actuator legs 2 and 5 fixed at their maximum lengths, and legs 1, 3, 4 and 6 varying.

Bifurcation point *B* $(0\ 1 - - 1\ 0)\ [0^\circ, 0^\circ, 0^\circ]$ coinciding with the intersection of bifurcation lines *CB* $[0 - - - - 0]\ [0^\circ, 0^\circ, 0^\circ]$ and *BA* $[- 1 - - 1 -]\ [0^\circ, 0^\circ, 0^\circ]$ is the position of the working point if actuator legs 1 and 6 are fixed at their minimum lengths, legs 2 and 5 at their maximum lengths and the top platform fixed in a horizontal orientation (4.4).

Bifurcation point *B* $(0\ 1 - - 1\ 0)\ [0^\circ, 0^\circ, 0^\circ]$ is found by minimizing an error function similar to (2.24) defined in Section 2.6.3.1. Details of the procedure is described in Appendix C.

Finally bifurcation point *A* $(1\ 1\ 1\ 1\ 1\ 1)\ [0^\circ, 0^\circ, 0^\circ]$ is the highest point in the fixed orientation accessible workspace $A\,[0^\circ, 0^\circ, 0^\circ]$, indicating the position of the working point if all the actuator legs at their maximum lengths.

The vertical section at $\theta_i = 180^\circ$ is also shown in Figure 4.2 (a) and is labeled in a similar manner.

Figure 4.2 (b) shows the section of the fixed orientation accessible boundary $\partial A\,[0^\circ, 0^\circ, 0^\circ]$ at $\theta_i = 30^\circ$ (curve *AbC*) and at $\theta_i = 210^\circ$ (curve *AcC*). The concave curve *Cb* $[- - - - - 0]\ [0^\circ, 0^\circ, 0^\circ]\,[\theta_i = 30^\circ]$ is the boundary path of the manipulator working point with leg 6 fixed at its minimum length and the remaining legs varying.

The single leg fixed at its extreme length is due to the fact that *modified* optimization problem (i), specified in terms of the six output and intermediate coordinates, has five equalities defined in Section 4.2. The five equalities comprise of the three equalities given by equation (4.4) and the two additional

equalities needed to specify the search direction of each ray in its associated vertical plane. The displacement from the radiating point $\mathbf{u}^0$ is therefore maximized until the first actuator leg reaches an extreme length resulting in a boundary point on any of the 12 boundary surfaces enclosing the fixed orientation accessible workspace $A\,[0^\circ,\ 0^\circ,\ 0^\circ]$.

Curve *bA* $[-\ -\ -\ -\ 1\ -]\ [0^\circ,\ 0^\circ,\ 0^\circ]\,[\theta_i = 30^\circ]$ carries a similar label. Boundary surfaces *ABD* and *BCD* (see Figure 4.1) may therefore respectively be labeled as *ABD* $[-\ -\ -\ -\ 1\ -]\ [0^\circ,\ 0^\circ,\ 0^\circ]$ and *BCD* $[-\ -\ -\ -\ -\ 0]\ [0^\circ,\ 0^\circ,\ 0^\circ]$.

The above also explains why a bifurcation or intersecting line exists where two bounding surfaces on $\partial A\,[0^\circ,\ 0^\circ,\ 0^\circ]$ intersect. Along this line two actuator legs remain fixed at their extreme values. Similarly the number of legs assuming extreme lengths at any bifurcation point is dependent on the different kinds of boundary surfaces intersecting at the specific bifurcation point.

It is interesting to note that the convex vertical bifurcation lines and convex boundary surfaces are associated with maximum extreme leg lengths, and the concave ones with minimum extreme leg lengths.

A final aspect of interest concerning the fixed orientation accessible workspace $A\,[0^\circ,\ 0^\circ,\ 0^\circ]$ is the bifurcation line *BD* $[-\ -\ -\ -\ 1\ 0]\ [0^\circ,\ 0^\circ,\ 0^\circ]$. The label of this bifurcation line corresponds to the label of point $b\ (-\ -\ -\ -\ 1\ 0)\ [0^\circ,\ 0^\circ,\ 0^\circ]\,[\theta_i = 30^\circ]$ in Figure 4.2 (b). At point $b\ (-\ -\ -\ -\ 1\ 0)\ [0^\circ,\ 0^\circ,\ 0^\circ]\,[\theta_i = 30^\circ]$ six constraints are active, namely the direction of the vertical plane (3.11), the two actuator legs assuming extreme lengths and the three orientation angles (4.4). Point *b* may accordingly be solved for by minimizing the following error function using *LFOPCV3*:

$$\begin{aligned} e(\mathbf{u},\mathbf{w}) = &\left(v_5(\mathbf{u},\mathbf{w}) - v_5^{max}\right)^2 + \left(v_6(\mathbf{u},\mathbf{w}) - v_6^{min}\right)^2 + \left(u_2 - u_1\tan(\theta)\right)^2 \\ &+ (w_1 - 0)^2 + (w_2 - 0)^2 + (w_3 - 0)^2 \end{aligned} \tag{4.5}$$

The labeled bifurcation points, bifurcation lines and boundary surfaces comprising the fixed orientation accessible boundary $\partial A\,[0^\circ,\ 0^\circ,\ 0^\circ]$ shown in Figure 4.1 are:

Bifurcation points:

$A\ (1\ 1\ 1\ 1\ 1\ 1)\ [0^\circ,\ 0^\circ,\ 0^\circ]$ $B\ (0\ 1\ -\ -\ 1\ 0)\ [0^\circ,\ 0^\circ,\ 0^\circ]$ $C\ (0\ 0\ 0\ 0\ 0\ 0)\ [0^\circ,\ 0^\circ,\ 0^\circ]$

$D\ (-\ -\ 0\ 1\ 1\ 0)\ [0^\circ,\ 0^\circ,\ 0^\circ]$ $E\ (1\ 0\ 0\ 1\ -\ -)\ [0^\circ,\ 0^\circ,\ 0^\circ]$ $F\ (1\ 0\ -\ -\ 0\ 1)\ [0^\circ,\ 0^\circ,\ 0^\circ]$

$G\ (-\ -\ 1\ 0\ 0\ 1)\ [0^\circ,\ 0^\circ,\ 0^\circ]$ $H\ (0\ 1\ 1\ 0\ -\ -)\ [0^\circ,\ 0^\circ,\ 0^\circ]$

Bifurcation lines (upper convex):

AB [– 1 – – 1 –] [0°, 0°, 0°] AD [– – – 1 1 –] [0°, 0°, 0°] AE [1 – – 1 – –] [0°, 0°, 0°]

AF [1 – – – – 1] [0°, 0°, 0°] AG [– – 1 – – 1] [0°, 0°, 0°] AH [– 1 1 – – –] [0°, 0°, 0°]

Bifurcation lines (lower concave):

CB [0 – – – – 0] [0°, 0°, 0°] CD [– – 0 – – 0] [0°, 0°, 0°] CE [– 0 0 – – –] [0°, 0°, 0°]

CF [– 0 – – 0 –] [0°, 0°, 0°] CG [– – – 0 0 –] [0°, 0°, 0°] CH [0 – – 0 – –] [0°, 0°, 0°]

Bifurcation lines (horizontally orientated):

BD [– – – – 1 0] [0°, 0°, 0°] DE [– – 0 1 – –] [0°, 0°, 0°] EF [1 0 – – – –] [0°, 0°, 0°]

FG [– – – – 0 1] [0°, 0°, 0°] GH [– – 1 0 – –] [0°, 0°, 0°] HB [0 1 – – – –] [0°, 0°, 0°]

Boundary surfaces (upper convex):

ABD [– – – – 1 –] [0°, 0°, 0°] ADE [– – – 1 – –] [0°, 0°, 0°] AEF [1 – – – – –] [0°, 0°, 0°]

AFG [– – – – – 1] [0°, 0°, 0°] AGH [– – 1 – – –] [0°, 0°, 0°] AHB [– 1 – – – –] [0°, 0°, 0°]

Boundary surfaces (lower concave):

CBD [– – – – – 0] [0°, 0°, 0°] CDE [– – 0 – – –] [0°, 0°, 0°] CEF [– 0 – – – –] [0°, 0°, 0°]

CFG [– – – – 0 –] [0°, 0°, 0°] CGH [– – – 0 – –] [0°, 0°, 0°] CHB [0 – – – – –] [0°, 0°, 0°]

4.3 THE COMPUTATION OF A SPECIFIC SPATIAL DEXTROUS WORKSPACE

The specific dextrous workspace of the 6–3 Stewart platform considered here has the restricted dexterity requirement (4.2):

$$[0^\circ,\ 0^\circ,\ (-30^\circ)-(30^\circ)] \tag{4.6}$$

Here, in accordance with the treatment for the planar case (Section 2.6.4.4), two spatial fixed orientation accessible workspaces, $\boldsymbol{A}[0^\circ,\ 0^\circ,\ -30^\circ]$ and $\boldsymbol{A}[0^\circ,\ 0^\circ,\ 30^\circ]$ are determined. The intersecting or overlapping volume is assumed to be the dextrous workspace $\boldsymbol{A}[0^\circ,\ 0^\circ,\ (-30^\circ)-(30^\circ)]$, within which the full dexterity requirement (4.6) is met at each point enclosed by $\partial\boldsymbol{A}[0^\circ,\ 0^\circ,\ (-30^\circ)-(30^\circ)]$.

Figure 4.3 shows the fixed orientation accessible workspace $A[0^\circ, 0^\circ, -30^\circ]$ with boundary $\partial A[0^\circ, 0^\circ, -30^\circ]$. Note that the highest point in Figure 4.3 is at $z = 10.82$, and the lowest point is at $z = 6.535$.

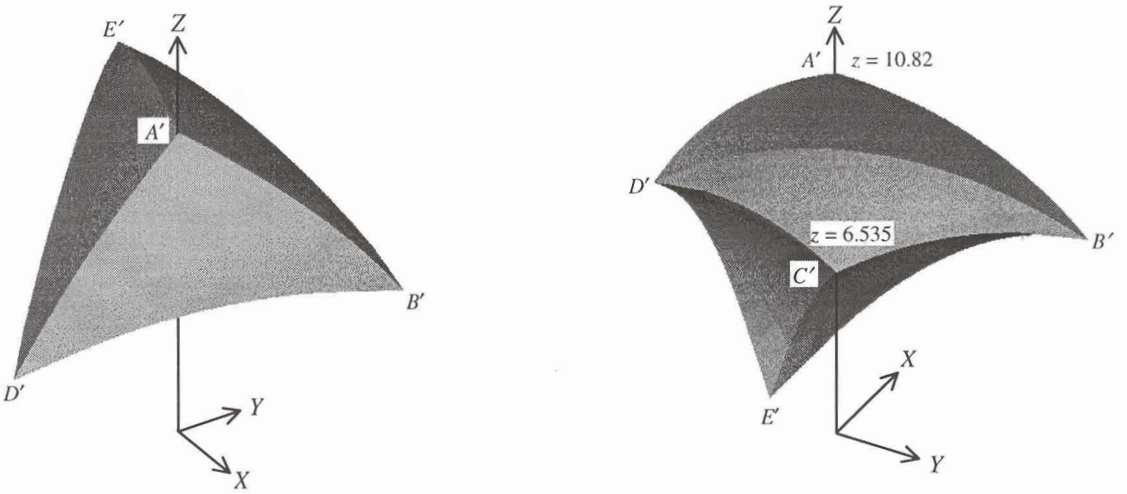

Figure 4.3 Fixed orientation accessible workspace boundary $\partial A[0^\circ, 0^\circ, -30^\circ]$.

The boundary $\partial A[0^\circ, 0^\circ, -30^\circ]$in Figure 4.3 is labeled according to the convention described in Section 4.2.1:

Bifurcation points:

A' (– 1 – 1 – 1) $[0^\circ, 0^\circ, -30^\circ]$ B' (0 1 0 1 – –) $[0^\circ, 0^\circ, -30^\circ]$

C' (0 – 0 – 0 –) $[0^\circ, 0^\circ, -30^\circ]$ D' (0 1 – – 0 1) $[0^\circ, 0^\circ, -30^\circ]$

E' (– – 0 1 0 1) $[0^\circ, 0^\circ, -30^\circ]$

Bifurcation lines (upper convex):

$A'B'$ [– 1 – 1 – –] $[0^\circ, 0^\circ, -30^\circ]$ $A'D'$ [– 1 – – – 1] $[0^\circ, 0^\circ, -30^\circ]$

$A'E'$ [– – – 1 – 1] $[0^\circ, 0^\circ, -30^\circ]$

Bifurcation lines (lower concave):

$C'B'$ [0 – 0 – – –] $[0^\circ, 0^\circ, -30^\circ]$ $C'D'$ [0 – – – 0 –] $[0^\circ, 0^\circ, -30^\circ]$

$C'E'$ [– – 0 – 0 –] $[0^\circ, 0^\circ, -30^\circ]$

Bifurcation lines (horizontally orientated):

$B'D'$ [0 1 – – – –] $[0^\circ, 0^\circ, -30^\circ]$ $D'E'$ [– – – – 0 1] $[0^\circ, 0^\circ, -30^\circ]$

$E'B'$ [– – 0 1 – –] $[0^\circ, 0^\circ, -30^\circ]$

Boundary surfaces (upper convex):

$$A'B'D' \; [-\,1\,-\,-\,-\,-] \; [0^\circ,\, 0^\circ,\, -30^\circ] \quad A'D'E' \; [-\,-\,-\,-\,-\,1] \; [0^\circ,\, 0^\circ,\, -30^\circ]$$

$$A'E'B' \; [-\,-\,-\,1\,-\,-] \; [0^\circ,\, 0^\circ,\, -30^\circ]$$

Boundary surfaces (lower concave):

$$C'B'D' \; [0\,-\,-\,-\,-\,-] \; [0^\circ,\, 0^\circ,\, -30^\circ] \quad C'D'E' \; [-\,-\,-\,0\,-] \; [0^\circ,\, 0^\circ,\, -30^\circ]$$

$$C'E'B' \; [-\,-\,0\,-\,-\,-] \; [0^\circ,\, 0^\circ,\, -30^\circ]$$

The spatial workspace $A\,[0^\circ,\, 0^\circ,\, -30^\circ]$ retains the three-fold symmetry, and possesses three convex and three concave boundary surfaces along the upper and lower portions of the fixed orientation accessible boundary $\partial A\,[0^\circ,\, 0^\circ,\, -30^\circ]$.

The three vertically mapped bifurcation lines formed by the three pairs of intersecting boundary surfaces (convex and concave), are in actual fact no longer perfectly vertical because of the 30° rotation. The exact analyses and determination of the typical non-vertical bifurcation curve $A'B'C'$ is presented in Appendix D.

Keeping in mind that the aim here is to determine the dextrous workspace $A\,[0^\circ,\, 0^\circ,\, (-30^\circ)-(30^\circ)]$, it is required to determine the intersection of the fixed orientation workspace $A\,[0^\circ,\, 0^\circ,\, 30^\circ]$ (Volume $A'C'F'G'H'$ shown in Figure 4.4) with the fixed orientation workspace $A\,[0^\circ,\, 0^\circ,\, -30^\circ]$ (Volume $A'B'C'D'E'$ shown in Figure 4.3 and Figure 4.4). These two fixed orientation accessible workspaces overlap each other as shown in Figure 4.4 and their intersection is taken as the dexterous workspace of interest, namely $A\,[0^\circ,\, 0^\circ,\, (-30^\circ)-(30^\circ)]$ corresponding to Volume $A'C'I'J'K'L'M'N'$.

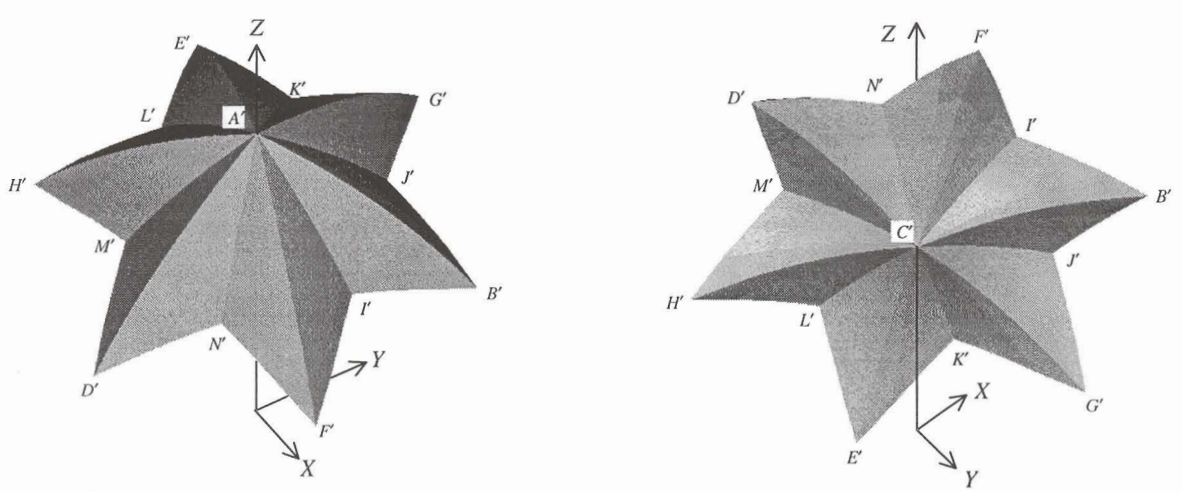

Figure 4.4 Overlap of fixed orientation accessible workspaces $A\,[0^\circ,\, 0^\circ,\, -30^\circ]$ and $A\,[0^\circ,\, 0^\circ,\, 30^\circ]$.

The dextrous workspace found by the intersection of $\boldsymbol{A}\left[0^\circ,\ 0^\circ,\ -30^\circ\right]$ and $\boldsymbol{A}\left[0^\circ,\ 0^\circ,\ 30^\circ\right]$ is depicted in Figure 4.5

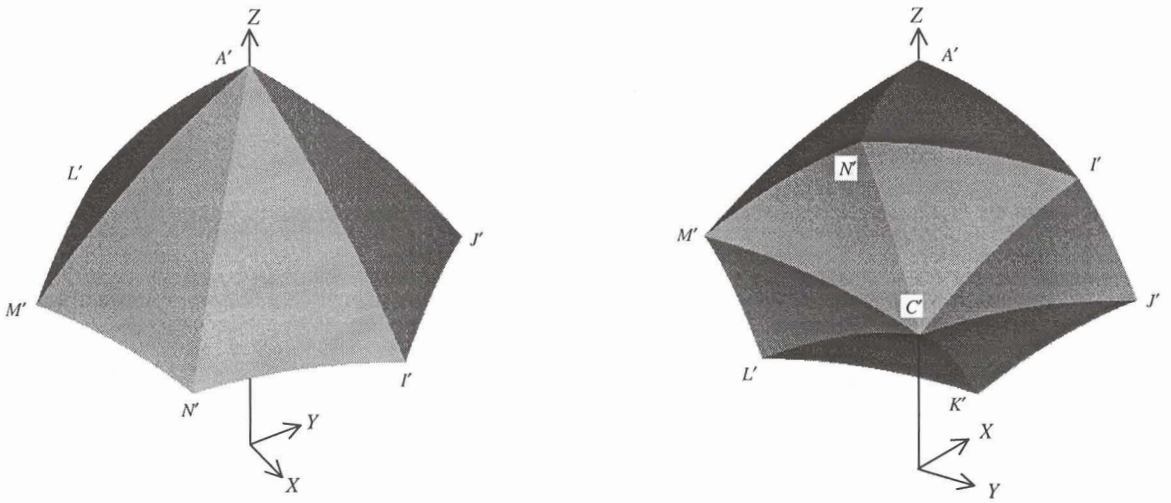

Figure 4.5 The dextrous workspace $\boldsymbol{A}\left[0^\circ,\ 0^\circ,\ (-30^\circ)-(30^\circ)\right]$.

The dextrous workspace is also characterized by the three-fold symmetry about the *0Z*-axis. It is bounded by and consists out of six pairs (convex and concave) of dextrous surfaces separated by six dextrous curves $A'I'C'$, $A'J'C'$, $A'K'C'$, $A'L'C'$, $A'M'C'$ and $A'N'C'$ spaced at 60° intervals. The six dextrous curves are all accurately mapped and carry the same label $\left[0^\circ,\ 0^\circ,\ (-30^\circ)-(30^\circ)\right]$ indicating that the full dexterity requirement is met along these curves.

Figure 4.6 shows sections of the dextrous boundary $\partial\boldsymbol{A}\left[0^\circ,\ 0^\circ,\ (-30^\circ)-(30^\circ)\right]$ mapped in the vertical plane at $\theta_i = 0^\circ$ and $\theta_i = 180^\circ$.

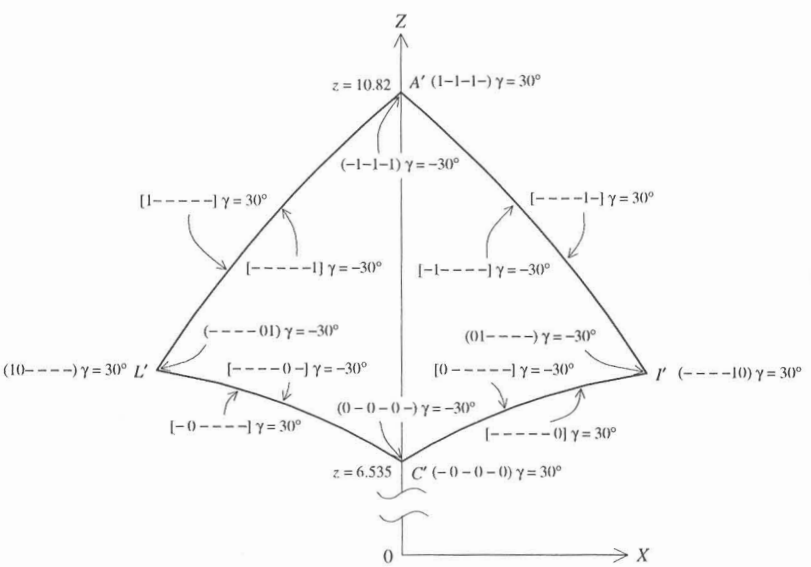

Figure 4.6 Sections of the dextrous boundary $\partial\boldsymbol{A}\left[0^\circ,\ 0^\circ,\ (-30^\circ)-(30^\circ)\right]$ at $\theta_i = 0^\circ$ and $\theta_i = 180^\circ$.

This boundary was mapped as two fixed orientation accessible boundaries $\partial A\left[0^\circ,\ 0^\circ,\ -30^\circ\right]$ and $\partial A\left[0^\circ,\ 0^\circ,\ 30^\circ\right]$ and they coincide exactly as shown in Figure 4.6. The same behavior is also evident at the other vertical dextrous curves separating the dextrous boundary surfaces which makes it easy to map sections of the dextrous workspace as shown in Figure 4.6.

With reference to Figure 4.4, the convex dextrous boundary surface $A'I'J'\ \left[0^\circ,\ 0^\circ,\ (-30^\circ)-(30^\circ)\right]$ forms part the fixed orientation accessible boundary surface $A'F'G'\ \left[0^\circ,\ 0^\circ,\ 30^\circ\right]$. The concave dextrous boundary surface $C'I'J'\ \left[0^\circ,\ 0^\circ,\ (-30^\circ)-(30^\circ)\right]$ forms part of the fixed orientation accessible boundary surface $C'F'G'\ \left[0^\circ,\ 0^\circ,\ 30^\circ\right]$. This implies that the first 60° of the dextrous workspace boundary $\partial A\left[0^\circ,\ 0^\circ,\ (-30^\circ)-(30^\circ)\right]$ may be found by mapping the first 60° of the fixed orientation accessible workspace $A\left[0^\circ,\ 0^\circ,\ 30^\circ\right]$.

Similarly, the convex dextrous boundary surface $A'J'K'\ \left[0^\circ,\ 0^\circ,\ (-30^\circ)-(30^\circ)\right]$ forms part of the fixed orientation accessible boundary surface $A'B'E'\ \left[0^\circ,\ 0^\circ,\ -30^\circ\right]$. The concave dextrous boundary surface $C'J'K'\ \left[0^\circ,\ 0^\circ,\ (-30^\circ)-(30^\circ)\right]$ forms part of the fixed orientation accessible boundary surface $C'E'B'\ \left[0^\circ,\ 0^\circ,\ -30^\circ\right]$. The dextrous boundary $\partial A\left[0^\circ,\ 0^\circ,\ (-30^\circ)-(30^\circ)\right]$ spanning $\theta_i = 60^\circ$ to $\theta_i = 120^\circ$ may therefore be found by mapping the corresponding range ($\theta_i = 60^\circ$ to $\theta_i = 120^\circ$) of the fixed orientation accessible workspace $A\left[0^\circ,\ 0^\circ,\ -30^\circ\right]$. In practice the intersection of the two fixed orientation workspaces is relatively easy to compute.

The three fold symmetry of the dextrous workspace $A\left[0^\circ,\ 0^\circ,\ (-30^\circ)-(30^\circ)\right]$ also necessitates only the first 120° be mapped.

The validity of assumption (2.30) in Section 2.6.4.4, and applied here to the spatial case, is shown in Figure 4.7, where the different fixed orientation accessible workspaces determined in this chapter are placed at an X-offset next to each other. The dextrous workspace $A\left[0^\circ,\ 0^\circ,\ (-30^\circ)-(30^\circ)\right]$ clearly satisfies condition (2.31) of Section 2.6.4.4.

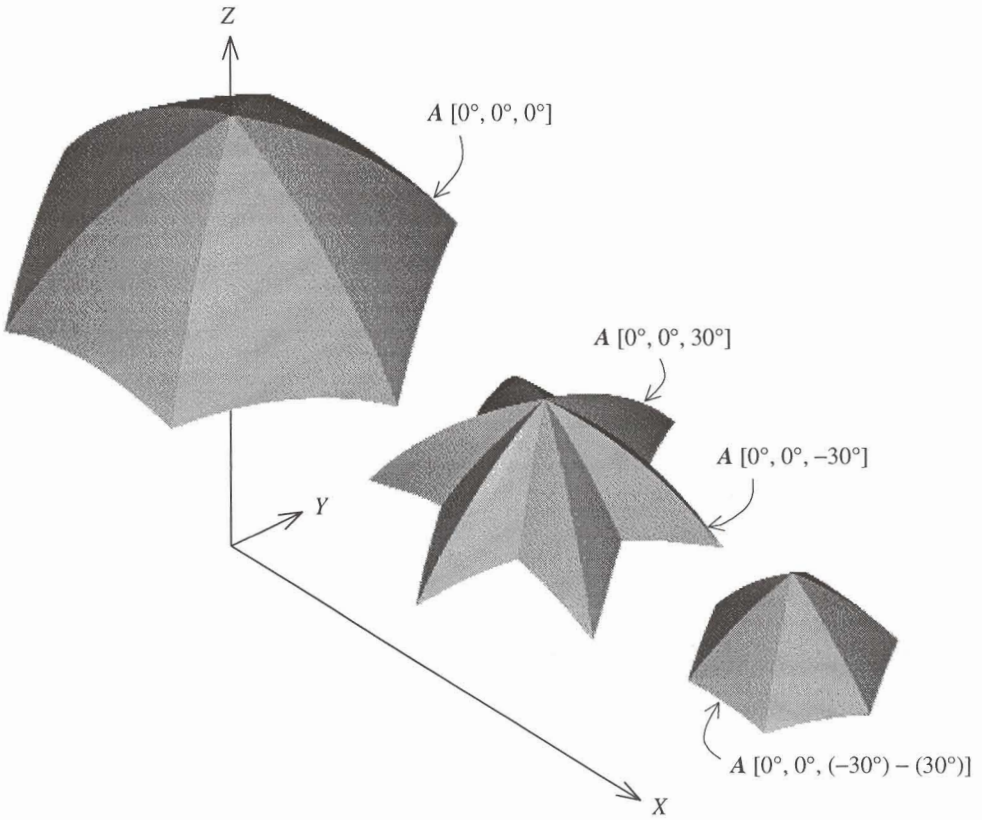

Figure 4.7 $A[0^\circ, 0^\circ, 0^\circ]$, the overlap of $A[0^\circ, 0^\circ, -30^\circ]$ and $A[0^\circ, 0^\circ, 30^\circ]$ and the final dextrous workspace $A[0^\circ, 0^\circ, (-30^\circ)-(30^\circ)]$.

Chapter 5

5 CONCLUSION

The main objective of this study has been achieved. From the results presented in this study, it is evident that the proposed optimization approach is indeed a *general* numerical method by means of which different types of workspaces of different classes of mechanical manipulators may *easily* be determined. The generality of the method is illustrated by the fact that the optimization method was successfully implemented for a redundantly controlled planar serial manipulator, a planar Stewart platform as well as a spatial 6–3 Stewart platform.

The validity of the optimization approach is established beyond doubt by a comparison of the results obtained for the planar manipulators with those reported by Haug et al. [8, 12] in their state-of-the-art articles on the continuation method. This is particularly reassuring and encouraging since Haug is considered one of the world's leading authorities on computer aided design of mechanical systems [45, 46]. Not only was the outer accessible workspace boundaries mapped, but also the curves connecting the bifurcation points situated on the outer boundary with those situated inside the accessible output set.

The mapping of the curves connecting the bifurcation points of the planar Stewart platform show that the optimization method easily handles the situation where the upper platform becomes collinear with one of the actuator legs, resulting in a singularity. Once all the singularities are identified, any required path can be planned to avoid those regions where the control of the Stewart platform becomes a problem. The method is therefore successful in assisting in the characterization of the workspace and of great potential importance with regard to the control of manipulators.

The description of the behavior of the planar manipulators led to a new notation for labeling the bifurcation points and curves of the workspaces. This notation arises in a natural way from the optimization approach, is generally applicable and easy to understand. Using this notation, the complete workspace may be described in terms of the behavior of the manipulator. This notation is more than a simple labeling since it allows for a concise and unambiguous description of the configuration of a manipulator at any allowable position and orientation. It is hoped that this notation will be accepted and adopted by workers in this field since, the belief is, that it will certainly assist in a clearer description of manipulator operations and thus will be invaluable with regard to communication between workers.

Of great practical importance is the treatment of dexterity requirements imposed on a Stewart platform. The optimization approach successfully determines different specified dextrous workspaces of the *planar* Stewart platform. Using the new notation, the boundaries containing the dextrous workspace are easily identified and labeled. Consequently the behavior of the planar Stewart platform when situated on these boundaries, may be described in detail.

As far as the *spatial* 6–3 Stewart platform is concerned, the workspace results obtained by the optimization approach gives a much more detailed description of the workspace than that previously reported by Liu et al. [18]. Here, for the orientationally unrestricted workspace, a single vertical plane of the accessible workspace was mapped and labeled using the optimization approach. The results show that mechanically infeasible regions are enclosed in the orientationally unrestricted workspace. Without the labeling notation suggested by the optimization approach, it may have been impossible for this important conclusion to be reached.

A very important achievement of this study is that an example of a dextrous workspace of the 6–3 Stewart platform was successfully mapped. The dexterity requirement is simple but of practical importance. It specifies a rotatability range for only one of the three orientation angles, with the other two orientation angles remaining fixed. The determination of this dextrous workspace is very significant because, as far as the author is aware, such a mapping has not previously been performed for the spatial case. In general of course, a dextrous workspace will imply that dexterity requirements are specified for all three orientation angles. There is no reason to believe that the current method will not be able to achieve this as well.

The proposed labeling notation was easily extended to label the surfaces containing the dextrous workspace as well. As with the planar Stewart platform, it was shown that the optimization method is a powerful tool with which the practical useful dextrous workspaces can be determined and characterized.

It is hoped that this study will lie the foundation for the development of a general and rational synthesis design tool for parallel manipulators. However, reviewing the research reported here, certain further and immediate research tasks are identified. Although the planar Stewart platform was analyzed in detail as far as the reachable and various dextrous workspaces are concerned, this is not so for the spatial platforms. An extension of the research done on the 6–3 Stewart platform workspaces remains to be done where the *full* orientationally unconstrained accessible workspace and any *general* specified dextrous workspace is to be mapped and labeled. In addition, the work must be extended to the *general* 6–6 Stewart platform.

Another outstanding problem of important practical value, is the determination of the *mechanically* feasible orientationally unconstrained reachable workspaces for both planar and spatial Stewart platforms. Here, actuator leg interference and actuator joint orientation range limits need to be considered as additional constraints in the implementation of the optimization method.

This study has important potential impact for the manufacturing industry of South Africa and other developing countries. The implementation of this technology lies primarily in retrofitting existing non-CNC milling equipment to increase their capability at a lower cost than that of the alternative of purchasing traditional 5-axis machining centers [47]. One of the industries that can benefit from such a development is, for example, the plastic injection molding industry, where mould manufacturing is an expensive and time consuming operation.

As a first step towards the successful implementation of such a retrofit, it is foreseen that a planar type Stewart platform be fitted to an existing 3-axis machining center that will result in 4-axis milling capabilities. A planar type manipulator will be easier and cheaper to manufacture than a spatial manipulator, and such a 4-axis CNC mill will, to some extent, fulfill in the machining requirements of the plastic injection molding industry. It is however envisaged to extend the machining capability to a higher competitive level by the eventual fitting of fully spatial Stewart platforms. This will only be possible through the use of sophisticated and powerful design tools of which, it is hoped, the foundation was laid here.

Further future research to be done also includes the extension of the optimization approach to incorporate the mapping of the so-called *quality index* [13] of any configuration within the mechanically feasible dextrous workspace. This will give further characterization of the workspace and provide valuable information regarding the utility of various regions of the workspace. The quality index should also reflect any singularities, and therefore give an indication of the safe regions within which the manipulator can be maneuvered and controlled.

In conjunction with the mapping of the quality index, adjustable positioning of the actuator leg joints on the base and moving platforms can be utilized to optimize the mechanically feasible dextrous workspace for any required machine tool path.

A further important point which emerges from this study and is worth mentioning relates to forward kinematics. The exercise of mapping bifurcation curves leads to the possibility of successfully performing forward kinematics through an optimization approach. This may lead to a competitive continuation method and therefore justifies further investigation.

Appendix A

A Computer Program for Determining the Planar Stewart Platform Workspace (*PLANSTEW*)

A.1 INTRODUCTION

This appendix explains the automated computer program *PLANSTEW* that was used to map the accessible output sets as well as the bifurcation point connecting curves of the planar Stewart platform.

PLANSTEW consists of a *main program* and a few *subroutines*. The outlay of the main program is shown in Figure A.1, and the different subroutines are shown in Figure A.2, Figure A.3, Figure A.6 and Figure A.7. The detail of the main program is explained here and the discussions of the subroutines are included as sub-paragraphs.

A.2 THE MAIN PROGRAM

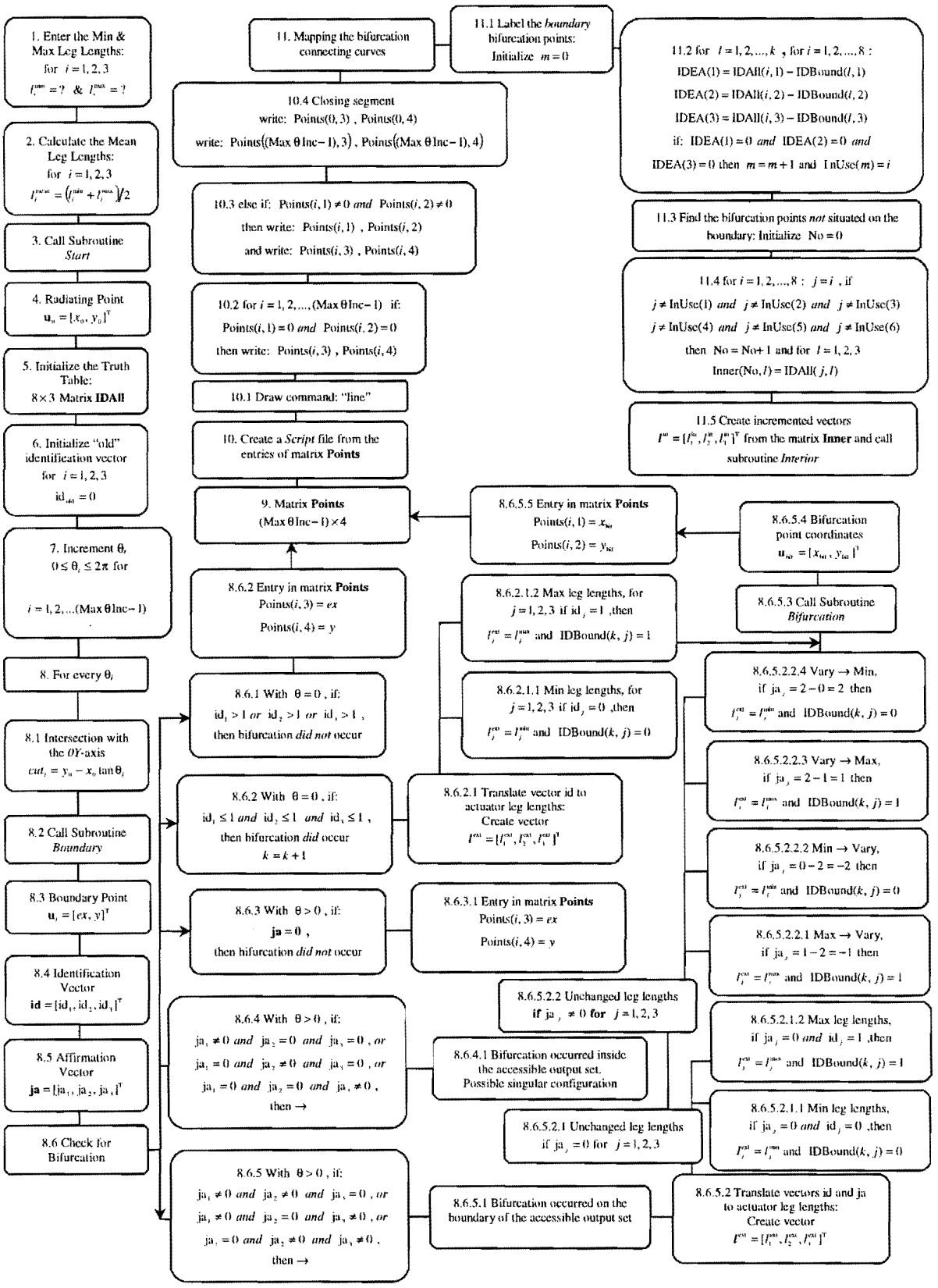

Figure A.1 Flow chart showing the layout of the main program.

Looking at Figure A.1, the first thing the user has to enter, is the respective minimum and maximum actuator leg lengths. The main program then calculates the mean actuator leg lengths.

$$l_i^{\text{mean}} = \frac{l_i^{\min} + l_i^{\max}}{2} \tag{A.1}$$

for $i = 1, 2, 3$

Equation (2.1) is used in equation (2.10), remembering that the actuator leg lengths were chosen as the input variables. Subroutine *Start* is used to determine the initial central point $\mathbf{u}^0$.

A.2.1 Subroutine *Start*

In the flow chart showing the lay out of subroutine *Start* (see Figure A.2), it is evident that the user has to enter an initial guess as to where the central point $\mathbf{u}^0$ is situated. This initial guess preferably has to be inside the accessible output set, and for the planar Stewart platform under consideration, the initial guess that was entered, is $(x, y) = (1.0,\ 1.2)$.

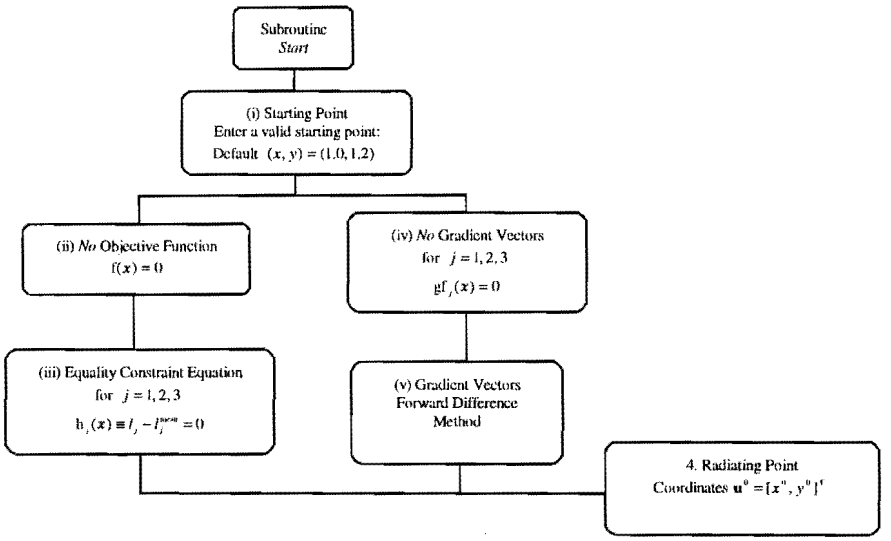

Figure A.2 Subroutine *Start*.

There is no explicit objective function, as the three non-linear equations are entered as equality constraints, i.e.

$$\begin{aligned} v_1(\mathbf{u}, w) - v_1^{\text{mean}} &= 0 \\ v_2(\mathbf{u}, w) - v_2^{\text{mean}} &= 0 \\ v_3(\mathbf{u}, w) - v_3^{\text{mean}} &= 0 \end{aligned} \tag{A.2}$$

The gradient vectors of the equality constraints are determined numerically using the forward difference method:

$$\frac{\partial f(\boldsymbol{x}_i)}{\partial x_j} \approx \frac{\left(f(\boldsymbol{x}_i + \Delta \boldsymbol{x}_j)\right) - f(\boldsymbol{x}_i)}{\Delta x_j} \tag{A.3}$$

The three non-linear equations are solved by minimizing the square of the Euclidean norm (2.11), and the output of subroutine *Start* is the radiating point $\mathbf{u}^0$ from where the boundary of the planar Stewart platform is mapped.

The next step in the main program (step 5 in Figure A.1), is to initialize the "truth table". Knowing that the planar Stewart platform has three legs each having two extreme positions, it is evident that there are $2^3 = 8$ bifurcation points. This truth table is used to identify which bifurcation points are situated on the boundary of the accessible output set. The remaining bifurcation points are used to trace the bifurcation connection curves as will be explained later.

The initialization of the truth table involves creating an 8×3 matrix **IDAll** where each row represents a different bifurcation point. The entry in each of the three columns indicates whether the corresponding leg takes on a minimum or maximum length with the manipulator working point corresponding with that specific bifurcation point. Based on the proposed labeling notation (Section 2.5.3.1), a 1 entry in column i indicates that leg i takes on a maximum length, and a 0 entry that leg i takes on a minimum length.

Step 6 in Figure A.1 is the initialization of the vector $\mathbf{id}_{\text{old}}$. This is an "old" identification vector, and it is used in subroutine *Boundary*. An auxiliary variable θ is defined in the main program to be used in the mapping of the planar accessible output set as discussed in Section (2.4). This orientation angle θ is incremented from 0 to 2π, as follows:

$$\theta_i = \frac{i(2\pi)}{\text{Max}\,\theta\,\text{Inc}} \tag{A.4}$$

for $i = 0, 1, 2, \ldots, (\text{Max}\,\theta\,\text{Inc} - 1)$.

The user decides on the number of increments required, and defines the parameter "MaxθInc". It follows that once the parameter "MaxθInc" is specified, the increment size δ of the emanating rays used for mapping the planar accessible output set (see Section 2.4), is fixed.

$$\delta = \frac{2\pi}{\text{Max}\,\theta\,\text{Inc}} \tag{A.5}$$

For each orientation angle θ_i, the intersection of the specific emanating ray with the *0Y*-axis (Cut_i) is determined in the main program (7.1 in Figure A.1), as it is used in subroutine *Boundary*.

$$Cut_i = y^0 - x^0 \tan(\theta_i) \tag{A.6}$$

for $i = 0, 1, 2, \ldots, (\text{Max}\,\theta\,\text{Inc} - 1)$

A.2.2 Subroutine *Boundary*

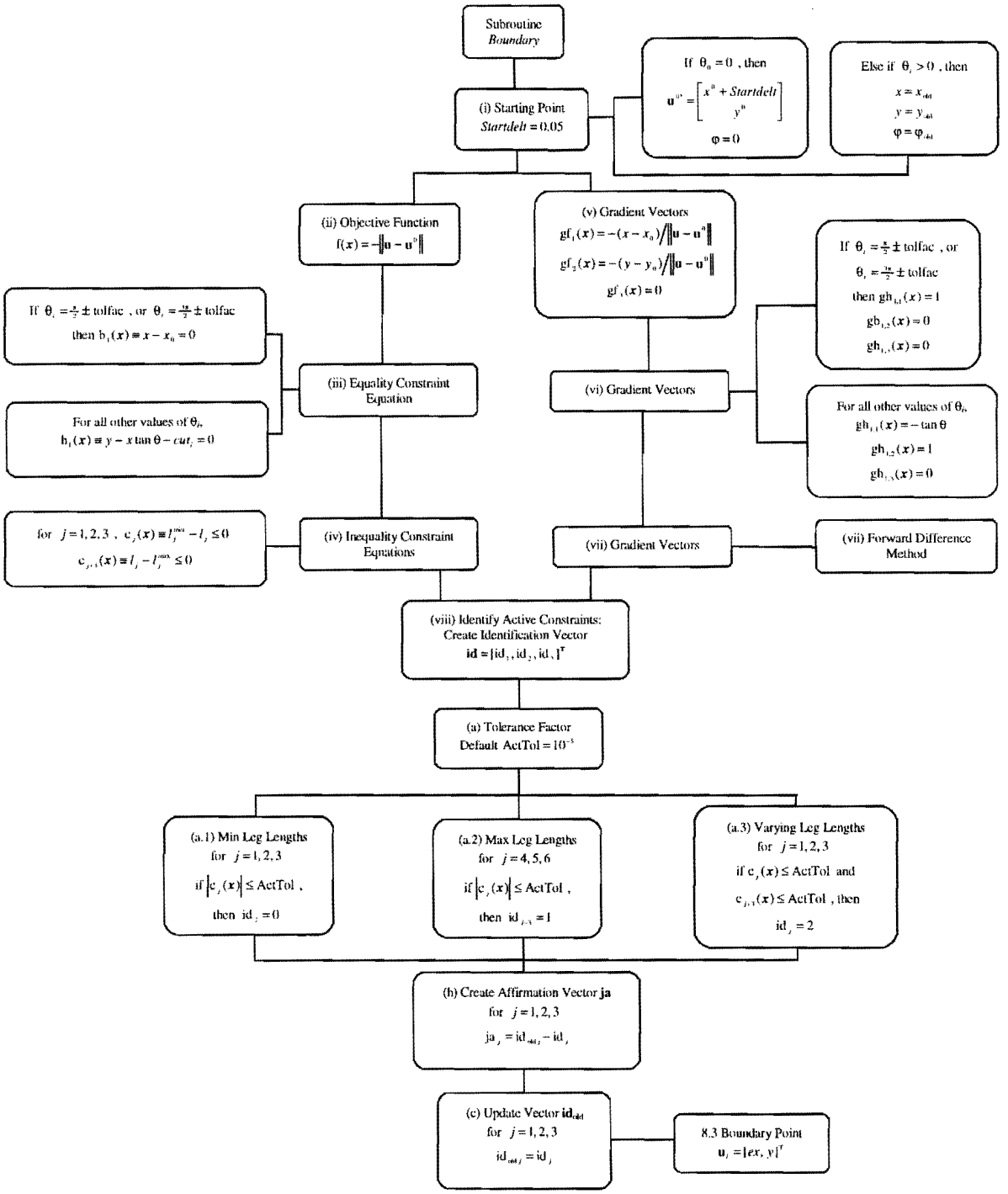

Figure A.3 Subroutine *Boundary*.

With $\theta_0 = 0$, an initial point on ∂A is sought, and optimization *problem (i)* as described in Section 2.3 is applicable. In order to make sure that the maximization is not done π out of phase, an offset (*Startdelt*) is added to the x-value of the radiating point $\mathbf{u}^0$. The actual radiating point used to find the initial point on ∂A with $\theta_0 = 0$, is $\mathbf{u}^{0*}$:

Looking at Figure A.1, the first thing the user has to enter, is the respective minimum and maximum actuator leg lengths. The main program then calculates the mean actuator leg lengths.

$$l_i^{\text{mean}} = \frac{l_i^{\min} + l_i^{\max}}{2} \tag{A.1}$$

for $i = 1, 2, 3$

Equation (2.1) is used in equation (2.10), remembering that the actuator leg lengths were chosen as the input variables. Subroutine *Start* is used to determine the initial central point $\mathbf{u}^0$.

A.2.1 Subroutine *Start*

In the flow chart showing the lay out of subroutine *Start* (see Figure A.2), it is evident that the user has to enter an initial guess as to where the central point $\mathbf{u}^0$ is situated. This initial guess preferably has to be inside the accessible output set, and for the planar Stewart platform under consideration, the initial guess that was entered, is $(x, y) = (1.0,\ 1.2)$.

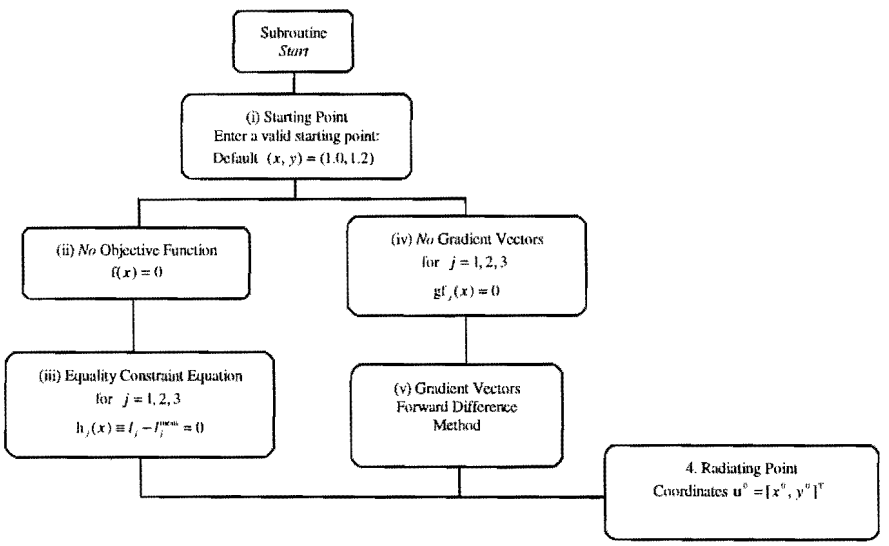

Figure A.2 Subroutine *Start*.

There is no explicit objective function, as the three non-linear equations are entered as equality constraints, i.e.

$$\begin{aligned} v_1(\mathbf{u}, w) - v_1^{\text{mean}} &= 0 \\ v_2(\mathbf{u}, w) - v_2^{\text{mean}} &= 0 \\ v_3(\mathbf{u}, w) - v_3^{\text{mean}} &= 0 \end{aligned} \tag{A.2}$$

The gradient vectors of the equality constraints are determined numerically using the forward difference method:

$$\frac{\partial f(\boldsymbol{x}_i)}{\partial x_j} \approx \frac{\left(f(\boldsymbol{x}_i + \Delta \boldsymbol{x}_j)\right) - f(\boldsymbol{x}_i)}{\Delta x_j} \tag{A.3}$$

The three non-linear equations are solved by minimizing the square of the Euclidean norm (2.11), and the output of subroutine *Start* is the radiating point $\mathbf{u}^0$ from where the boundary of the planar Stewart platform is mapped.

The next step in the main program (step 5 in Figure A.1), is to initialize the "truth table". Knowing that the planar Stewart platform has three legs each having two extreme positions, it is evident that there are $2^3 = 8$ bifurcation points. This truth table is used to identify which bifurcation points are situated on the boundary of the accessible output set. The remaining bifurcation points are used to trace the bifurcation connection curves as will be explained later.

The initialization of the truth table involves creating an 8×3 matrix **IDAll** where each row represents a different bifurcation point. The entry in each of the three columns indicates whether the corresponding leg takes on a minimum or maximum length with the manipulator working point corresponding with that specific bifurcation point. Based on the proposed labeling notation (Section 2.5.3.1), a 1 entry in column i indicates that leg i takes on a maximum length, and a 0 entry that leg i takes on a minimum length.

Step 6 in Figure A.1 is the initialization of the vector $\mathbf{id}_{\text{old}}$. This is an "old" identification vector, and it is used in subroutine *Boundary*. An auxiliary variable θ is defined in the main program to be used in the mapping of the planar accessible output set as discussed in Section (2.4). This orientation angle θ is incremented from 0 to 2π, as follows:

$$\theta_i = \frac{i(2\pi)}{\text{Max}\,\theta\,\text{Inc}} \tag{A.4}$$

for $i = 0, 1, 2, \ldots, (\text{Max}\,\theta\,\text{Inc} - 1)$.

The user decides on the number of increments required, and defines the parameter "MaxθInc". It follows that once the parameter "MaxθInc" is specified, the increment size δ of the emanating rays used for mapping the planar accessible output set (see Section 2.4), is fixed.

$$\delta = \frac{2\pi}{\text{Max}\,\theta\,\text{Inc}} \tag{A.5}$$

For each orientation angle θ_i, the intersection of the specific emanating ray with the *0Y*-axis (Cut_i) is determined in the main program (7.1 in Figure A.1), as it is used in subroutine *Boundary*.

$$Cut_i = y^0 - x^0 \tan(\theta_i) \tag{A.6}$$

for $i = 0, 1, 2, \ldots, (\text{Max}\,\theta\,\text{Inc} - 1)$

A.2.2 Subroutine *Boundary*

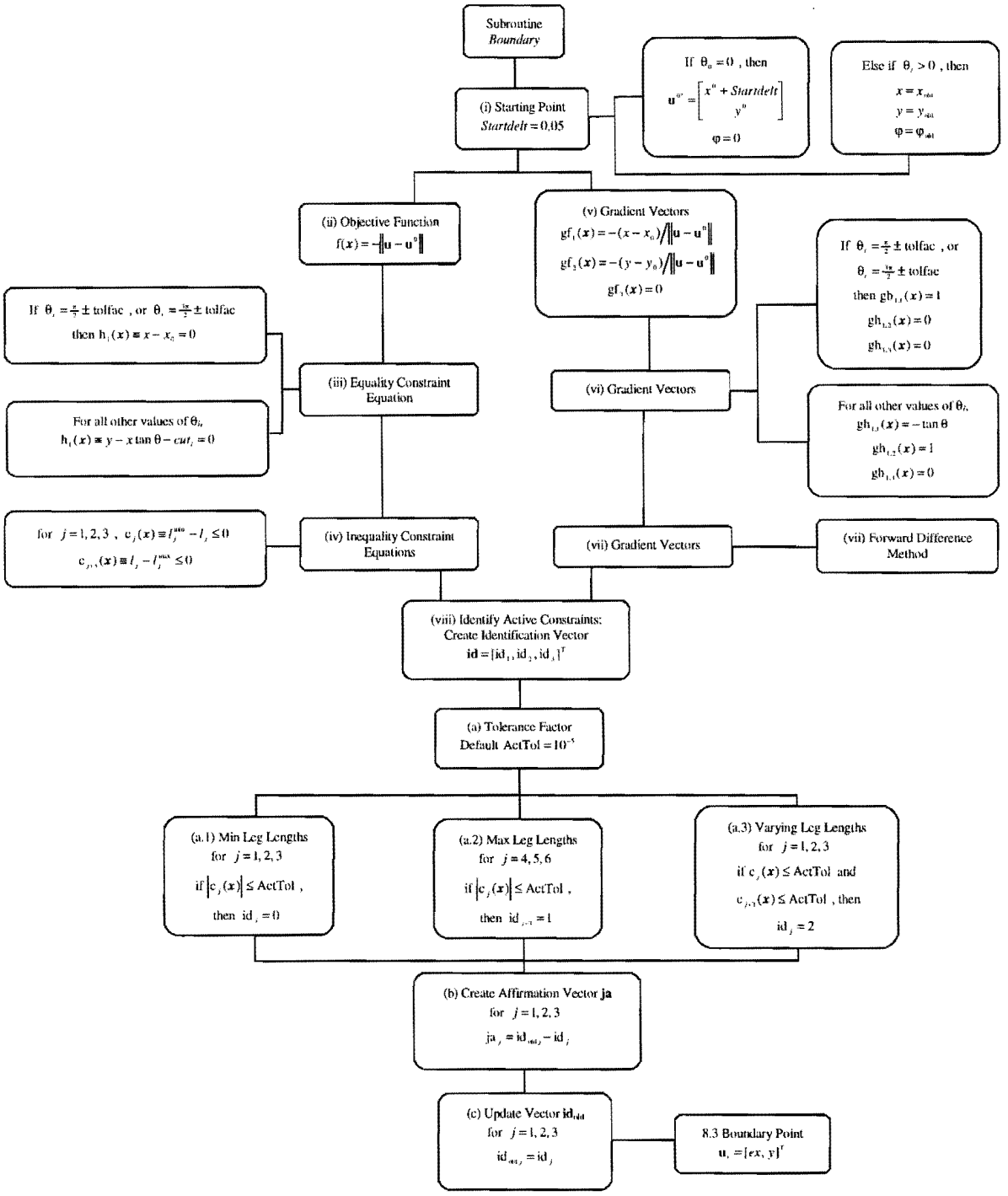

Figure A.3 Subroutine *Boundary*.

With $\theta_0 = 0$, an initial point on ∂A is sought, and optimization *problem (i)* as described in Section 2.3 is applicable. In order to make sure that the maximization is not done π out of phase, an offset (*Startdelt*) is added to the x-value of the radiating point $\mathbf{u}^0$. The actual radiating point used to find the initial point on ∂A with $\theta_0 = 0$, is $\mathbf{u}^{0*}$:

$$\mathbf{u}^{0*} = \begin{bmatrix} x^0 + Startdelt \\ y^0 \end{bmatrix} \tag{A.7}$$

With $\theta_i > 0$, the output and intermediate coordinates of the previous boundary point is used as an initial guess for the new boundary point sought.

Maximization *problem (i)* of Section 2.3 is converted to an equivalent minimization problem as follows:

$$\underset{\mathbf{u},\mathbf{w}}{minimize} \; -\left\|\mathbf{u}-\mathbf{u}^0\right\| \tag{A.8}$$

Analytical expressions for the gradient vectors of the objective function are used in subroutine *Boundary* as can be seen in box (vi) of Figure A.3.

The θ_i and Cut_i values determined in the main program, are used in subroutine *Boundary* to impose the single equality constraint. A separate equality constraint had to be defined to accommodate the asymptotic behavior of the tan-function:

$$\begin{aligned} &\text{If } \theta_i = \tfrac{\pi}{2} \pm TolFac \text{ or } \theta_i = \tfrac{3\pi}{2} \pm TolFac\text{, then: } \quad \mathrm{h}_1 \equiv x - x^0 = 0 \\ &\qquad\qquad \text{(default value } TolFac = 0.001\text{)} \\ &\text{for all other values of } \theta_i\text{: } \quad \mathrm{h}_1 \equiv y - x\tan\theta_i - Cut_i = 0 \end{aligned} \tag{A.9}$$

Analytical expressions for the gradient vectors of the equality constraint are used as can be seen in Figure A.3.

The minimum and maximum leg lengths that were entered in the main program, are used in subroutine *Boundary* for the six inequality constraint equations (see box (v) in Figure A.3).

$$\begin{aligned} \mathrm{c}_j &\equiv l_i^{\min} - l_i \le 0 \\ \mathrm{c}_{j+3} &\equiv l_i - l_i^{\max} \le 0 \end{aligned} \tag{A.10}$$

for $j = 1, 2, 3$

These inequalities impose correspond to expression (2.18) of Section 2.6.1. Once again, the forward difference method (A.3) is used to determine the gradient vectors of the inequality constraints.

An important aspect of subroutine *Boundary*, is to identify the active inequality constraints, as the mapping of the boundary is done. For each θ_i, $i = 0, 1, 2, \ldots, (\mathrm{Max}\,\theta\,\mathrm{Inc} - 1)$, the values of the

inequality constraints are monitored, and the entries of an identification vector, $\mathbf{id} = [\mathrm{id}_1, \mathrm{id}_2, \mathrm{id}_3]^T$, as well as the entries of an affirmation vector $\mathbf{ja} = [\mathrm{ja}_1, \mathrm{ja}_2, \mathrm{ja}_3]^T$ is determined. These vectors are used in the main program to identify the *bifurcation points*, as the workspace boundary is mapped.

A tolerance factor *ActTol* is associated with vector **id**, and its magnitude is specified by the user (default value $ActTol = 10^{-5}$). Each entry of the vector **id** can have one of three possible entries:

- if any of the actuator legs is at its minimum length, the corresponding entry in vector **id** will have the value *zero*.

$$\therefore \text{for } j = 1,2,3: \text{ if } |c_j| \le \text{ActTol}, \text{ then } \mathrm{id}_j = 0$$

- if any of the actuator legs is at its maximum length, the corresponding entry in vector **id** will have the value *one*.

$$\therefore \text{for } j = 4,5,6: \text{ if } |c_j| \le \text{ActTol}, \text{ then } \mathrm{id}_{j-3} = 1$$

- if any of the actuator legs is varying anywhere between its minimum and maximum length, the corresponding entry in vector **id** will have the value *two*.

$$\therefore \text{for } j = 1,2,3: \text{ if } c_j \le \text{ActTol } \textit{and } c_{j+3} \le \text{ActTol}, \text{ then } \mathrm{id}_j = 2$$

The entries of the affirmation vector (**ja**) is determined at each θ_i, $i = 0, 1, 2, \ldots, (\text{Max}\,\theta\,\text{Inc} - 1)$, by subtracting the current identification vector (**id** obtained for θ_i, $i = 1, 2, \ldots, \text{Max}\,\theta\,\text{Inc} - 1$) from the "old" identification vector ($\mathbf{id}_{\text{old}}$, which in actual fact is **id** obtained for θ_i, $i = 0, 1, 2, \ldots, \text{Max}\,\theta\,\text{Inc} - 2$).

$$\mathbf{ja} = \mathbf{id}_{\text{old}} - \mathbf{id} \tag{A.11}$$

With $\theta_0 = 0$, the initialized vector $\mathbf{id}_{\text{old}} = [0, 0, 0]^T$ is used to determine the affirmation vector (**ja**). After the affirmation vector has been determined, the vector $\mathbf{id}_{\text{old}}$ is updated, i.e. for $j = 1, 2, 3$, $\mathrm{id}_{\text{old}\,j} = \mathrm{id}_j$.

The coordinates of the "boundary point" ($\mathbf{u}^{bi} = [ex, y]^T$),the identification vector **id** as well as the affirmation vector **ja** are transferred back to the main program.

Each boundary bifurcation point is entered in a consecutive row *k* of the matrix **IDBound** using a similar notation to the one used for matrix **IDAll**. Once all the boundary bifurcation points are found, a comparison between the matrices **IDAll** and **IDBound** allows for the isolation of the bifurcation points

not situated on the accessible output set boundary. Counter k is initialized before the boundary mapping is started.

The main program uses the two vectors **id** and **ja** to identify the bifurcation points as the workspace boundary is mapped.

Clearly it is possible to intersect a bifurcation point with ray 0 where $\theta_0 = 0$, and provision is made to identify such a bifurcation point, if this happens.

with $\theta_0 = 0$, if: $\mathrm{id}_1 > 1$, *or* $\mathrm{id}_2 > 1$, *or* $\mathrm{id}_3 > 1$, then a bifurcation point *is not* intersected by ray 0.

with $\theta_0 = 0$, if: $\mathrm{id}_1 \leq 1$, *and* $\mathrm{id}_2 \leq 1$, *and* $\mathrm{id}_3 \leq 1$, then a bifurcation point *is* intersected by ray 0.

Increment counter $k = k + 1$

With $\theta_0 = 0$, the identification vector (**id**) shows whether each of the three actuator legs is at its maximum or minimum length.

With $\theta_i > 0$, it is the affirmation vector (**ja**) that indicates whether a bifurcation point is situated between two successively mapped boundary points:

with $\theta_i > 0$, if: $\mathrm{ja}_1 = 0$, *and* $\mathrm{ja}_2 = 0$, *and* $\mathrm{ja}_3 = 0$,

then a bifurcation point *is not* present between rays i and $i-1$.

with $\theta_i > 0$, if: $\mathrm{ja}_1 \neq 0$, *and* $\mathrm{ja}_2 \neq 0$, *and* $\mathrm{ja}_3 = 0$,

or $\mathrm{ja}_1 \neq 0$, *and* $\mathrm{ja}_2 = 0$, *and* $\mathrm{ja}_3 \neq 0$, ***or*** $\mathrm{ja}_1 = 0$, *and* $\mathrm{ja}_2 \neq 0$, *and* $\mathrm{ja}_3 \neq 0$,

then a bifurcation point *is* present between rays i and $i-1$.

Increment counter $k = k + 1$.

The detail of why any two entries of the affirmation vector **ja** has to be non-zero values to indicate bifurcation is evident from the discussion of the results in Section 2.6.3.1.

The main program creates a matrix called *Points* which has (MaxθInc) rows and four columns. The global x- and y-coordinates of mapped workspace boundary are respectively entered in columns 3 and 4 of matrix *Points* (see Box 8 in Figure 9). The global x- and y-coordinates of the mapped bifurcation points are respectively entered in columns 1 and 2 of matrix *Points*. This matrix is then used to create a drawing of the workspace (see Figure A.4).

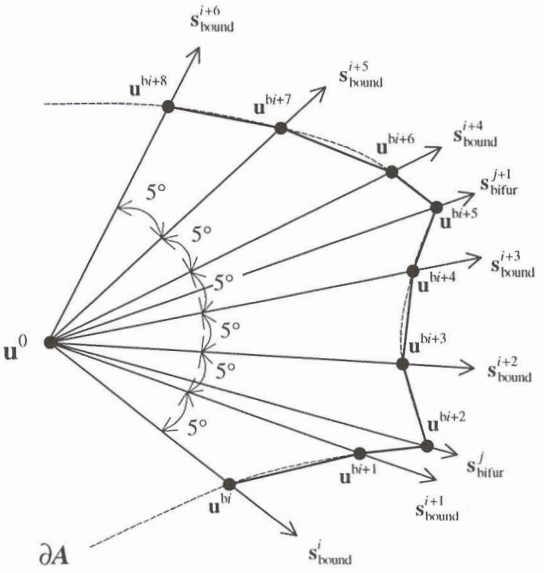

Figure A.4 Finding ∂A using *boundary* and *bifurcation* mappings.

If only the *boundary* mappings are used, the danger exists of inaccurately mapping the accessible output set as shown in Figure A.5.

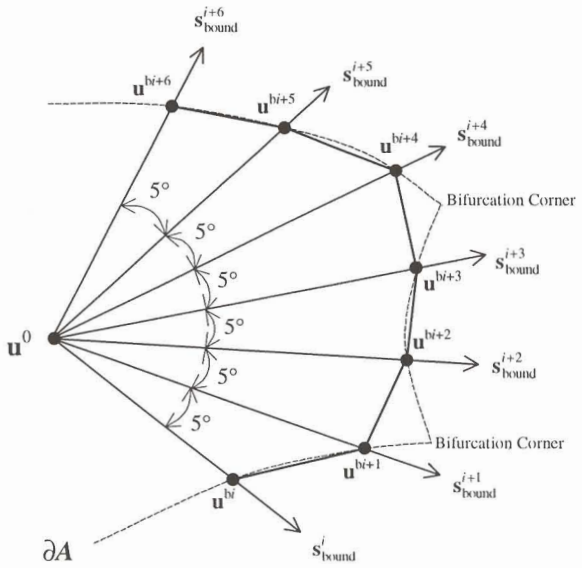

Figure A.5 Finding ∂A using only *boundary* mappings.

As soon as bifurcation point is identified between two boundary mappings, the specific coordinates of the bifurcation point is determined, and entered into columns 1 and 2 of matrix *Points*. The determination of the bifurcation point coordinates is done by interpretating the vector **id** (for $\theta_0 = 0$) *or*

the vector **ja** *and* the vector **id** (for $\theta_i > 0$) to determine the actual lengths of the actuator legs, and creating a vector containing these extreme actuator leg lengths $\boldsymbol{l}^{\text{ext}} = [l_1^{\text{ext}}, l_2^{\text{ext}}, l_3^{\text{ext}}]^{\text{T}}$. The vector $\boldsymbol{l}^{\text{ext}}$ is then used in subroutine *Bifurcation* to determine the coordinates of the bifurcation point.

If a bifurcation point is intersected by ray 0 where $\theta_0 = 0$, the vector $\boldsymbol{l}^{\text{ext}}$ is determined from the entries of the identification vector:

- extreme leg lengths corresponding to the minimum leg lengths:

$$\therefore \text{for } j = 1,2,3: \text{ if } \text{id}_j = 0, \text{ then } l_j^{\text{ext}} = l_j^{\min}$$

$$\text{IDBound}(k, j) = 0$$

- extreme leg lengths corresponding to the maximum leg lengths:

$$\therefore \text{for } j = 1,2,3: \text{ if } \text{id}_j = 1, \text{ then } l_j^{\text{ext}} = l_j^{\max}$$

$$\text{IDBound}(k, j) = 1$$

With $\theta_i > 0$, a bifurcation point is identified if any two entries of the affirmation matrix **ja** is a non-zero value. Since $\mathbf{ja} = \mathbf{idold} - \mathbf{id}$, two entries of the vector **id** change when a bifurcation point is present in the section of the boundary contained between the vectors **idold** and **id**. Mapping the *unchanged* leg lengths is done by examining the vector **id** as well as the vector **ja**.

- extreme leg lengths corresponding to the minimum leg lengths:

$$\therefore \text{for } j = 1,2,3: \text{ if } \text{id}_j = 0 \textit{ and } \text{ja}_j = 0, \text{ then } l_j^{\text{ext}} = l_j^{\min}$$

$$\text{IDBound}(k, j) = 0$$

- extreme leg lengths corresponding to the maximum leg lengths:

$$\therefore \text{for } j = 1,2,3: \text{ if } \text{id}_j = 1 \textit{ and } \text{ja}_j = 0, \text{ then } l_j^{\text{ext}} = l_j^{\max}$$

$$\text{IDBound}(k, j) = 1$$

Mapping the *changed* leg lengths is done by examining only the vector **ja**.

- maximum leg lengths *changing* to varying leg lengths:

$$\therefore \text{for } j = 1,2,3: \text{ if } \text{ja}_j = 1 - 2 = -1, \text{ then } l_j^{\text{ext}} = l_j^{\max}$$

$$\text{IDBound}(k, j) = 1$$

- minimum leg lengths *changing* to varying leg lengths:

$$\therefore \text{for } j = 1,2,3: \text{ if } \text{ja}_j = 0 - 2 = -2, \text{ then } l_j^{\text{ext}} = l_j^{\min}$$

$$\text{IDBound}(k, j) = 0$$

- varying leg lengths *changing* to maximum leg lengths:

$$\therefore \text{for } j = 1,2,3 : \text{if } \text{ja}_j = 2 - 1 = 1, \text{ then } l_j^{\text{ext}} = l_j^{\max}$$

$$\text{IDBound}(k, j) = 1$$

- varying leg lengths *changing* to minimum leg lengths:

$$\therefore \text{for } j = 1,2,3 : \text{if } \text{ja}_j = 2 - 0 = 2, \text{ then } l_j^{\text{ext}} = l_j^{\min}$$

$$\text{IDBound}(k, j) = 0$$

The vector $\boldsymbol{l}^{\text{ext}}$ is transferred by the main program to subroutine *Bifurcation* where the coordinates of the bifurcation points are determined (see Figure A.6).

A.2.3 Subroutine *Bifurcation*:

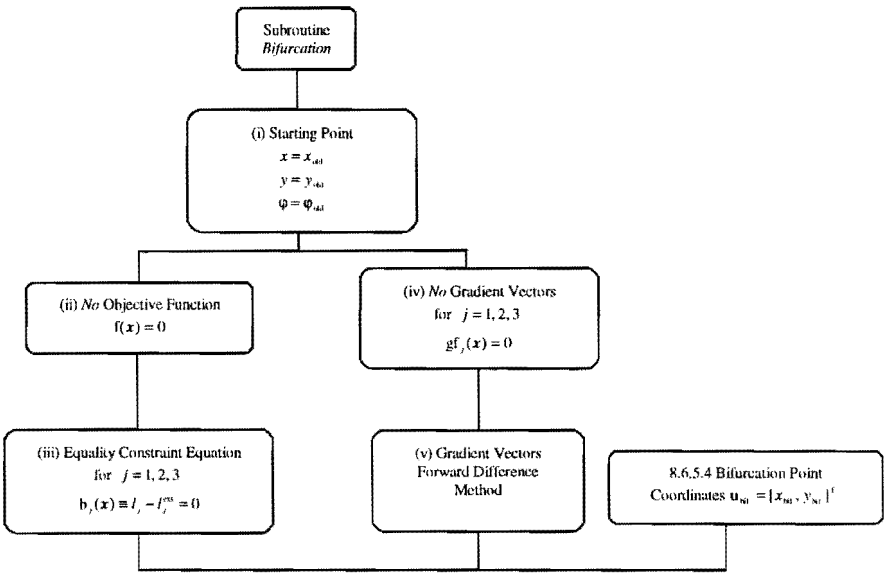

Figure A.6 Subroutine *Bifurcation*.

The starting point used in this subroutine is coordinates of the previous boundary point, and similar to subroutine *Start*, there is **no** explicit objective function, as well as **no** objective function gradient vectors for the code *LFOPCV3*.

The components of the vector $\boldsymbol{l}^{\text{ext}}$ are used in the three equality constraint equations shown in box (iv) of Figure A.6. *LFOPCV3* is once again used to solve three non-linear equations:

$$\begin{aligned} \text{v}_1(\mathbf{u}, \text{w}) - \text{v}_1^{\text{ext}} &= 0 \\ \text{v}_2(\mathbf{u}, \text{w}) - \text{v}_2^{\text{ext}} &= 0 \\ \text{v}_3(\mathbf{u}, \text{w}) - \text{v}_3^{\text{ext}} &= 0 \end{aligned} \qquad \text{(A.12)}$$

The gradient vectors of the equality constraints are determined using the forward difference method given by equation (A.3).

Once the coordinates of the bifurcation point ($\mathbf{u}^{bif} = [x^{bif}, y^{bif}]^T$) is determined, they are transferred to the main program, where they are respectively entered into columns 1 and 2 of the matrix *Points*.

Once the exterior boundaries are mapped, the bifurcation point connecting curves are traced using the matrices **IDAll** and **IDBound**. The first step in tracing the bifurcation point connecting curves is to identify the bifurcation points situated on the accessible output set boundary.

All row vectors of matrix **IDBound** is subsequently subtracted from each row vector in matrix **IDAll** to give the resultant vector **IDEA**:

$$\mathbf{IDEA} = \mathbf{IDAll} - \mathbf{IDBound} \tag{A.13}$$

If for any of the row vectors in matrix **IDBound** vector **IDEA** is a zero vector, the specific row vector in **IDAll** is labeled as it represents a bifurcation point situated on the boundary of the accessible output set. After the complete boundary is mapped, the unlabeled row vectors of **IDBound** is isolated and used to trace the bifurcation point connecting curves as described in Section 2.6.3.2 and set out in Figure A.2 and Figure A.7.

A.2.4 Subroutine Interior

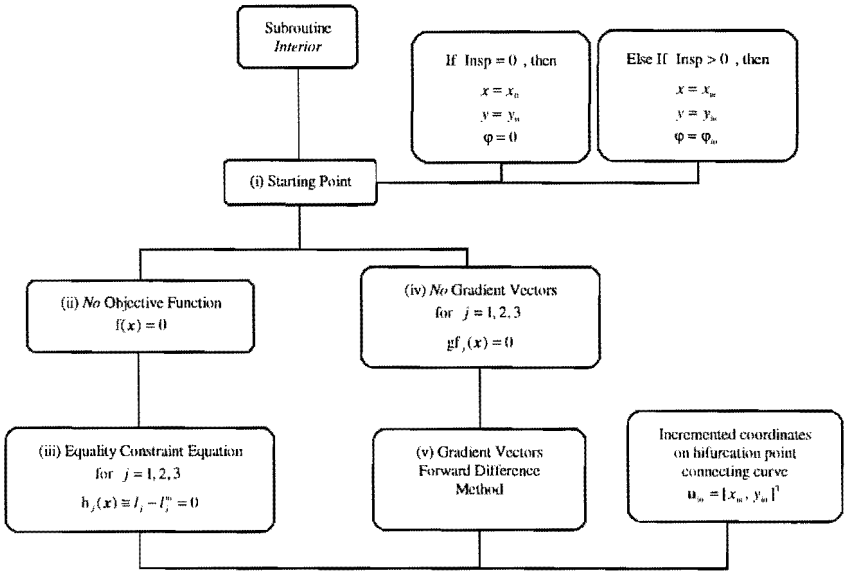

Figure A.7 Subroutine *Interior*

The starting point used in this subroutine is the radiating point $\mathbf{u}^0$ when the first point of a new bifurcation point connecting curve is to be traced. Once the first point on the curve is found, its coordinates are used as the starting point from where the next point on the curve is to be traced.

is coordinates of the previous boundary point, and similar to subroutine *Start* and *Bifurcation*, there is **no** explicit objective function, as well as **no** objective function gradient vectors for the code *LFOPCV3*.

The components of the vector $\boldsymbol{l}^{in}$ are used in the three equality constraint equations shown in box (iv) of Figure A.7. *LFOPCV3* is once again used to solve three non-linear equations:

$$\begin{aligned} v_1(\mathbf{u}, w) - v_1^{in} &= 0 \\ v_2(\mathbf{u}, w) - v_2^{in} &= 0 \\ v_3(\mathbf{u}, w) - v_3^{in} &= 0 \end{aligned} \tag{A.14}$$

The gradient vectors of the equality constraints are determined using the forward difference method given by equation (A.3).

Once the coordinates of the point on the interior curve ($\mathbf{u}^{in} = [x^{in}, y^{in}]^T$) is determined, they are transferred to the main program and entered into a *script* file from where the results are drawn.

This concludes the description of the computer code *PLANSTEW*.

Appendix B

B The Mapping of the Near Global Optimum Boundary Curves of the Reachable 6–3 Stewart Platform Workspace

The method for computing the accessible workspace for the 6–3 Stewart platform is explained further in this appendix, with the emphasis on the near global optimum boundary curves (*EF* $[11--11]$in Figure 3.3 and *DG* $[01--10]$ in Figure 3.4).

Following the "upward sweep" to map the reachable workspace as depicted in Figure 3.3, no problems occur as the near global optimum boundary curve *DE* $[-1111-]$ is mapped. Even for the first few rays mapping curve *EF* $[11--11]$, the near global maximum displacement from $\mathbf{u}^0$ is found time and again, and the first part of curve *EF* is easily determined as shown in Figure B.1. However, as curve *EF* is followed using the "upward sweep", the near global optimum is separated further and further from the global optimum situated along curve *FG* $[-1111-]$ (see Figure 3.2). As soon as the distance between the near global and global maximum displacements for two successive rays reaches a critical value, the optimizer *LFOPCV3* "jumps" to the global optimum for the latter ray. This explains the "jump" between the near global boundary curve *EF* $[11--11]$ and global boundary curve *FG* $[-1111-]$ as shown in Figure B.1.

Curve *EF* $[11--11]$ as presented in Figure 3.2 and Figure 3.3 is mapped with user interference. Because the first part of this curve is successfully determined, the optimization approach allows for the identification the actuator legs assuming extreme lengths as the working point follows curve *EF*. The label of curve *EF* $[11--11]$ stems from this identification procedure, and the label shows that actuator legs 1, 2, 5 and 6 remain fixed at their maximum lengths along curve *EF*.

Using a separate procedure, the complete near global optimum curve *EF* $[11--11]$ is mapped for N_R successive rays emanating in the range $121.8^\circ \leq \varphi_i \leq 180^\circ$ $(2.126 \leq \varphi_i \leq \pi)$, by minimizing the following error function using *LFOPCV3*.

$$e(\mathbf{u},\mathbf{w}) = \left(v_1(\mathbf{u},\mathbf{w}) - v_1^{\max}\right)^2 + \left(v_2(\mathbf{u},\mathbf{w}) - v_2^{\max}\right)^2 + \left(v_5(\mathbf{u},\mathbf{w}) - v_5^{\max}\right)^2 + \left(v_6(\mathbf{u},\mathbf{w}) - v_6^{\max}\right)^2 + (u_2 - u_1\tan 0)^2 + \left(\sqrt{u_{1j}^2 + u_{2j}^2} - (z^0 - u_{3j})\tan(\varphi_j)\right)^2 \quad \text{(B.1)}$$

The first four terms of (B.1) fixes the actuator legs at their extreme lengths while the fifth term fixes the vertical plane at $\theta_i = 0^\circ$. The last term of (B.1) corresponds to equation (3.15), and is incremented as curve EF $[11--11]$ is traced, i.e.

$$\varphi_j = 2.126 + \frac{j1.016}{N_R} \quad \text{(B.2)}$$

for $j = 0, 1, 2, \ldots, N_R$

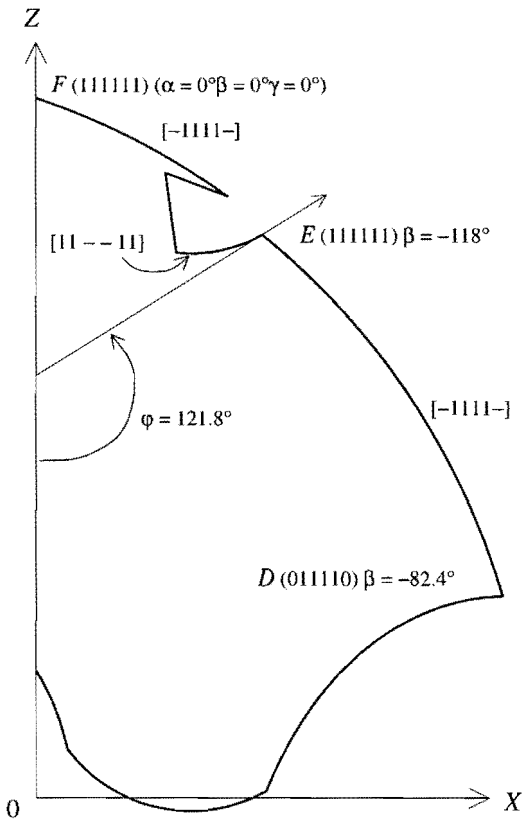

Figure B.1 The "jump" between the near global optimum and global optimum boundary curves.

Curve GD $[01--10]$ shown in Figure 3.4 is mapped in a similar manner.

Appendix C

C Procedure of Finding the Bifurcation Point Coordinates of the Fixed Orientation 6–3 Stewart Platform Workspace

As an extenuation of Section 4.3, an explanation follows on the details of how the bifurcation points on the boundary ($\partial A\ [0^\circ, 0^\circ, 0^\circ]$), of the fixed orientation workspace $A\ [0^\circ, 0^\circ, 0^\circ]$ of the 6–3 Stewart platform are mapped. Bifurcation point $B\ (0\ 1\ -\ -\ 1\ 0)\ [0^\circ, 0^\circ, 0^\circ]$ shown in Figure 4.1 and Figure 4.2(a) is used as a representative example.

Bifurcation point $B\ (0\ 1\ -\ -\ 1\ 0)\ [0^\circ, 0^\circ, 0^\circ]$ is found by minimizing an error function, corresponding to the planar case explained in Section 2.6.3.1, where an error function (2.24) was defined to find the point A' shown in Figure 2.10.

The error function used to find the coordinates of bifurcation point $B\ (0\ 1\ -\ -\ 1\ 0)\ [0^\circ, 0^\circ, 0^\circ]$, is again expressed in terms of the output coordinates (**u**) and intermediate coordinates (**w**).

Eight terms can be defined for the error function, one to "fix" the direction of the vertical plane (3.11), four terms to "fix" actuator legs 1, 2, 5 and 6 to their respective extreme lengths and a final three to "fix" the orientation of the top platform (4.4).

The error function of the planar Stewart platform is defined in terms of three coordinates (two output and one intermediate), and it consists of three terms. This means that for the spatial Stewart platform under consideration, the error function defined in terms of six variables should only have six terms.

Fortunately, not all eight of the possible terms are independent. The six terms used determine the orientation of the top platform (4.4) and any three of the four "active" actuator legs. Because the platform is symmetrical about the *X0Z* plane and all the leg length limits are the same, the fourth leg automatically assumes the correct extreme length at the correct orientation of the vertical plane.

Considering, for example, bifurcation point B $(0\ 1\ -\ -\ 1\ 0)$ $[0^\circ, 0^\circ, 0^\circ]$. It is expected that actuator legs 3 and 4 assume the same intermediate length when the other four legs assume the labeled extreme lengths. The error function to be minimized is:

$$e(\mathbf{u}, \mathbf{w}) = \left(v_1(\mathbf{u}, \mathbf{w}) - v_1^{\min}\right)^2 + \left(v_2(\mathbf{u}, \mathbf{w}) - v_2^{\max}\right)^2 + \left(v_5(\mathbf{u}, \mathbf{w}) - v_5^{\max}\right)^2 + (w_1 - 0)^2 + (w_2 - 0)^2 + (w_3 - 0)^2 \quad \text{(C.1)}$$

The global coordinates that were obtained for bifurcation point B $(0\ 1\ -\ -\ 1\ 0)$ $[0^\circ, 0^\circ, 0^\circ]$, by minimizing the error function (B.1) using *LFOPCV3*, are $(6.197,\ 0.0,\ 6.613)$.

These coordinates and the fixed orientation of the top platform ($\alpha = 0^\circ, \beta = 0^\circ$ and $\gamma = 0^\circ$), are substituted into expressions (3.3) and (3.4) to determine the actuator leg lengths:

$$l_1 = l_6 = 8.0 = l_{\min}$$
$$l_2 = l_5 = 15.0 = l_{\max}$$
$$l_3 = l_4 = 11.331$$

This validates the definition of error function (C.1).

Appendix D

D Determination of a Non-Vertical Bifurcation Curve of the Fixed Orientation 6–3 Stewart Platform Workspace

Bifurcation line $A'B'C'$ $[0^\circ, 0^\circ, -30^\circ]$ presented as part of the fixed orientation accessible workspace boundary ∂A $[0^\circ, 0^\circ, -30^\circ]$ shown in Figure 4.3 is analyzed in more detail looking at the three vertical planes of the fixed orientation accessible workspace A $[0^\circ, 0^\circ, -30^\circ]$, respectively isolated at $\theta = 15^\circ$, $\theta = 30^\circ$ and $\theta = 45^\circ$.

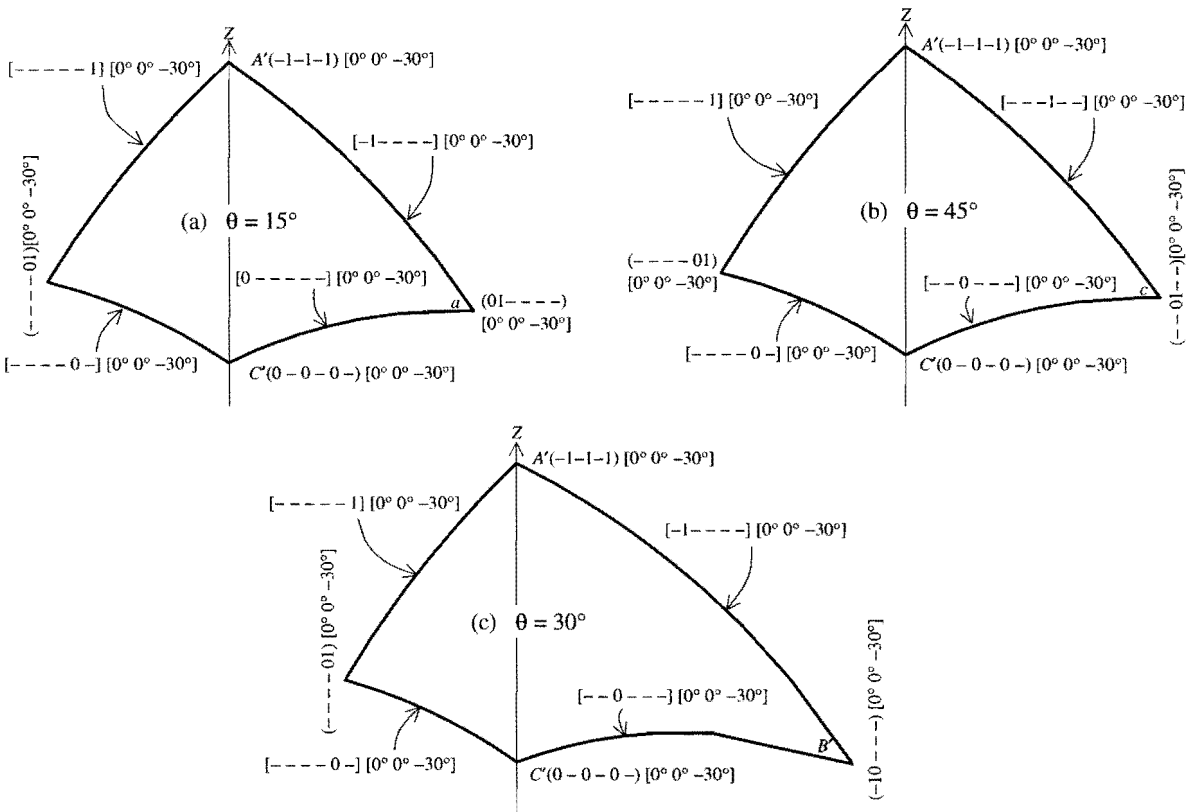

Figure D.1 Sections of ∂A $[0^\circ, 0^\circ, -30^\circ]$ at (a) $\theta_i = 15^\circ$, (b) $\theta_i = 45^\circ$, and (c) $\theta_i = 30^\circ$.

Figure D.1 (a) shows the section of the fixed orientation accessible boundary ∂A $[0^\circ, 0^\circ, -30^\circ]$ in the vertical plane at $\theta_i = 15^\circ$. Along curve $A'a$ $[-1 - - - -]$ $[0^\circ, 0^\circ, -30^\circ]$ $[\theta_i = 15^\circ]$, actuator leg 2 remains at its maximum length as the manipulator working point follows the curve. Curve $A'a$ forms

part of the convex boundary surface $A'B'D'$ labeled in Section 4.3 as $A'B'D'$ $[-\ 1\ -\ -\ -\ -]$ $[0^\circ,\ 0^\circ,\ -30^\circ]$. Similarly curve aC' $[0\ -\ -\ -\ -\ -]$ $[0^\circ,\ 0^\circ,\ -30^\circ]$ $[\theta_i = 15^\circ]$ is characterized by actuator leg 1 remaining fixed at its minimum length, and curve aC' forms part of the concave boundary surface $C'B'D'$ $[0\ -\ -\ -\ -\ -]$ $[0^\circ,\ 0^\circ,\ -30^\circ]$.

Next consider Figure D.1 (b) which shows the section of the fixed orientation accessible boundary $\partial A\,[0^\circ,\ 0^\circ,\ -30^\circ]$ in the vertical plane at $\theta_i = 45^\circ$. The labels of convex curve $A'b$ $[-\ -\ -\ 1\ -\ -]$ $[0^\circ,\ 0^\circ,\ -30^\circ]$ $[\theta_i = 45^\circ]$ and concave curve bC' $[-\ -\ 0\ -\ -\ -]$ $[0^\circ,\ 0^\circ,\ -30^\circ]$ $[\theta_i = 45^\circ]$ respectively correspond to the labels of convex boundary surface $A'E'B'$ and concave boundary surface $C'E'B'$ labeled in Section 4.3.

The *actual* bifurcation curve $A'B''C'$ coinciding with the intersection of the four boundary surfaces $A'B'D'$ and $A'E'B'$, as well as $C'B'D'$ and $C'E'B'$ (as labeled in Section 4.3), consists out of two bifurcation lines. The upper bifurcation line is a convex, and is labeled $A'B''$ $[-\ 1\ -\ 1\ -\ -]$ $[0^\circ,\ 0^\circ,\ -30^\circ]$, while the bottom bifurcation line is and a concave with label $B''C'$ $[0\ -\ 0\ -\ -\ -]$ $[0^\circ,\ 0^\circ,\ -30^\circ]$. These two bifurcation lines intersect at bifurcation point B'' $(0\ 1\ 0\ 1\ -\ -)$ $[0^\circ,\ 0^\circ,\ -30^\circ]$.

The curve $A'B'C'$ obtained from the vertical plane at $\theta_i = 30^\circ$ is labeled and shown in Figure D.1 (c). Convex "bifurcation line" $A'B'$ $[-\ 1\ -\ -\ -\ -]$ $[0^\circ,\ 0^\circ,\ -30^\circ]$ $[\theta_i = 30^\circ]$ does in actual fact not coincide with the intersection of boundary surfaces $A'B'D'$ and $A'E'B'$, as it is part of boundary surface $A'B'D'$ $[-\ 1\ -\ -\ -\ -]$ $[0^\circ,\ 0^\circ,\ -30^\circ]$. Similarly, concave "bifurcation line" $B'C'$ $[-\ -\ 0\ -\ -\ -]$ $[0^\circ,\ 0^\circ,\ -30^\circ]$ $[\theta_i = 30^\circ]$ forms part of boundary surface $C'E'B'$ $[-\ -\ 0\ -\ -\ -]$ $[0^\circ,\ 0^\circ,\ -30^\circ]$, and does not coincide with the intersection of the two boundary surfaces $C'E'B'$ and $C'B'D'$.

The actual bifurcation curve $A'B''C'$ is shown in Figure D.2 together with the near bifurcation curve $A'B'C'$ and they almost coincide.

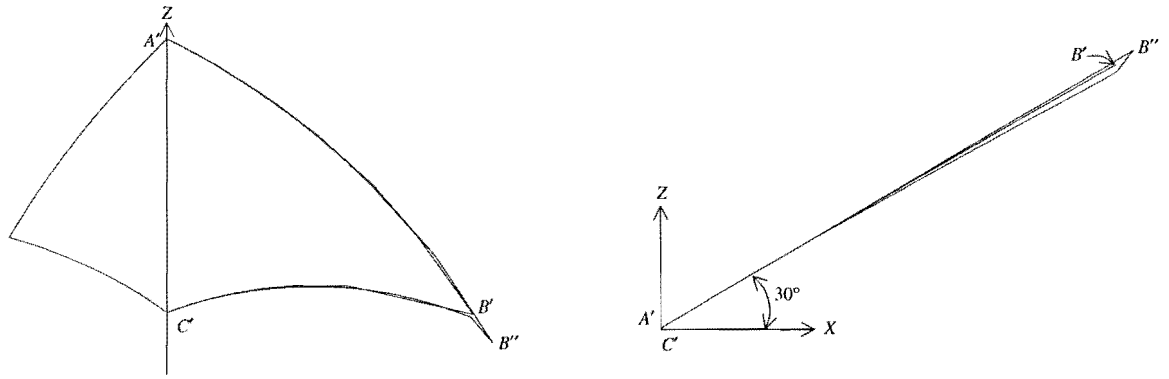

Figure D.2 The near ($A'B'C'$) and actual ($A'B''C'$) bifurcation curves.

The computed "bifurcation" curves $A'B'C'\left[0^\circ, 0^\circ, -30^\circ\right]$, $A'D'C'\left[0^\circ, 0^\circ, -30^\circ\right]$, $A'E'C'$ $\left[0^\circ, 0^\circ, -30^\circ\right]$, $A'F'C'$ $\left[0^\circ, 0^\circ, 30^\circ\right]$, $A'G'C'$ $\left[0^\circ, 0^\circ, 30^\circ\right]$ and $A'H'C'$ $\left[0^\circ, 0^\circ, 30^\circ\right]$ as presented in Figure 4.4 are also not the exact bifurcation curves. The deviations are however sufficiently small so as to be considered negligible from a practical point of view.

In addition the bifurcation lines all lie outside the dextrous workspace $\boldsymbol{A}\left[0^\circ, 0^\circ, (-30^\circ)-(30^\circ)\right]$ (Volume $A'C'I'J'K'L'M'N'$) as shown in Figure 4.5 and may therefore be ignored in the further analysis of the dextrous workspace.

REFERENCES

[1] Stewart, D. 1965. "A platform with six degrees of freedom." *Proceedings of the Institution of Mechanical Engineers 1965-1966*, 371-386.

[2] Gough, V. E. 1956. "Contribution to discussion to papers on research in tyre performance, by Cornell staff ." *Proc. Auto. Div. Instn. Mech. Engrs. 1956-57*, 392.

[3] Gough, V. E. 1962. "Universal tyre test machine." *Proceedings, Ninth International Technical Congress F.I.S.I.T.A. May 1962.* 117 (Institution of Mechanical Engineers).

[4] Merlet, J.P. 1994. "Parallel manipulators: state of the art and perspectives." *Advanced Robotics.* Vol.8, No.6, 589-596.

[5] Duffy, J. and C. D. Crane. 1997. Research proposal submitted to the National Science Foundation. *University of Florida, Gainesville USA.*

[6] Lin, W., Crane, C.D. and J. Duffy. 1992. "Closed-form forward displacement analyses of the 4–5 in-parallel platforms." *Robotics, Spatial Mechanisms, and Mechanical Systems, ASME 1992*, 521-527.

[7] Wang, J. and C.M. Gosselin. 1997. "Kinematic analysis and singularity representation of spatial five-degree-of-freedom parallel mechanisms." *Journal of Robotic Systems.* 14(12), 851-869.

[8] Haug, E. J., J. Y. Wang and J. K. Wu. 1994. "Dextrous workspaces of manipulators, Part 1: Analytical Criteria. *Technical Report R-125: Center for Simulation and Design Optimization of Mechanical Systems and Mechanical Engineering*, The University of Iowa.

[9] Gosselin, C. M. and J. Wang. 1997. "Singularity loci of planar parallel manipulators with revolute actuators." *Robotics and Autonomous Systems.* 21, 377-398.

[10] Bajpai, A. and B. Roth. 1986. "Workspace and mobility of a closed-loop manipulator." *The International Journal of Robotics Research.* Vol. 5, No. 2, 131-142.

[11] Kumar, V. 1992. "Characterization of workspaces of parallel manipulators." *Transactions of the ASME, Journal of Mechanical Design.* Vol.114, Sept., 368-375.

[12] Haug, E. J., C.M. Luh, F. A. Adkins and J.Y. Wang. 1994. "Numerical algorithms for mapping boundaries of manipulator workspaces." *IUTAM Summer School, Aalborg, Denmark, 1994: Concurrent Engineering Tools for Dynamic Analyses and Optimization, Mechanism and Manipulator Workspace Analyses.*

[13] Lee, J., J. Duffy and M. Keler. 1996. "The optimum quality index for stability of in-parallel planar platform devices." Proceedings of The 1996 ASME Design Engineering Technical Conferences and Computer in Engineering Conference, August 18-22, 1996, Irvine, California. 96-DETC/MECH-1135.

[14] Merlet, J. P., C. M. Gosselin and N. Mouly. 1998. "Workspaces of planar parallel manipulators." *Mechanism and Machine Theory.* Vol.33, No.1/2, 7-20.

[15] Griffis, M. and J. Duffy. 1989. "A forward displacement analyses of a class of Stewart platforms." *Journal of Robotic Systems.* 6(6), 703-720.

[16] Lin, W., Griffis, M. and J. Duffy. 1992. "Forward displacement analyses of the 4-4 Stewart platforms. *Transactions of the ASME, Journal of Mechanical Design.* Vol.114, No.3, 444-450.

[17] Fichter, E. F. 1986. "A Stewart platform based manipulator: General Theory and Practical Construction." *The International Journal of Robotics Research.* No.5, Vol.2, 157-182.

[18] Liu, K., Fitzgerald, J.M. and F.L. Lewis. 1993. "Kinematic analyses of a Stewart platform manipulator." IEEE Transactions on Industrial Electronics. Vol.40, No.2, 282-293.

[19] Arai, T., Tanikawa, T., Merlet, J.P. and T. Sendai 1996. "Development of a new parallel manipulator with fixed linear actuators." *ASME Proceedings of the Japan/USA Symposium on Flexible Automation.* Vol.1, 145-149.

[20] Honneger, M., Codourey, A. and E. Burdet. "Adaptive control of the Hexaglide, a 6 DOF parallel manipulator." *Institute of Rotics, ETH Zurich, Switzerland.*

[21] Hervè J.M. 1992. "Group mathematics and parallel link mechanisms." *IMACS/SICE International Symposium on Robotics, Mechatronics, and Manufacturing Systems.* Kobe, 16-20 Sept., 459-464.

[22] Ji, Z., and P. Song. 1998. "Design of a reconfigurable platform manipulator." *Journal of Robotic Systems.* 15(6), 341-346.

[23] Ji, Z. 1996. "Analyses of design parameters in platform manipulators." *Transactions of the A SME, Journal of Mechanical Design.* Vol. 118, Dec., 526-531.

[24] "HEXAPOD the technology breakthrough" *Technical brochure published by:* Geodetic Technology (USA) Inc. Gaskins Center, 3827 Gaskins Road, Glen Allen, Virginia 23060, USA, 1997.

[25] Zou, H., Wang, Q., Li, Q. and Zhang, B. 1996. "The kinematics and workspace analyses of a parallel manipulator for manufacturing." *Proceedings of The IEEE International Conference on Industrial Technology.* 647-650.

[26] "TRICEPT HP" *Technical Brochure published by:* COMAU, Via Rivalta 30, 10095 Grugliasco, Torino, Italy, 1997.

[27] "FLEXTOOL The solution to Assembly Flexibility" Technical Brochure published by: FANUC Robotics North America, 2000 South Adams Road, Auburn Hills, MI 48326-2800, 1996.

[28] "INA Components for a new machine tool concept" Technical Brochure published by: INA Wälzlager Schaeffler oHG, Herzogenaurach, 1998.

[29] Wang, L.T. and J.H. Hsieh. 1998. "Extreme reaches and reachable workspace analyses of general parallel robotic manipulators." *Journal of Robotic Systems.* 15(3), 145-159.

[30] Geng, Z., Haynes, L. S., Lee, J. D. and R. L. Carroll. 1992. "On the dynamic model and kinematic analysis of a class of Stewart platforms." *Robots and Autonomous Systems.* 9, 237-254.

[31] Waldron, K. J. and K. H. Hunt. 1991. "Series-parallel dualities in actively coordinated mechanisms." *The International Journal of Robotics Research* 10(2), 473-480.

[32] Zamanov. V.B. and Z.M. Sotirov. 1991. "A contribution to the serial and parallel manipulator duality." *Proceedings of the 8 th World Congress on the Theory of Machine and Mechanisms, Prague.* 517-520.

[33] Merlet, J. P. 1995. "Follow-up on parallel manipulators: a short history." *Posted on Internet by:* Jean-Pierre.Merlet@sophia.inria.fr (Comp.Robotics.Research).

[34] Innocenti, C. 1995. "Direct kinematics in analytical form of the 6-4 fully-parallel mechanism." Transactions of the ASME, Journal of Mechanical Design. Vol.117, No.2, 89-95.

[35] Gosselin, C. 1990. "Determination of the workspace of 6-DOF parallel manipulators." *Transactions of the ASME, Journal of Mechanical Design.* Vol.112, 331-336.

[36] Kumar, A. and K. J. Waldron. 1981. "The workspaces of a mechanical manipulator." *Transactions of the ASME, Journal of Mechanical Design.* Vol.103, 665-672.

[47] Abbasi, W.A., Ridgeway, S.C., Adsit, P.D., Crane, C.D. and J. Duffy, 1997. "Development of a special 6–6 parallel platform for countour milling." *Proceedings of the ASME Manufacturing Engineering Division 1997 International M.E. Congress and Exposition (IMECE), Dalas*, 373-380.